University of Crete

Strong Light-Matter Coupling in GaN Microcavities

by
Emmanouil Trichas

A thesis submitted in partial fulfillment for the
degree of Doctor of Philosophy
in the
Faculty of Science
Department of Materials Science & Technology

December 12, 2010

ΠΑΝΕΠΙΣΤΗΜΙΟ ΚΡΗΤΗΣ

ΠΕΡΙΛΗΨΗ

Σχολή Θετικών Επιστημών
Τμήμα Επιστήμης & Τεχνολογίας Υλικών
από τον διδάκτορα
Τριχά Εμμανουήλ

Ισχυρή Σύζευξη Ύλης-Φωτός στις Μικροκοιλότητες GaN

Όλες οι σύγχρονες φωτονικές δομές σε εφαρμογές χρήσιμες για τον άνθρωπο, όπως ο φωτισμός, οι οθόνες, τα οπτικά δίκτυα, τα φωτοβολταϊκά συστήματα παραγωγής ενέργειας, τα κβαντικά πληροφοριακά συστήματα κλπ, βασίζονται στον έλεγχο της αυθόρμητης εκπομπής φωτός. Για παράδειγμα, οι LEDs (Light Emitting Diodes) προσπαθούν να αντικαταστήσουν της λάμπες φθορισμού και πυρακτώσεως, βασισμένες στην αυθόρμητη εκπομπή. Στα δε laser, τα οποία είναι πηγές ενισχυμένων συμφώνων φωτονίων, η αυθόρμητη εκπομπή συζεύγνειται με τον οπτικό τρόπο ταλάντωσης της αντίστοιχης οπτικής κοιλότητας. Συνεπώς, υπάρχει ισχυρό κίνητρο ελέγχου της αυθόρμητης εκπομπής και της χρήσης της σε φωτονικές δομές κατά το δοκούν.

Σύμφωνα με την κβαντική θεωρία του φωτός, για τον έλεγχο της αυθόρμητης εκπομπής, είναι σημαντικό να ελεγχθούν οι οπτικοί τρόποι ταλάντωσης καθώς και η χωρική τους κατανομή σε σχέση με την εκπομπή. Οι *μικροκοιλότητες* είναι φωτονικές δομές ελέγχου της αυθόρμητης εκπομπής σε ημιαγωγικά συστήματα και σε αυτές «συναντώνται» η *δέσμια κατάσταση ζεύγους ηλεκτρονίου-οπής*, γνωστή και ως *εξιτόνιο*, με τα *χωρικά περιορισμένα φωτόνια*, ως τρόποι οπτικού συντονισμού σε οπτικό ταλαντωτή διαστάσεων μικρομέτρου και κατώτερων αυτού. Σε αυτές απαντώνται φαινόμενα όπως *η ασθενής (Weak Coupling-WC)* καθώς και *η ισχυρά* (Strong Coupling-SC) *σύζευξη ύλης-φωτός (exciton-photon)*.

Η ισχυρά σύζευξη, ως κβαντικό φαινόμενο, γίνεται κατανοητή με την θεώρηση ενός *οιονεί-σωματιδίου*, που ονομάζεται *πολαριτόνιο*. Η μελέτη αυτού, κυρίως στο σύστημα *Αρσενικούχου Γαλλίου (GaAs)*, οδήγησε στην κατασκευή καινοτόμων φωτονικών δομών, όπως το λεγόμενο polariton LED και το polariton laser πολύ μικρού κατωφλίου. Σε αυτές αξιοποιήθηκε ο μποζονικός χαρακτήρας των πολαριτονίων που του προσδίδει μοναδικές ιδιότητες όπως η εξαναγκασμένη σκέδαση, η παραμετρική ενίσχυση, το lasing, η συμπύκνωση και η υπερρευστότητα.

Σημαντικό μειονέκτημα της τεχνολογίας αυτής είναι η αδυναμία επίτευξης ισχυράς σύζευξης ύλης-φωτός σε θερμοκρασία δωματίου, ως απαραιτήτου στοιχείου για κατασκευή οπτοηλεκτρονικών εφαρμογών ικανών να λειτουργήσουν σε κανονικές συνθήκες περιβάλλοντος. Για να ξεπεραστεί ένα τέτοιο τεχνολογικό πρόβλημα, ένας τρόπος είναι και η επιλογή ενός κατάλληλου υλικού, του οποίου το *εξιτόνιο* παραμένει «σθεναρό» σε θερμοκρασία δωματίου. Έτσι, κριτήριο επιλογής του υλικού αποτελεί η μέγιστη δυνατή *ενέργεια σύνδεσης εξιτόνιου (exciton binding energy)* που μπορεί να παράσχει αυτό. Ένας τέτοιος «υποψήφιος» είναι και το *Νιτρίδιο του Γαλλίου (GaN)*, του οποίου οι μικροκοιλότητες γίνονται αντικείμενο μελέτης ετούτης της διδακτορικής

διατριβής. Ένα άλλο θέμα που προκύπτει επίσης, είναι και η ανάγκη για μέγιστο δυνατό χωρικό περιορισμό των φωτονίων και υψηλό παράγοντα ποιότητας των μικροκοιλοτήτων (Q-factor). Ταυτόχρονα, η ανάπτυξη επάλληλων ημιαγωγικών υλικών, ως καθρεπτών Bragg των μικροκοιλοτήτων, με μονολιθικές μεθόδους ανάπτυξης, όπως η επιταξία μοριακής δέσμης (MBE) ή και με άλλες, δημιουργεί συσσώρευση τάσεων στα διάφορα στρώματα της δομής, οδηγώντας σε εμφάνιση ατελειών δομής και σε ρηγματώσεις. Οι αστοχίες αυτές μεταβιβάζονται στο στρώμα εκπομπής της μικροκοιλότητας, διευρύνοντας την κορυφή εξιτονικής απορρόφησης του υλικού, στοιχείο αρνητικό για την ισχυρά σύζευξη. Από την άλλη, οι προσπάθειες αναίρεσης των ανωτέρω οδηγεί σε αισθητή μείωση του εύρους μεγίστης ανακλαστικότητας των καθρεπτών, συγκρίσιμου με το λεγόμενο *διαχωρισμό Rabi* μεταξύ των άνω και κάτω βραχιόνων διασποράς του πολαριτονίου. Αποτέλεσμα ετούτου είναι η αδυναμία δημιουργίας ισχυράς σύζευξης στην μικροκοιλότητα. Η αντιμετώπιση αυτού του προβλήματος γίνεται με την ανάπτυξη διηλεκτρικών καθρεπτών, που απαλείφουν τις προαναφερθείσες αστοχίες και συνάμα επιτυγχάνουν τον μέγιστο δυνατό χωρικό περιορισμό των φωτονίων.

Τελικά, η διδακτορική αυτή διατριβή πραγματεύεται την μεθοδολογία εγκιβωτισμού λεπτού υμενίου του *GaN* σε μια μικροκοιλότητα, φτιαγμένη από δύο διηλεκτρικούς Bragg καθρέπτες. Βασικό εργαλείο της κατασκευής αποτελεί η λεγόμενη φωτο-ενισχυόμενη ηλεκτροχημική υγρή εγχάραξη θυσιαζόμενου υποκειμένου στρώματος για την δημιουργία ελεύθερων-αιωρούμενων λεπτών υμενίων *GaN*.. Η τεχνική αυτή εξασφαλίζει τις απαιτούμενες υπέρ-λείες επιφάνειες του υμενίου, καθώς και την διατήρηση των πολύ καλών οπτικών ιδιοτήτων του *Νιτριδίου του Γαλλίου*.

Μεγάλο μέρος τις εργασίας που εκπονήθηκε, αναλώθηκε στη μελέτη αυτής κάθ‘ εαυτής της μεθόδου. Χρησιμοποιώντας ένα σύστημα παλμικού laser, μεταβλητού μήκους κύματος, ως πηγή φωτοενίσχυσης-διέγερσης του προς εγχάραξη στρώματος, μελετήσαμε την ιδιότητα της *επιλεκτικής εγχάραξης (selective etching) νιτριδίων με διαφορετικό ενεργειακό χάσμα (Energy Bandgap)* κατά την διεύθυνση ανάπτυξης των διαφορετικών αυτών νιτριδίων, καθώς και την τραχύτητα των απομενόντων επιφανειών. Παρατηρήσαμε την περαιτέρω έντονη ενίσχυσή του ρυθμού επιλεκτικής εγχάραξης και του επαγόμενου φωτορεύματος κατά την περίπτωση *συντονισμού* της οπτικής διέγερσης του παλμικού laser με το εξιτόνιο του προς εγχάραξη νιτριδίου. Το χαρακτηριστικό αυτό μετατρέπει την μέθοδο αυτή σε εξαιρετικά επιλεκτική υγρή εγχάραξη με βάση το ενεργειακό χάσμα. Με αυτόν τον τρόπο καταφέραμε να εγχαράξουμε επιλεκτικά στρώματα νιτριδίων με μικρότερο ενεργειακό χάσμα σε σχέση με τα υποκείμενά τους, στα οποία και τερματίστηκε αφ’ εαυτής η εγχάραξη, δεδομένου του μεγαλύτερού τους χάσματος. Χρησιμοποιώντας την ιδιότητα αυτή (*high selectivity*) κατά την *επιφανειακή (lateral)* διεύθυνση και με επάλληλες βελτιστοποιήσεις των συνθηκών της εγχάραξης του θυσιαζόμενου υποκειμένου νιτριδίου, καταφέραμε να σχηματίσουμε υψηλής ποιότητας λεπτά υμένια *GaN* για την κατασκευή των αντίστοιχων μικροκοιλοτήτων.

Η εναπόθεση διηλεκτρικών καθρεπτών στην ανάντι και κατάντι πλευρά του λεπτού υμενίου, με μεθόδους sputtering ή εξάχνωσης με δέσμη ηλεκτρονίων, ολοκληρώνει την λεγόμενη *all-dielectric GaN μικροκοιλότητα*. Ο οπτικός χαρακτηρισμός των μικροκοιλοτήτων, που αναπτύχθηκαν με την μέθοδο αυτή, αποτέλεσε και αυτός σημαντικό αντικείμενο αυτή της διατριβής. Παρατηρήθηκε *ένδειξη ισχυράς σύζευξης του εξιτονίου (exciton) και οπτικού Bragg τρόπου (Bragg mode)* ενός εκ των διηλεκτρικών καθρεπτών, εισάγοντας ένα νέο εμφανιζόμενο οιονεί-σωματιδίο, το λεγόμενο *Bragg-*

polartion ή *Braggoriton*. Το θετικό αυτό αποτέλεσμα, είναι απόδειξη του ότι η κατασκευή *all-dielectric GaN* μικροκοιλοτήτων είναι εφικτή με την μέθοδο της προαναφερθείσας φωτο-ενισχυόμενης ηλεκτροχημικής υγρής εγχάραξης και ικανή να δώσει ισχυρά σύζευξη εξιτονίου-φωτονίου με μεγάλα Q-factors. Αποτελεί, λοιπόν, έρεισμα για ανάπτυξη καινοτόμων τεχνολογιών εκπομπής πολαριτονίων, λειτουργούντων σε θερμοκρασία δωματίου καθώς και για ανάπτυξη νέας φυσικής που διέπει την μποζονική φύση των πολαριτονίων.

Παράλληλα με των ανάπτυξη μικροκοιλοτήτων βασισμένων στα νιτρίδια, ασχοληθήκαμε και με μια άλλη κατηγορία υλικών και εξιτονίων, ικανών να δώσουν *ισχυρά σύζευξη σε θερμοκρασία δωματίου*, τα λεγόμενα *j-aggregates*, ως φορείς των λεγομένων *Frenkel excitons*, σε αντιδιαστολή με τα *Wannier-Mott excitons* των ανόργανων ημιαγωγικών υλικών. Σχηματίστηκαν μικροκοιλότητες με μεταλλικούς καθρέπτες και μελετήθηκαν οι οπτικές τους ιδιότητες. Έντονο ήταν το φαινόμενο της φωτο-οξείδωσης των υλικών αυτών κατά την οπτική διέγερσή τους, δημιουργώντας δυσμενείς συνθήκες διατήρησης του πολαριτονίου. Παρόλα αυτά, ένα j-aggregate εκ των δοκιμασθέντων επέδειξε αντοχή στον χρόνο και το φως καθώς ισχυρά σύζευξη του εξιτονίου του με τον οπτικό τρόπο, με αντίστοιχο *διαχωρισμό Rabi* των 56meV.

To my parents, who love me so much,
but never understood what I have
been doing all these years…!!

Contents

List of Figures

FIG. 4.15 Typical “saw” structure oscillation of the photocurrent during PEC etching of GaN. The exponential decay of the photocurrent is attributed to the oxide formation. When the shutter closes the electrolyte etches the oxide and when it opens, the photocurrent reaches its initial value

FIG.4.16. a) SEM image of a porous GaN oxide after PEC etching experiment, b) SEM image of a recessed GaN patterned square after PEC etching experiment and itsoxide removal.

FIG. 4.17. SEM image of the a-step tip scan on a PEC etched $In_{0.1}Ga_{0.9}N$ surface.

FIG. 4.18. a) SEM image of the a-step tip scan on a PEC etched $In_{0.1}Ga_{0.9}N$ surface. The sample was used is consisted of 50nm thick $In_{0.1}Ga_{0.9}N$ layer, undoped, b) AFM image of the GaN layer just above the fully etched $In_{0.1}Ga_{0.9}N$ layer.

FIG. 4.19. SEM picture following selective PEC etching of GaN on $Al_{0.2}Ga_{0.8}N$ showing sharp sidewalls and smooth etched surface. The 350 nm sidewall which is independent of etch time proves the bandgap selective nature of the etching process. The Ti mask was removed to measure the real etch depth, corresponding to the thickness of the GaN layer

FIG. 4.20. Plot of the photocurrent density versus time during the PEC etching of an InGaN layer. At ~2400sec one can clearly see the PEC etching process stopping by itself when reaching a layer of a greater to the excitation energy bandgap.

FIG. 4.21. SEM image of the inversed InGaN pyramids corresponding to the thread dislocations.

FIG. 4.22. The hexagonal wurtzite crystal structure of GaN. The c-plane or (0001) direction is a very resistive to all kind of etchants (including HF) at room temperature. On the contrary, the $(000\bar{1})$ direction can be very easily etched even by low concentration acid or alkali solutions. (www.ece.cmu.edu/~dwg/research/polarity.html).

FIG. 5.1. a) SEM image of an n-type sacrificial GaN layer etched below a p-type GaN top layer [8], [9]. One can clearly see the inversed pyramid features transferred into the p-type etch-stop layer, “destroying” the selectivity of the PEC lateral process, resulting in an increase of surface

FIG. 6.12. Reflectivity spectra simulation of a 10-pair SiO_2/Ta_2O_5 DBR for TM and TE polarizations.

FIG. 6.13. Intentionally spaced, acquired at different angles, reflectivity spectra of the top (second) DBR, used in our all-dielctric microcavities. The s (TE) and p (TM) waves are clearly identified.

FIG. 6.14. Setup of the angle resolved PL experiment. The angle range used for the spectra acquisition was from 0º-73º degrees

FIG. 6.15. Intentionally spaced angle resolved photoluminescence spectra of all-dielectric GaN microcavities, acquired at room temperature.

FIG. 6.16. Plot of intensity normalized photoluminescence from GaN microcavity sample. Dashed lines are TM, TE Bragg modes extracted from reference mirror samples for the top and bottom DBRs respectively. Strong exciton-Bragg mode coupling and anticrossing behaviour are observed around 68°. Solid lines are just guides for the eye.

FIG. 7.1 Progression from atomic orbitals in two isolated atoms, through the formation of a bonding orbital in a simple diatomic molecule, and the generation of several bonding orbitals in a medium sized molecule, to the coalescence of orbital energy levels into bands. This last situation occurs when thousands or millions of atoms are connected to each other by a three-dimensional network of bonds. As in the case of small molecules, the energy levels are separated into a bonding set (valence band) and an antibonding set (conduction band) [12].

FIG. 7.2. Schematic representation of the electronic transitions in a monomer, H aggregate, and J-aggregate on the basis of the interaction between molecular excitons in aggregates, where *a* is the slip angle between molecules in an aggregate, and $E_{TR}(M)$, $E_{TR}(H)$, and $E_{TR}(J)$ are the transition energies of a monomer, H-aggregate, and J-aggregate, respectively [13].

FIG. 7.3. a) Schematic representation of monomer's structure and its polarization direction, b) Peak absorption of our cyanine dye monomer molecule and its corresponding j-aggregate.

List of Tables

Publications

- **E.Trichas**, N. T. Pelekanos, E. Iliopoulos, E. Monroy, K. Tsagaraki, A. Kostopoulos and P. G. Savvidis, "Strong Exciton-Bragg mode coupling in all dielectric GaN microcavity, submitted in Appl. Phys. Lett. (2010).

- **E. Trichas**, M. Kayambaki, E. Iliopoulos, N.T. Pelekanos, P.G. Savvidis, "Resonantly enhanced selective photochemical etching of GaN", Appl. Phys. Lett. 94, 173505 (2009).

- **E. Trichas**, C. Xenogianni, M. Kayambaki, P. Tsotsis, E. Iliopoulos, N. T. Pelekanos, P. G. Savvidis, "Selective photochemical etching of GaN films and laser lift-off for microcavity fabrication", Phys. stat. sol. (a) 205, 2509 (2008).

- G. E. Dialynas, A. Pantazis, M. Androulidaki, K. Tsagaraki,G. Constantinidis, Z. Hatzopoulos, C. Xenogianni, **E. Trichas**, S. Tsintzos, P. G. Savvidis, N. T. Pelekanos, "InAs nanostructures on polar GaAs surfaces", International Journal of Nanotechnology 6, 124 (2009).

- G.E. Dialynas, C. Xenogianni, S. Tsintzos, **E. Trichas**, P.G. Savvidis, G. Constantinidis, J. Renard, B. Gayral, Z. Hatzopoulos, N.T. Pelekanos, "Anti-binding of biexcitons in (211)B InAs/GaAs piezoelectric quantum dots", Physica E, 40, 2113 (2008).

Acknowledgements

This PhD has been a very rich experience for me, with numerous people contributing to it, with ideas, guidance and support, in a professional and personal level.

First of all, I would like to thank my supervisor Prof. Pavlos Savvidis, for trusting me, and giving me the opportunity to learn all these new exciting polariton physics. I appreciate his support, his endless energy and passion, and his continuous presence in the laboratory, helping me in every scientific and technical problem. I would also like to thank Prof. Nikos Pelekanos for supporting me us a second supervisor, especially for his contribution in the interpretation of our results and stimulating discussions.

I am grateful to Prof. Georgakilas and Prof. Iliopoulos for providing the MBE facility, but especially I would like to thank Prof. Iliopoulos for providing very high quality nitride samples, which played a very important role in my study.

Special thanks go to Mrs Maria Kayambaki, who has been so enthusiastic in introducing me in the PEC etching of nitrides. I am also grateful to Maria Androulidaki and George Deligiorgis for learning me tricks on the optical characterization.

Many thanks and gratitude to Mr Athanasios Kostopoulos, Mr Antonis Stavrinidis and especially to Dr. George Konstantinidis for the continuous support, not only in the proceesing of nitrides but also for taking care of me, literally as a father, when ever I had been facing several problems in the lab.

Special thanks also to his wife, Mrs Katerina Tsagkaraki for spending so many hours with me, for taking pictures in the FE-SEM and AFM measurements, which I must say they were not easy tasks to do.

I would also like to thank Prof. Pantelis Trikalitis and his colleagues, Mrs Aleka Manousidaki and Mrs Sandra Siakouli for providing me a full and easy access in the electron microscopy facility of the University of Crete.

I am also really grateful to the two technicians of the Microelectronics Research Group of IESL, Mr Nikos Papadakis and Mr. Michalis Sfendourakis, who stood by me in every technical problem I faced up all these years and especially for transferring to me technical knowledge, useful for my life outside the academic world.

Finally, I would like to thank Prof. Maria Vamvakaki and especially his colleague, Dr. Maria Kalyva for our strong collaboration in fabricating the organic microcavities.

Chapter 1: Physics of Excitons and Optical Cavities

1.1 Controling Spontaneous Emission

Spontaneous emission (SE) is a fundamental phenomenon associated with the creation of light. All modern photonic devices in applications including illumination, displays, optical communication, solar energy and quantum-information systems etc are based on spontaneous emission control. For example, LEDs, which are poised to replace fluorescent and incandescent lighting, rely on SE to generate light, Similarly, in lasers, which are coherent light sources, SE couples to the lasing mode. As a result, there is a strong motivation to achieve control over SE and inhibit it when it is not desired or alternatively concentrate it into useful forms. In fact, controlling SE can be considered one of the most important objectives of current photonics research as it will probably lead to important and dramatic advances in device performance.

According to quantum theory of light [1], SE occurs when an emitter relaxes from an excited state to its ground state by photon emission into an optical mode that is not occupied by other photons. The rate of this transition is determined by the photonic density of states and the electric-field strength at the position of the emitter. Consequently, when trying to manipulate SE, it is important to control the number of optical modes and their spatial distribution relative to the emitter.

Microcavities are photonic structures which control the spontaneous emission of semiconducting materials [2], [3]. These can achieve the combination of *bound electron-hole pair (exciton)* and *photon confinements* and define the regime of their interaction leading to interesting phenomena such as the Strong Coupling (SC) and the Weak Coupling between light (photon) and matter (exciton) [4].

These systems have generated an intense research effort for the past two decades due to the light-matter interactions mentioned above which offer the opportunity for the fabrication of novel optoelectronic devices such as the co-called polariton LEDs and ultra low threshold polariton lasers [5-7]. Owing to their composite light-matter nature, polaritons exhibit strong nonlinearities and their behavior is often governed by a distinctive bosonic character, which is responsible for a series of spectacular demonstrations such as stimulated scattering of polaritons [8] polariton amplification [9-12], condensation [13-15], polariton lasing [16-20] and superfluidity [21], [22]. These unique properties of polaritons are believed to provide the basis for a new generation of polariton emitters and semiconductor lasers.

However, a key element of this technology is its ability to operate at room temperature (RT) so we can use it in ordinary optoelectronic devices. Researchers have already demonstrated light-matter interactions mostly at low temperatures in the GaAs system [23] and recently Tsintzos et. al [5], [6], have shown strong coupling at 295K, by incorporating pairs of $In_{0.1}Ga_{0.9}As/GaAs$ quantum wells in the microcavities, exploiting the large binding energy of confined excitons of these QWs. An other way to overcome this temperature barrier is to use materials that can provide robust excitons, with large binding energies at 300K.

1.2 Bandgap Engineering

The simplest form of light-matter interaction is the photon absorption of the semiconducting materials. When a photon of given wavelength (λ) with an energy above the material's bandgap E_g is absorbed, electron-hole pairs are created. These pairs can either recombine into a photon via spontaneous emission (radiative recombination) or thermally dissipate (non-radiative).

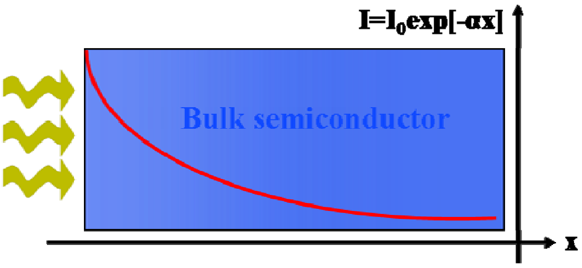

FIG. 1.1: schematic of the light absorption from a material. The intensity decreases exponentially with the penetration depth x.

There are several kinds of photon absorption attributed to a) band-to-band, b) impurity/defect, c) free carrier and of course d) excitonic transitions which leave their fingerprints on the material's absorption spectra. The absorption of light (see Fig. 1) is expressed by the absorption coefficient (α) which is proportional to the rate of decrease of light intensity (I) along its penetration path (x):

$$I = I_0 e^{-ax} \Rightarrow a = \frac{1}{I}\frac{dI}{dx}, \quad (1.1)$$

Where I_0 is the light intensity at x=0. This coefficient reflects how strong the material absorbs a particular wavelength.

At low temperatures optical absorption spectra of semiconductors show strong and sharp profiles, at energies just below the bandgap E_g (see Fig. 2). These are attributed to electron-holes pairs being bound together by Coulomb interactions, called excitons.

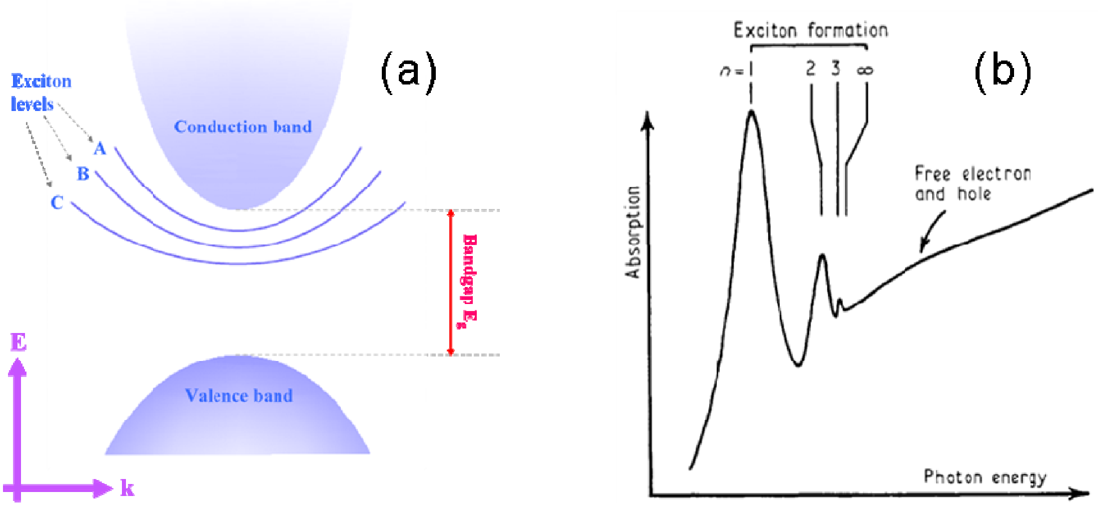

FIG. 1.2: a) band diagram of a wurtzite semiconductor. b) Absorption curve of a semiconductor at **low** temperature, showing strong absorption peaks due to ‘Mott- Wannier’ exciton series **(n** = 1,2, . . . CO) and the ‘continuum’ absorption due to ‘free electrons and holes’ at higher energies [24].

1.2.1 Wannier-Mott & Frenkel excitons

Excitons, in a variety of materials can be distinguished in a) Frenkel and b) Mott-Wannier excitons. In (1931) the Russian theorist Frenkel interpreted narrow photoemission lines being observed in the spectra of organic molecular crystals. He introduced the concept of excitation waves in crystals and later coined the term *exciton* (Frenkel 1936). Frenkel treated the crystal potential as a perturbation to the Coulomb interaction between an electron and a hole belonging to the same crystal cell. This scenario is most appropriate in organic molecular crystals [4].

The binding energy (see Eq. 2.2) of Frenkel excitons (i.e. the energy of its ionization to a non-correlated electron–hole pair) is typically of the order of 100– 300 meV. Frenkel excitons have been initially observed in alkali halides by Apker and Taft (1950). At present they are widely studied in organic materials where they dominate the optical absorption and emission spectra.

$$E_{b,n} = \frac{\hbar^2}{2\mu\left(\alpha_B^2\right)^2 n^2}, \quad (1.2) \text{ where } \alpha_B^2 \text{ is the exciton Bohr radius: } \alpha_B^2 = \frac{\hbar^2 \varepsilon_0}{e^2 \mu}, \quad (1.3)$$

At the end of the 1930s, Wannier (1937) and Mott (1938) developed the concept of excitons in inorganic semiconductor crystals. Unlike Frenkel excitons, Wannier–Mott excitons have a typical size of the order of tens of lattices constants and a relatively small binding energy, typically, a few meV (see Fig. 3).

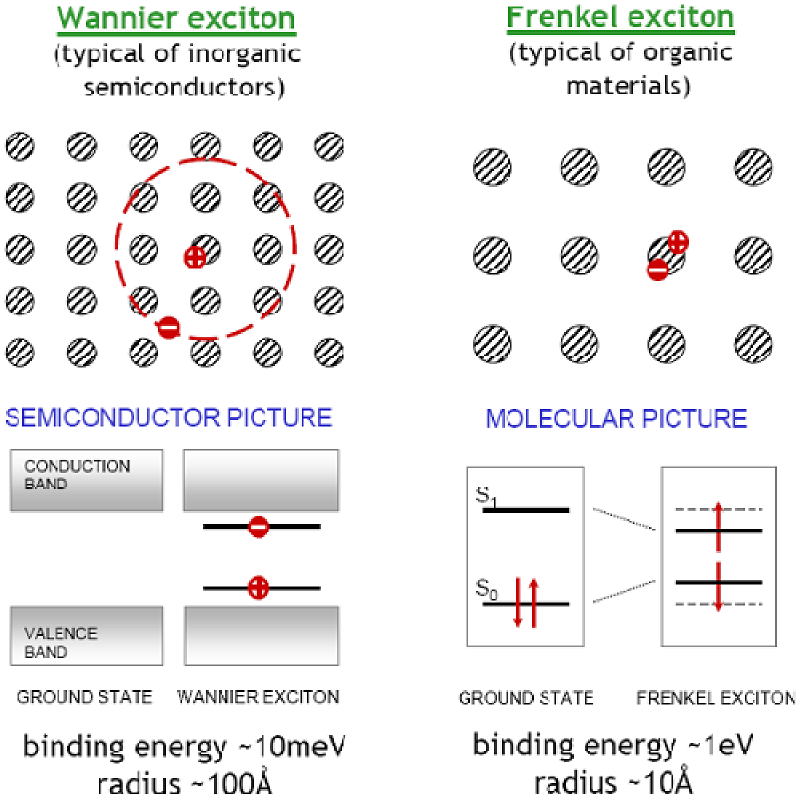

FIG. 1.3: Schematic illustration of the Wannier-Mott and Frenkel excitons and the band formation in the inorganic and organic semiconducting material [25].

Additionally to Wannier-Mott and Frenkel excitons in wurtzite inorganic semiconductors there is another species of the Bound Excitons (BE). These are multi-particle electronic excitations of defects in semiconductors, which are very useful for studying the electronic structure of shallow and deep impurities, as well as other defects. Bound-exciton photoluminescence spectra are also convenient signatures for these defects, by which they can easily be recognized in particular sample. Understanding bound-excitons is important for the operation of strongly coupled microcavities. Especially in the case of Gallium Nitride, we believe that donor bound exciton will not exhibit any oscillator strength at room temperature [26], since it begins to ionize above 100K. However, it will be interesting to investigate how nitride-based microcavites will be affected.

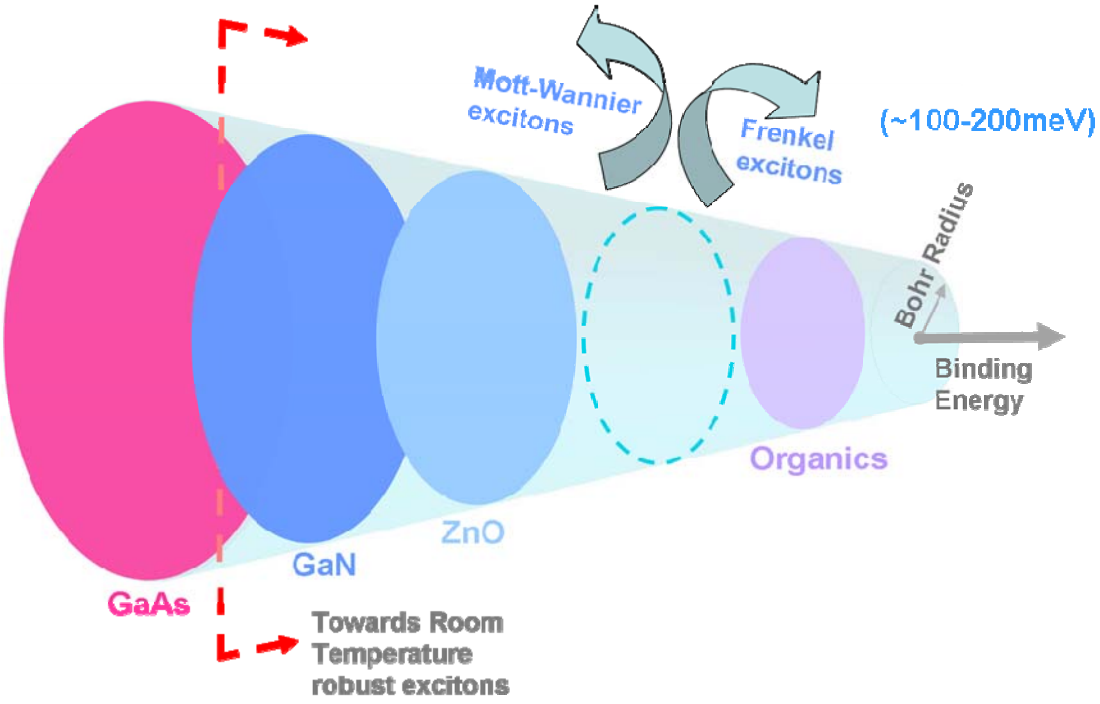

FIG. 1.4: schematic illustration of binding energy modulation with the exciton Bohr radius. Nitrides, zinc oxide, and organics exhibit binding energies greater than $K_B T$.

Figure 4 shows a schematic of how exciton binding energy increases with the decrease of Bohr radius. It is also a map of materials according to which we can select the proper ones for exploiting their Wannier-Mott or Frenkel excitons for the fabrication of optoelectronic devices. Gallium Arsenide exciton has a relatively small binding energy and as long we move to the family of nitrides, of Zinc Oxide we get higher binding energies. Inorganic semiconductors cannot provide smaller Bohr radius. Thus, we have to consider using the π-conjugated organic semiconductors like the j-aggregates of cyanine dyes or the polysilanes. This exciton binding energy-based material mapping will be used in chapter 3 in order to select materials as candidates for room temperature polariton emitters.

1.2.2 "S*emiclassical*" treatment of Exciton

An exciton is simulated just like the simple hydrogen atom using a Lorentzian oscillating dipole. In this, light is modelled by Maxwell's equations and the atom by a mechanical system of two masses—the nucleus and an electron—bound together by a spring [4], [27-30]. The spring is set into motion when light irradiates the atom.

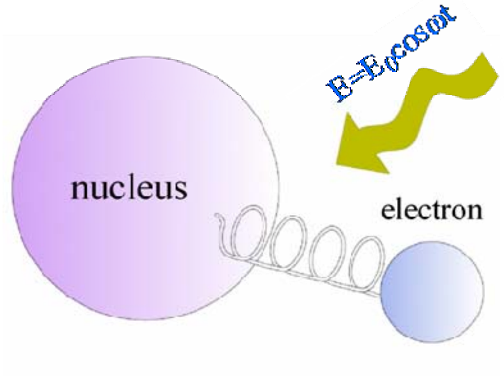

FIG. 1.5: schematic of Lorentzian Oscillating dipole.

The atom is fixed and the electron a distance *x(t)* away, moving under the influence of an applied electric field *E(t)*, with an equation of motion:

$$m_0\ddot{x} + m_0 2\gamma\dot{x} + m_0\omega_0^2 x = -eE(t) \qquad (1.4)$$

where m_0 is the mass of the electron, $-e$ its charge, ω_0 is the natural frequency of the oscillator and $m_0\omega_0^2$ the harmonic potential binding the electron (the spring). The loss term arises in this model from the fact that an oscillating dipole radiates energy. The exciting field is introduced as an harmonic function of time: $E = E_0 \cos\omega t$. The electron also oscillates harmonically with the frequency of the external force, but with a different amplitude and a different phase: $x(t \to \infty) = A\cos(\omega t + \varphi)$. The oscillation of the electric field is connected with a dipole moment with the nucleus-electron oscillator.

$$p_x = e * x_p \quad , \quad (1.5)$$

and a polarizability : $$a(\omega) = \frac{ex_p}{E_0} = \frac{e^2}{m}\left(\omega_0^2 - \omega^2 - i\omega\gamma\right)^{-1} \quad , \quad (1.6).$$

If we consider a semiconductor as a three-dimensional array of oscillators with N density, excited by electromagnetic radiation, the result will be the same and we shall get a preliminary polarization density $\boldsymbol{P}$ as described in equation (6).

$$\boldsymbol{P} = N\alpha\boldsymbol{E_0} = \frac{Ne^2}{m}\left(\omega_0^2 - \omega^2 - i\omega\gamma\right)^{-1}\boldsymbol{E_0} \quad , \quad (1.7)$$

Thus, the dielectric displacement is becoming:

$$\boldsymbol{D} = \varepsilon_0\ \boldsymbol{E} + \boldsymbol{P} = \varepsilon_0\left[1 + \frac{Ne^2}{m}\left(\omega_0^2 - \omega^2 - i\omega\gamma\right)^{-1}\right]\boldsymbol{E} \quad , \quad (1.8)$$

and the dielectric and susceptibility functions $\varepsilon(\omega)$, $\chi(\omega)$ are described by the following equation:

$$\varepsilon(\omega) = 1 + \frac{Ne^2}{m}\left(\omega_0^2 - \omega^2 - i\omega\gamma\right)^{-1} = \chi(\omega) + 1 \quad , \quad (1.9)$$

where N is the number of oscillators per unit volume V [31], [32]. A consequence of Eq. (1.9) is a modulated refractive index which describes the excitonic transition.

$$\tilde{n}(\omega) = n(\omega) + ik(\omega) = \sqrt{\varepsilon(\omega)}, \quad (1.10)$$

This refractive index is used in modeling of microcavities based on a transfer matrix TM method which treats the optically active medium of the microcavity as a matrix with elements, parts of this modulated refractive index of Eq. (1.10).

1.3 Oscillator Strength

The term Ne^2 / m^{-1} gives the coupling strength of the electromagnetic field to the oscillators in this classical model. In quantum mechanics, this coupling is given by the transition matrix element squared.

$$f = \frac{2N\omega_0}{\varepsilon_0 \hbar} \left| H_{ij}^D \right|^2 = \frac{2N\omega_0}{\varepsilon_0 \hbar} \left| \left\langle j \middle| H^D \middle| i \right\rangle \right|^2 \quad , \qquad (1.11)$$

where i and j stand for initial and final state and H^D for the dipole operator *er* or *ex*. Now, it is easy to easy to describe the dielectric function as:

$$\varepsilon(\omega) = 1 + \frac{f}{\omega_0^2 - \omega^2 - i\omega\gamma} \quad , \qquad (1.12)$$

It also well known that there is a correlation between the dielectric function, the refractive index of a semiconductor and its absorption coefficient $\alpha(\omega)$ of the Eq. 1.1. Thus, we can say that when an exciton can absorb light (Lorentz oscillating dipole) and undergo a transition from one quantum state to another. The *oscillator strength* is a quantity to express the strength of the transition. The meaningful quantity is the oscillator strength per unit volume, which is related to the absorption coefficient $\alpha(\omega)$ by

$$\int \alpha(\omega) d\omega = \frac{2\pi^2 e^2}{n m_0 c} \left(\frac{f}{V} \right), \qquad (1.13)$$

This means that the sharper the excitonic absorption is, the greater its oscillator strength becomes [2].

The correlation of the above physical parameters is used in chapter 4 in order to simulate a strongly coupled GaN-based microcavity, using a transfer matrix method.

In this method excitonic absorption is interpreted as a modulated function of the refractive index (or dielectric function), corresponding to the exciton oscillator strength.

1.4 The role of Exciton Confinement

Exciton confinement plays an important role in optical properties of semiconductors. Structures like quantum wells (QWs), superlattices (SLs), quantum dots (QDs), nanopilars and generally ultrathin layers or nanosized three dimensional structures of semiconducting materials decrease the Bohr radius of excitons, they increase the electrons and holes wavefunctions overlap leading to high binding energies and oscillator strengths [33].

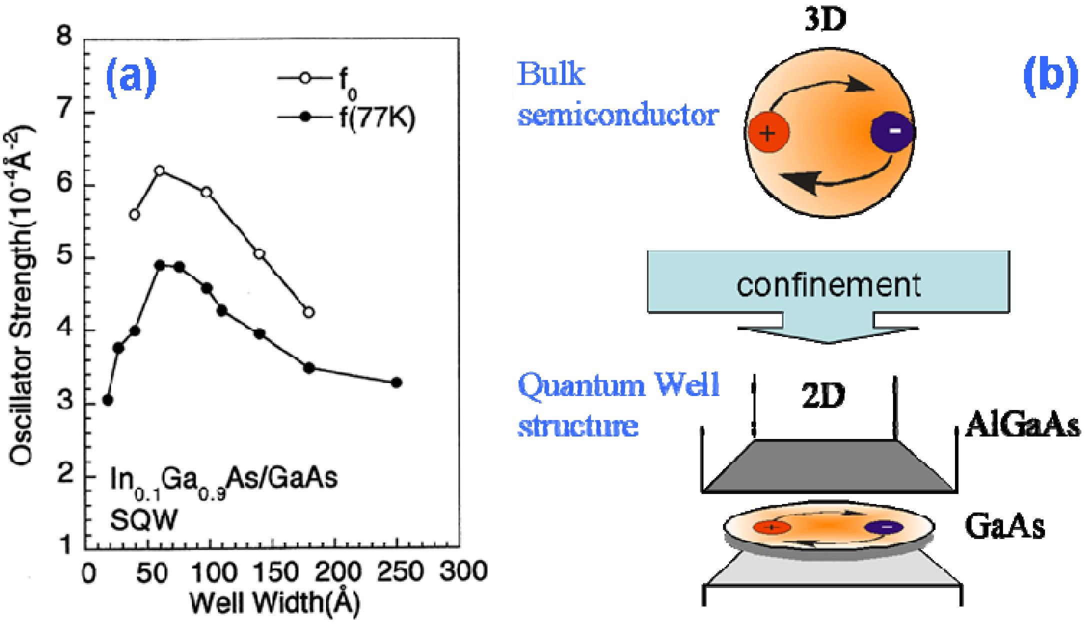

FIG. 1.6: a) characteristic modulation of exciton oscillator strength with the quantum well width in the InGaAs system [34], b) this modulation is due to the exciton confinement.

This increase of binding energy is such high, that resonant excitonic absorption peaks are far from the free electron-holes continuum and excitons are easier to see. The confinement also reduces the interaction channels between the excitons and the polar phonons (a problem we will formulate in Chapter 2) that are responsible for the temperature broadening. Although the width of the exciton peak is temperature broadend, it remains narrow enough to be resolved at room temperature.In the case of a QW the oscillator strength per unit surface depends on the QW's width, as seen in figure 6 [34].

1.5 The role of Photon Confinement

Photon confinement is the second key element needed for strong coupling between light and matter. It is achieved by the modulation of refractive index in optical microcavities where a set of discrete confined photon modes arises, called cavity modes. More precisely, a microcavity is an optical resonator close to, or below the dimension of the wavelength of light. Micrometre- and submicrometre-sized resonators use two different schemes to confine light. In the first, reflection off a single interface is used, for instance from a metallic surface, or from total internal reflection at the boundary between two dielectrics. The second scheme is to use microstructures periodically patterned on the scale of the resonant optical wavelength, for instance a planar multilayer Bragg reflector with high reflectivity, or a photonic crystal [4].

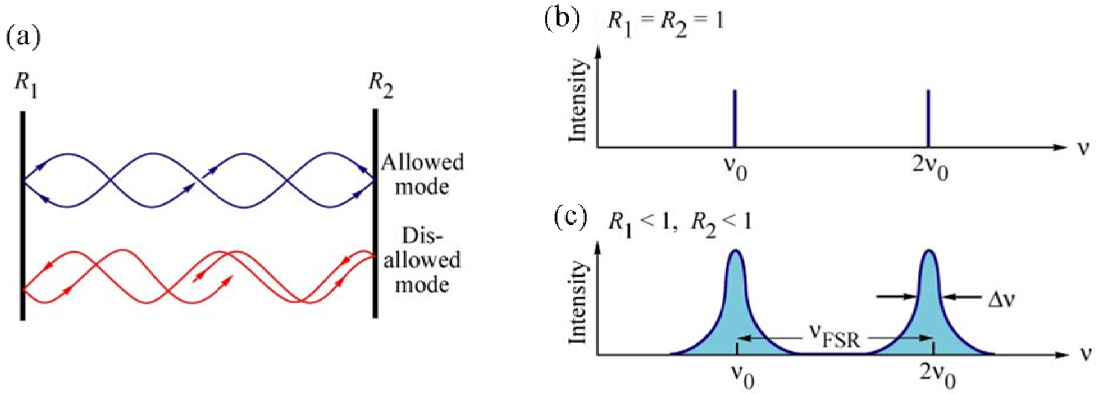

FIG. 1.7: (a) Schematic illustration of allowed and disallowed optical modes in a Fabry-Perot cavity consisting of two coplanar reflectors. Optical mode density for a resonator with (b) no mirror loses (R1=R2=100%) and (c) mirror loses [35].

The simplest way to confine a photon is a Fabry-Perot resonator. It is a resonant cavity formed by two parallel reflecting mirrors separated by a medium such as air or gas. When the mirrors are aligned perfectly parallel to each other (planar cavity), the reflections of the light waves between the two mirrors interfere constructively and destructively, giving rise to a standing wave pattern between the mirror surfaces (cavity modes), just like standing waves on a string. For standing waves, any wavelengths that are not an integer multiple of half a wavelength will interfere destructively. This is shown below in Figure 7 (a), (b). The standing waves therefore must satisfy the condition: $m(\lambda/2) = L$ (1.14).

In the case of oblique incidence of light (see Fig.8), multiple reflections of light between the two reflecting surfaces arise, which constructively interfere if the transmitted beams are in phase, corresponding to a high-transmission peak of the cavity.

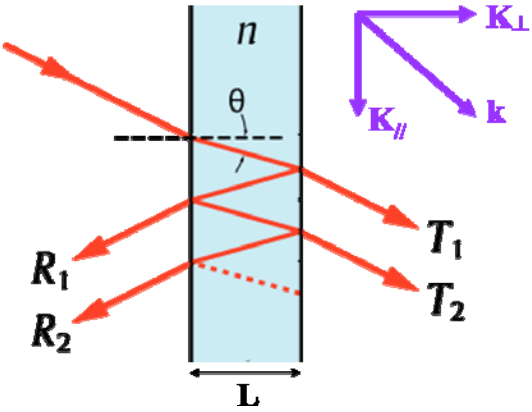

FIG. 1.8: schematic illustration of the multiple reflections and transmissions of a light beam when being incident to a thin film at an angle θ relatively to normal incidence.

If the transmitted beams are out-of-phase, destructive interference occurs and this corresponds to a transmission minimum. Whether the multiply-reflected beams are in-phase or not depends on the wavelength (λ) of the light (in vacuum), the angle the light travels through the etalon (*θ*), the thickness of the cavity (*L*) and the refractive index of the material between the reflecting surfaces (*n*). The phase difference between each succeeding reflection is given by δ:

$$\delta = \left(\frac{2\pi}{\lambda}\right) 2n\ell\cos\theta, \quad (1.15)$$

The transmittance and reflectance functions of the cavity are given by:

$$T = \frac{(1-R_1)(1-R_2)}{[1-\sqrt{R_1R_2}]^2 + 4\sqrt{R_1R_2}\sin^2\delta}, \quad (1.16)$$

$$R = \frac{[1-\sqrt{R_1R_2}]^2 + 4\sqrt{R_1R_2}\sin^2\delta - (1-R_1)(1-R_2)}{[1-\sqrt{R_1R_2}]^2 + 4\sqrt{R_1R_2}\sin^2\delta}, \quad (1.17).$$

This occurs when the path-length difference is equal to half an odd multiple of the wavelength. The wavelength separation between adjacent transmission/reflection peaks, as depicted in figure 9, is called the free spectral range (FSR) of the cavity, Δλ, and is given by:

$$\Delta\lambda = \frac{\lambda_0^2}{2n\ell\cos\theta + \lambda_0} \approx \frac{\lambda_0^2}{2n\ell\cos\theta}, \quad (1.18)$$

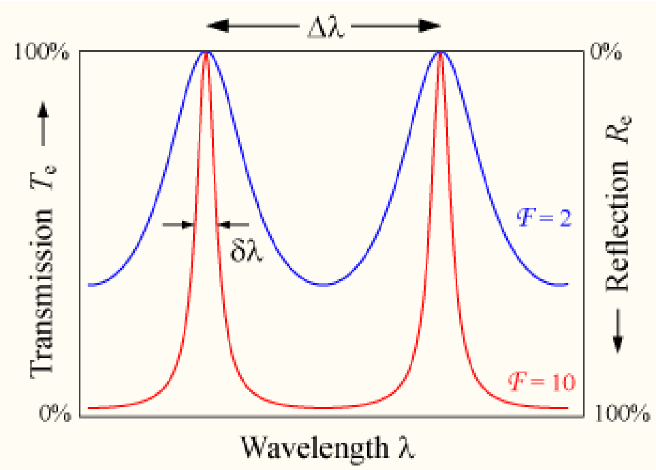

FIG. 1.9: Transmission and reflectivity spectra corresponding to different cavity finesse values for the same spectral reange [36].

where λ_0 is the central wavelength of the nearest transmission peak. The FSR is related to the full-width half-maximum (FWHM) δλ, of any one transmission band by a quantity known as the *finesse*:

$$F = \frac{\Delta\lambda}{\delta\lambda} = \frac{\pi(\sqrt{R_1 R_2})^{1/2}}{1-\sqrt{R_1 R_2}} \quad , \quad (1.19)$$

a useful tool which gives a quick indication of the sharpness and the overlapping of the peaks. Larger mirror reflectivities lead to larger ***finesses*** and to sharper peaks.

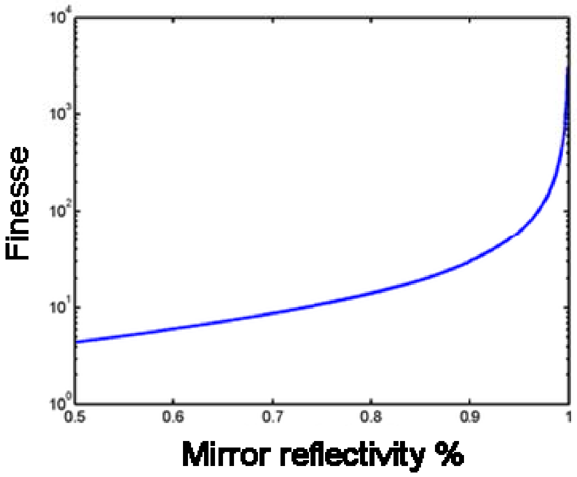

FIG. 1.10: Finesse as a function of reflectivity. Very high finesse factors require highly reflective mirrors [36].

Another tool of measuring the sharpness of the transmission/reflectivity peaks is the cavity quality factor Q. It is defined as the ratio of the resonance wavelength λ_0 to the the full-width half-maximum (FWHM) δλ.

$$Q = \frac{\lambda_0}{\Delta\lambda} \quad , \quad (1.20)$$

Q-factor comprises a measure of the rate at which optical energy decays from within the cavity (from absorption, scattering or leakage through the imperfect mirrors) and Q^{-1} is the fraction of energy lost in a single round-trip around the cavity. Equivalently, the exponential decay photon number has a lifetime given by

$$\tau = Q/\lambda, \ (1.21).$$

Strongly coupled microcavities need high Q-factors to minimize the energy loss and preserve a long lasting cavity mode, available for coupling to an exciton.

References

[1] R. Loudon, *The Quantum Theory of Light*, 3rd ed. Oxford University Press, USA, 2000.

[2] Y. Yamamoto, F. Tassone, and H. Cao, *Semiconductor cavity quantum electrodynamics*. Springer, 2000.

[3] C. Weisbuch, H. Benisty, and R. Houdré, “Overview of fundamentals and applications of electrons, excitons and photons in confined structures,” *Journal of Luminescence*, vol. 85, no. 4, pp. 271-293, Jan. 2000.

[4] A. Kavokin, J. J. Baumberg, G. Malpuech, and F. P. Laussy, *Microcavities*. Oxford University Press, USA, 2008.

[5] S. Tsintzos, P. Savvidis, G. Deligeorgis, Z. Hatzopoulos, and N. Pelekanos, “Room temperature GaAs exciton-polariton light emitting diode,” *Applied Physics Letters*, vol. 94, no. 7, 2009.

[6] S. I. Tsintzos, N. T. Pelekanos, G. Konstantinidis, Z. Hatzopoulos, and P. G. Savvidis, “A GaAs polariton light-emitting diode operating near room temperature,” *Nature*, vol. 453, no. 7193, pp. 372-375, May. 2008.

[7] S. Christopoulos et al., “Room-Temperature Polariton Lasing in Semiconductor Microcavities,” *Physical Review Letters*, vol. 98, no. 12, p. 126405, Mar. 2007.

[8] L. S. Dang, D. Heger, R. André, F. Boeliguf, and R. Romestain, “Stimulation of Polariton Photoluminescence in Semiconductor Microcavity,” *Physical Review Letters*, vol. 81, no. 18, p. 3920, Nov. 1998.

[9] P. G. Savvidis, J. J. Baumberg, R. M. Stevenson, M. S. Skolnick, D. M. Whittaker, and J. S. Roberts, “Angle-Resonant Stimulated Polariton Amplifier,” *Physical Review Letters*, vol. 84, no. 7, p. 1547, Feb. 2000.

[10] C. Ciuti, P. Schwendimann, B. Deveaud, and A. Quattropani, “Theory of the angle-resonant polariton amplifier,” *Physical Review B*, vol. 62, no. 8, p. R4825, 2000.

[11] C. Ciuti, P. Schwendimann, and A. Quattropani, “Parametric luminescence of microcavity polaritons,” *Physical Review B*, vol. 63, no. 4, p. 041303, Jan. 2001.

[12] M. Saba et al., “High-temperature ultrafast polariton parametric amplification in semiconductor microcavities,” *Nature*, vol. 414, no. 6865, pp. 731-735, Dec. 2001.

[13] J. J. Baumberg et al., “Parametric oscillation in a vertical microcavity: A polariton condensate or micro-optical parametric oscillation,” *Physical Review B*, vol. 62, no. 24, p. R16247, Dec. 2000.

[14] R. M. Stevenson et al., “Continuous Wave Observation of Massive Polariton Redistribution by Stimulated Scattering in Semiconductor Microcavities,” *Physical Review Letters*, vol. 85, no. 17, p. 3680, Oct. 2000.

[15] C. Diederichs et al., “Parametric oscillation in vertical triple microcavities,” *Nature*, vol. 440, no. 7086, pp. 904-907, Apr. 2006.

[16] D. Porras, C. Ciuti, J. J. Baumberg, and C. Tejedor, “Polariton dynamics and Bose-Einstein condensation in semiconductor microcavities,” *Physical Review B*, vol. 66, no. 8, p. 085304, 2002.

[17] G. Malpuech, A. Di Carlo, A. Kavokin, J. J. Baumberg, M. Zamfirescu, and P. Lugli, “Room-temperature polariton lasers based on GaN microcavities,” *Applied Physics Letters*, vol. 81, no. 3, p. 412, 2002.

[18] J. Kasprzak et al., “Bose-Einstein condensation of exciton polaritons,” *Nature*, vol. 443, no. 7110, pp. 409-414, 2006.

[19] H. Deng et al., “Quantum Degenerate Exciton-Polaritons in Thermal

Equilibrium," *Physical Review Letters*, vol. 97, no. 14, p. 146402, Oct. 2006.

[20] L. V. Butov, "Solid-state physics: A polariton laser," *Nature*, vol. 447, no. 7144, pp. 540-541, May. 2007.

[21] I. Carusotto and C. Ciuti, "Probing Microcavity Polariton Superfluidity through Resonant Rayleigh Scattering," *Physical Review Letters*, vol. 93, no. 16, p. 166401, Oct. 2004.

[22] A. Kavokin, G. Malpuech, and F. P. Laussy, "Polariton laser and polariton superfluidity in microcavities," *Physics Letters A*, vol. 306, no. 4, pp. 187-199, Jan. 2003.

[23] R. Houdré, C. Weisbuch, R. P. Stanley, U. Oesterle, P. Pellandini, and M. Ilegems, "Measurement of Cavity-Polariton Dispersion Curve from Angle-Resolved Photoluminescence Experiments," *Physical Review Letters*, vol. 73, no. 15, p. 2043, Oct. 1994.

[24] W. Y. Liang, "Excitons," *Physics Education*, vol. 5, no. 4, pp. 226-228, 1970.

[25] M. Pope and C. E. Swenberg, *Electronic Processes in Organic Crystals and Polymers*, 2nd ed. Oxford University Press, 1999.

[26] K. Kornitzer et al., "Photoluminescence and reflectance spectroscopy of excitonic transitions in high-quality homoepitaxial GaN films," *Physical Review B*, vol. 60, no. 3, p. 1471, Jul. 1999.

[27] V. Savona, L. C. Andreani, P. Schwendimann, and A. Quattropani, "Quantum well excitons in semiconductor microcavities: Unified treatment of weak and strong coupling regimes," *Solid State Communications*, vol. 93, no. 9, pp. 733-739, Mar. 1995.

[28] V. Savona, Z. Hradil, A. Quattropani, and P. Schwendimann, "Quantum theory of quantum-well polaritons in semiconductor microcavities," *Physical Review B*, vol. 49, no. 13, p. 8774, Apr. 1994.

[29] V. Savona, F. Tassone, C. Piermarocchi, A. Quattropani, and P. Schwendimann, "Theory of polariton photoluminescence in arbitrary semiconductor microcavity structures," *Physical Review B*, vol. 53, no. 19, p. 13051, May. 1996.

[30] V. Savona, "Strong coupling of exciton-polaritons in semiconductor microcavities," *Journal of Crystal Growth*, vol. 184, pp. 737-744, Feb. 1998.

[31] C. F. Klingshirn, *Semiconductor Optics*, 3rd ed. Springer, 2006.

[32] G. Khitrova, H. M. Gibbs, F. Jahnke, M. Kira, and S. W. Koch, "Nonlinear optics of normal-mode-coupling semiconductor microcavities," *Reviews of Modern Physics*, vol. 71, no. 5, p. 1591, Oct. 1999.

[33] D. S. Chemla and D. A. B. Miller, "Room-temperature excitonic nonlinear-optical effects in semiconductor quantum-well structures," *Journal of the Optical Society of America B*, vol. 2, no. 7, pp. 1155-1173, Jul. 1985.

[34] B. Zhang, S. Kano, Y. Shiraki, and R. Ito, "Oscillator Strength of Excitons in InGaAs/GaAs Quantum Wells," *Journal of the Physical Society of Japan*, vol. 62, pp. 3031-3034, 1993.

[35] E. F. Schubert, *Light-emitting diodes*. Cambridge University Press, 2006.

[36] http://en.wikipedia.org/wiki/Fabry%E2%80%93P%C3%A9rot_interferometer

Chapter 2: Physics of Polariton Microcavities

2.1 Structure of a Planar Microcavity

As mentioned in the previous chapter, microcavities are photonic structures which combine the *confinements* of *bound electron-hole pairs (excitons)* and *photons* (*cavity modes*) for the control of light-matter interactions.

A planar microcavity is an optical Fabry-Perot resonator in the centre of which an optically active material (inorganic, organic or hybrid) is incorporated. Its mirrors can either be distributed Bragg reflectors (DBRs) or metallic ones.

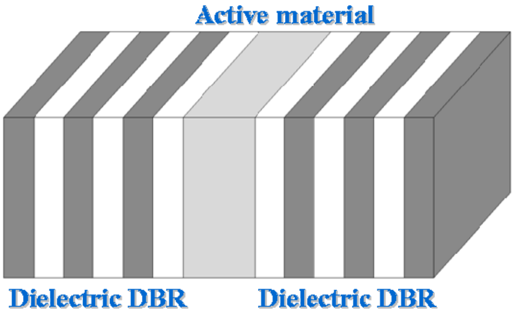

FIG. 2.1. Structure of a planar microcavity.

A DBR is also a planar structure made of stacks of semiconductor (or dielectric) layers with two alternating refraction indices n_1, and n_2. Provided the N number of pairs is sufficiently high, DBRs present a wavelength interval centred at λ_c (ω_S frequency), called *stop band*, in which the square modulus of the reflection coefficient at normal incidence is very close to unity ($R_{DBR} = |r|^2_{DBR}$ ~1). When the optical thickness of each layer is $\lambda/4$ ($\lambda = \lambda_{air}/n$) all Fresnel reflections add in phase and the transmitivity of the mirror decreases approximately exponentially as a function of the mirror thickness (or the number of alternating dielectric layers) [1]. The typical microcavity is made of a semiconducting layer called *spacer* which is placed between two DBRs, defining the cavity length as an integer multiple of lamda half $L_c = m\lambda/2$, a condition that gives an antinode of the electric field at the centre of the cavity (symmetric microcavity).

In a λ -cavity (m=2) the spacer has thickness λ , corresponding to the wavelength of the excitonic transition. In this configuration the mirrors, the spacer, and the exciton mode are characterized by the same optical wavelength and the system is said to be at resonance [2].

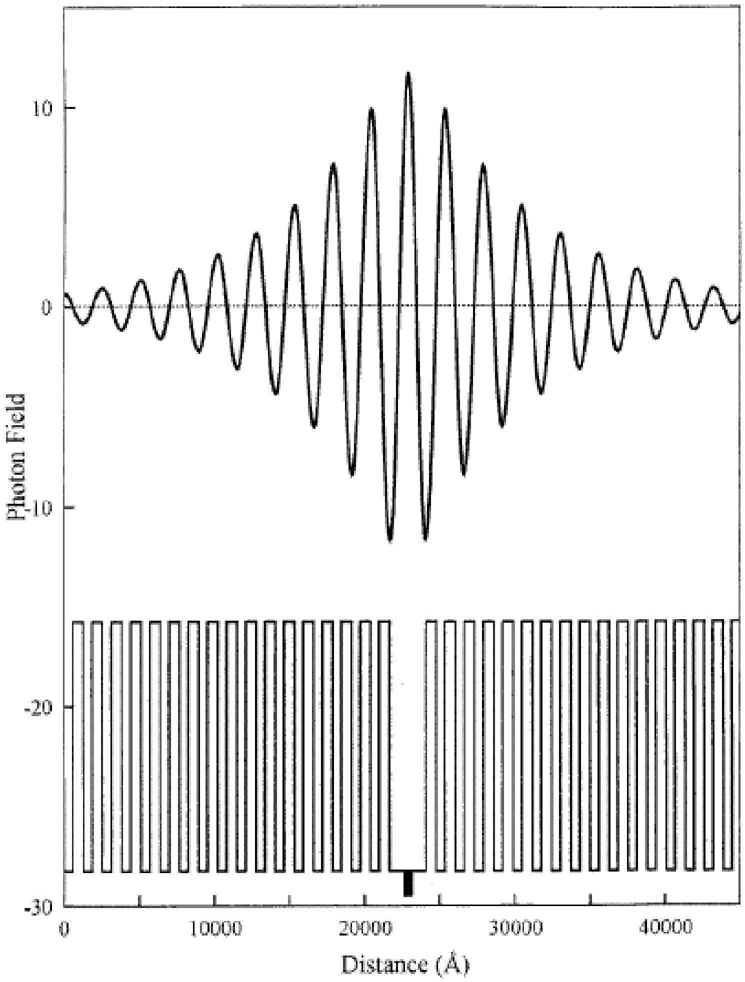

FIG. 2.2 Calculated photon field distribution for microcavity. The optical field enhancement in the cavity region is visible. The refractive index profile (multiplied by 1) of the cavity plus DBRs is also shown [2].

However, as shown in [3], [4], there is a penetration of the cavity field into the DBR which means that, in some of the formulae, the Fabry–Perot cavity length has to be replaced by a significantly larger effective length $L_{eff} = L_c + L_{DBR}$, (2.1), where

$$L_{DBR} = \frac{\lambda}{2n_c} \frac{n_1 n_2}{n_2 - n_1}, \quad n_1 < n_2, \quad (2.2)$$

This means that the microcavity frequency should also be modified according to the following equation:

$$\omega_{microcav} = \frac{L_c \omega_c(\theta) + L_{DBR}\omega_s(\theta)}{L_{eff}(\theta)}, \quad (2.3)$$

where $\omega_c = m\pi c/(n_c L_c \cos\theta_c)$ is the Fabry-Perot cavity frequency if there is no phase delay in the mirrors. The angle θ_c in the cavity is related to the external angle θ of light incidence by $\sin\theta_c = \sin\theta / n_c$, where n_c is the Fabry-Perot cavity refractive index. In most cases L_{DBR} is much larger than L_c and the cavity mode (standing wave of the Fabry-Perot cavity) is mostly determined by the center of the DBR stop band [2], [3].

2.2 Light-Matter Interactions in a Microcavity

When photonic modes of the cavity are resonant with the optical transitions of the active material new physical phenomena arise, such as the weak and strong coupling of exciton and photon.

In weak coupling regime the cavity mode and the emission overlap. In the strong coupling regime the cavity mode and the absorption of a dipole (exciton) are in superposition. This coupling of a photon and exciton creates a new quasi-particle called cavity polariton. It can be understood as a state oscillating between being an exciton and a photon (half light-half matter). At resonance, the cavity modes strongly coupled to excitons of the same energy and in-plane momentum, split into two modes called upper and lower polarion modes, with equal intensity transitions. Their energy gap is called Rabi splitting Ω and expresses how strong light and matter are coupled.

Cavity polaritons can be observed when the product of the optical attenuation coefficient α and the cavity layer thickness L overcomes the losses of the resonator with mirror reflectivities R_1 and R_1 respectively: $aL >> 1 - \sqrt{R_1 R_2}$ [5], [6]. This is when the vacuum Rabi splitting is greater than the linewidth difference between the cavity and exciton modes, yielding a measurable splitting of two polariton branches in the optical spectrum.

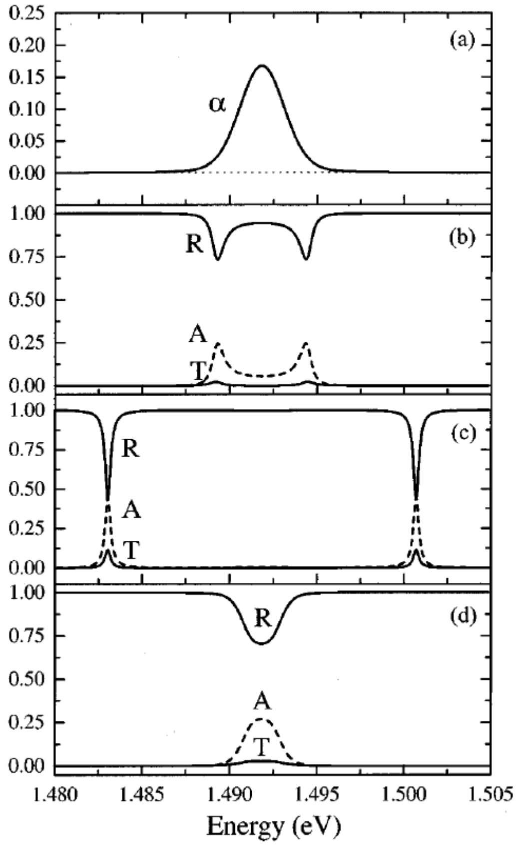

FIG. 2.3. Symmetrically inhomogeneously broadened oscillator: (a) absorption coefficient; (b)–(d) Corresponding θ=0 NMC transmission (*T*, solid lines), reflection (*R*, solid lines), and absorption (*A*, dashed lines) spectra for (b) splittings of 5 meV; (c) splittings of 17.6 meV; (d) splittings of 2 meV [4].

2.2.1 Semi-classical Polariton Model

A simple model to describe polaritons is treating the cavity and photon modes as coupled oscillators, with a coupling matrix element $V = \hbar\Omega/2$. This captures most of the essential physics of the cavity polaritons and has the advantage of being simple enough to solve analytically. The various parameters, such as the vacuum Rabi splitting and the cavity and photon mode widths, are treated phenomenologically, to be obtained either by separate calculation or from fitting to experimental data [2].

The coupled oscillator model can readily be used to calculate microcavity in-plane k_{II} dispersions [7]. To do this, the uncoupled exciton and cavity photon energies are made *k* dependent according to their dispersions. The polariton dispersion is then obtained by solving the coupled oscillator problem for each value of *k*.

In the simple case of a single QW incorporated in a microcavity, the coupling between the exciton and cavity oscillators is described by a 2x2 matrix Hamiltonian:

$$H = \begin{bmatrix} E_{exc}(k) - i\gamma_{exc}(k) - E(k) & \dfrac{\Omega}{2} \\ \dfrac{\Omega}{2} & E_{ph}(k) - i\gamma_{ph}(k) - E(k) \end{bmatrix}, \quad (2.4)$$

where k is the wave vector, $E_{exc}(k)$ and $E_{ph}(k)$ are the uncoupled exciton and photon mode energy respectively, Ω is the Rabi splitting coupling strength and γ_{exc} and γ_{ph} are the linewidths of exciton and photon mode respectively which act as damping parameters of the individual oscillators. This Hamiltonian is easily diagonalized to an equation of two damped coupled oscillators

$$(E_{ex} - E - i\gamma)(E_{ph} - E - i\gamma_{ph}) = V^2, \quad (2.5)$$

where $E_{ph} - i\gamma_{ph}$ is the complex eigenfrequency of the cavity mode in the absence of exciton–photon coupling, providing its two complex solutions-Hamiltonian eigenvalues [3], [8], [9].

$$E_{LP}^{UP} = \frac{E_{ex} + E_{ph}}{2} - \frac{i}{2}(\gamma_{ex} + \gamma_{ph}) \pm \sqrt{V^2 + \frac{1}{4}\left(E_{ex} - E_{ph} - i(\gamma_{ex} - \gamma_{ph})\right)^2}, \quad (2.6)$$

The matrix element *V* has the sense of the coupling strength between the cavity photon mode and the exciton, which is directly correlated to the exciton's binding energy and oscillator strength in the simple case of a quantum well incorporated in the cavity [3].

$$V(\theta) = \left(\frac{1}{4\pi\varepsilon_0} \frac{2\pi e^2 f_{xy}}{n_c^2 m L_{eff}(\theta)} \right)^{1/2}, \quad (2.7)$$

where θ is the angle of the emitted polaritons, n_c is the cavity medium refractive index, $L_{eff}(\theta)$ is the effective cavity length and f_{xy} the exciton oscillator strength per unit surface of the quantum well.

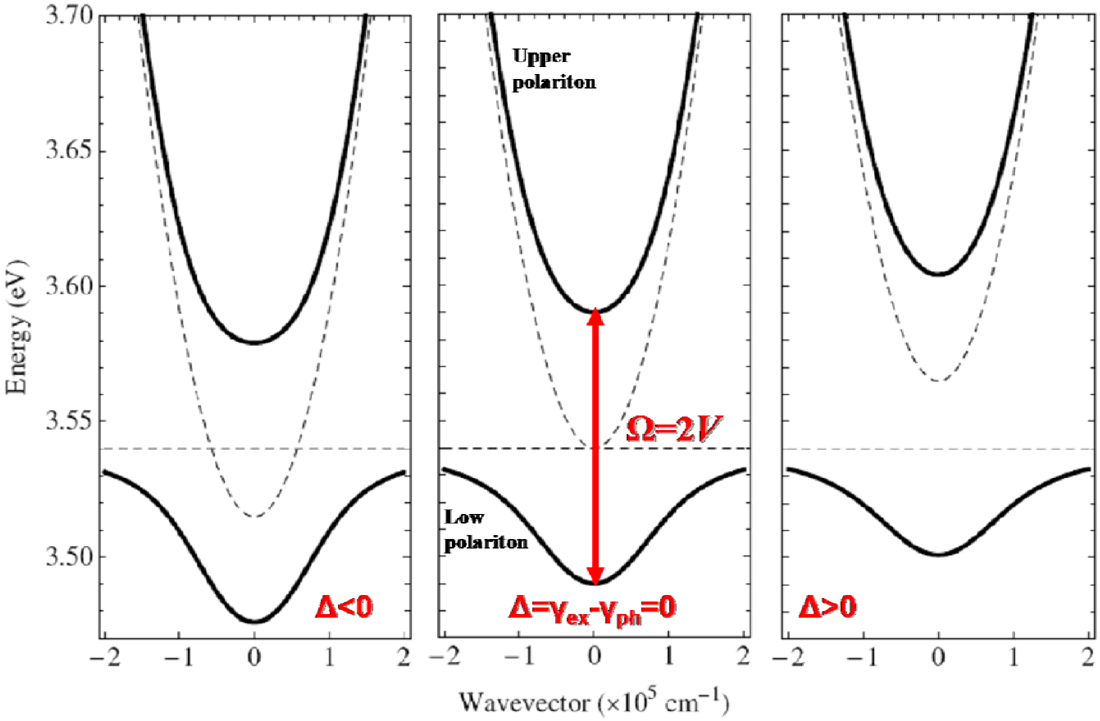

FIG. 2.4. Energies of exciton-polaritons at (a) negative, (b) zero and (c) positive detuning between the bare photon and exciton modes. Solid lines show the inplane dispersion of exciton-polariton modes. Dashed lines show the dispersion of the uncoupled exciton and photon modes. The calculations have been made with parameters typical of a GaN microcavity, from Kavokin and Gil (1998), with a photon mass of 0.5×10−4m0 and a Rabi splitting of 50 meV [9].

At resonance ($E_{ex} = E_{ph}$), the solutions of the diagonalized Hamiltonian are given by

$$E_{LP}^{UP} = E_{ex} - \frac{i}{2}(\gamma_{ex} + \gamma_{ph}) \pm \sqrt{V^2 + \frac{1}{4}(\gamma_{ex} - \gamma_{ph})^2}\,, \quad (2.8)$$

The Rabi splitting Ω between the two polariton branches is given by

$$\Omega = \sqrt{4V^2 - (\gamma - \gamma_c)^2}\,, \quad (2.9)$$

which is related to the exciton's oscillator strength f_{xy} , binding energy and both photon and exciton linewidths.

2.2.2 Strong Coupling

When the condition $V > |\gamma - \gamma_c| / 2$, (2.10) is satisfied, anticrossing of the two solutions E^{UP}-upper polariton (UP) and E_{LP}-lower polariton (LP) dispersion curves takes place between the exciton and photon modes, which is characteristic of the *strong-coupling regime*. In this regime, two distinct exciton-polariton branches manifest themselves as two optical resonances in the reflection or transmission spectra. The splitting between these two resonances is referred to as the *vacuum-field Rabi splitting* Ω. It reaches 4–15 meV in state of the art GaAs-based microcavities, up to 30 meV in CdTe-based microcavities, and is found to be as large as 50 meV in GaN microcavities [9].

In the strong coupling regime, where the vacuum Rabi splitting is greater than the widths of the cavity and exciton modes, this corresponds to a measurable splitting in the optical spectrum when the two modes anticross. Two spectral features due to mixed polariton modes are observed: (a) on resonance, the two polariton modes arise from symmetric and antisymmetric combinations of the exciton and cavity modes. (b) Away from resonance, only the cavity mode couples directly to external photons so, the predominantly excitonic mode becomes weak.

Figures 4 shows a typical polariton dispersion calculated in this way, for a structure on resonance at $k_{\amalg} = 0$. Around $k_{\amalg} = 0$, the polariton mass in both branches is approximately twice the effective mass of the photon. However, since the dispersions of the photon and exciton are very different, varying *k* moves the system away from resonance, with the lower branch becoming more massive and exciton like, the upper branch more photon like. Such polariton dispersions were first measured in angle tuning experiments by Houdre *et al* [10].

One of the most important features of Hamiltonian given above is the inclusion of broadening. This is most obviously done by adding an imaginary part to the exciton and photon energies, corresponding to a homogeneous, or lifetime, broadening of the oscillator. For the cavity mode, this is appropriate, as the linewidth is believed to be mainly homogeneous, originating from the tunnelling decay of the photon through the mirrors (mirror losses). For the exciton, by contrast, the dominant broadening mechanism is inhomogeneous, because of disorder. The inhomogeneous linewidth of a QW exciton is typically a few meV, while the homogeneous width is at most a small fraction of an meV. Hence it is not really appropriate to treat the exciton linewidth as due to homogeneous broadening. The reason why some sort of broadening needs to be included is that the separation of the spectral features is reduced by the broadening, so the measured splitting at resonance is less than $\hbar\Omega$ [6].

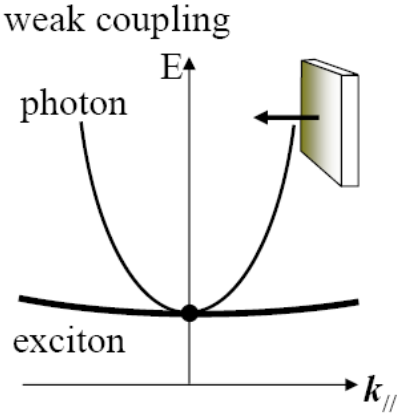

FIG. 2.5. Weak coupling dispersion curve. The exciton and photon dispertion curves cross.

In contrast to strong coupling, when the condition $V < |\gamma - \gamma_c|/2$, (2.11) is satisfied, the weak-coupling regime holds, which is characterized by crossing of the exciton and photon modes and an increase of the exciton decay rate at the resonance point. This regime is typically used in vertical-cavity surface-emitting lasers (VCSELs). The corresponding photon and exciton dispersion curves are described by the following equations:

$$E_{photon}(k_{II}) = \frac{\hbar c}{n_c}\sqrt{\left(\frac{2\pi}{L_c}\right)^2 + k_{II}^2}\,, \quad (2.12)$$

$$E_{exciton}(k_{II}) = E(0) + \frac{\hbar^2 k_{II}^2}{2M_{exciton}}\,, \quad (2.13)$$

2.3 Excitons vs e-h Plasma

Keeping a robust polariton at room temperature is directly related to the exciton's robustness. Its binding energy and oscillator strength should be large at these conditions. These two factors strongly affect the Rabi splitting Ω of upper and lower polariton branches as mentioned in the previous paragraph. However, this is not the only key element for strong light-matter coupling. The relative difference of exciton and photon linewidths γ_{exc} and γ_c respectively, in comparison to the coupling strength constant V control the microcavity behaviour from weak to strong coupling regime and the polariton appearance [4], [7], [9], [11], [12].

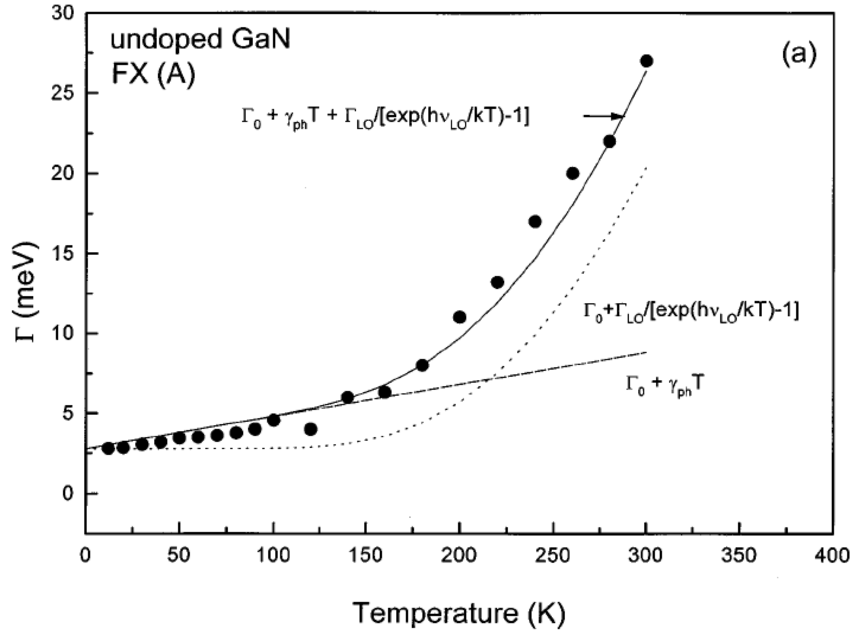

FIG. 2.6. Temperature dependence of the linewidths of free exciton *A* in wurtzite GaN. Solid circles are the experimental points. Solid curve is the fitting of the experimental linewidths considering acoustic-phonon scattering and LO-phonon scattering. Dashed lines show the contribution from the acoustic-phonon scattering alone, and dotted lines show the contribution from the LO phonons only. In both the cases inhomogeneous broadening was added [13].

Exciton linewidth of many semiconducting materials shows an excess of broadening with temperature increase [14-16], [13]. In GaAs system, excitons at 300K survive for a few nanoseconds, producing resonances before being ionized to electron-hole plasma [14], due to severe (LO-phonon)–(exciton) and (acoustic phonon)-(exciton) scattering. Generally, in high-purity crystals, linewidth originates from interactions with thermal phonons, and in polar semiconductors (such as GaN) it is dominated by LO-phonon broadening. But in practice the semiconductor grown by any method has some background impurities, crystal imperfections, and they contribute to inhomogeneous broadening mentioned before. This is represented as Γ_0 in the equation below [13].

$$\gamma_{ex}(T) = \Gamma_0 + \gamma_{ph}T + \Gamma_{LO} / [\exp(\hbar\omega_{LO} / k_B T) - 1], \quad (2.14)$$

At very low temperatures, phonons are not active and the contribution to the linewidth is mainly from inhomogeneous broadening. The best way to obtain Γ_0 is by extrapolation of the linewidth to 0 K. The second and third terms on the right-hand side of Eq. (2.14) are the homogeneous linewidths and are due to acoustic-phonon and LO-phonon scatterings, respectively. Phonons can scatter the exciton to the same bound state or higher-lying bound states. The processes involving acoustic phonons are only intraband scattering of excitons. The contribution due to acoustic phonons increases linearly with temperature T and is represented as $\gamma_{ph}T$, where γ_{ph} is the exciton–acoustic-phonon coupling strength. The last term in Eq. (2.14) arises from interaction of excitons with LO phonons, described by the Frohlich interaction [13], and is proportional to the Bose function for LO-phonon occupation, which is equal to $1/[\exp(\hbar\omega_{LO} / kT - 1)]$, where $\hbar\omega_{LO}$ is the LO-phonon energy and γ_{LO} represents the strength of exciton–LO-phonon coupling.

Figure 2.6 depicts the linewidth temperature dependence of the free *A* exciton in wurtzite GaN. The solid lines are the least-squares fitting considering acoustic-phonon scattering and LO-phonon scattering, in addition to inhomogeneous broadening. The dashed lines show the contribution from acoustic-phonon scattering and the dotted lines show the contribution from the LO phonons to the linewidth. In all cases, the inhomogeneous broadening is also added. It is easily noticeable that the acoustic phonons contribute up to 120 K very significantly, but the contribution from LO phonons is negligible up to this temperature. From 120K onwards the participation of LO phonons causes the linewidth to increase sharply. At 200 K there is a crossover and the LO phonons dominate over the acoustic phonons.

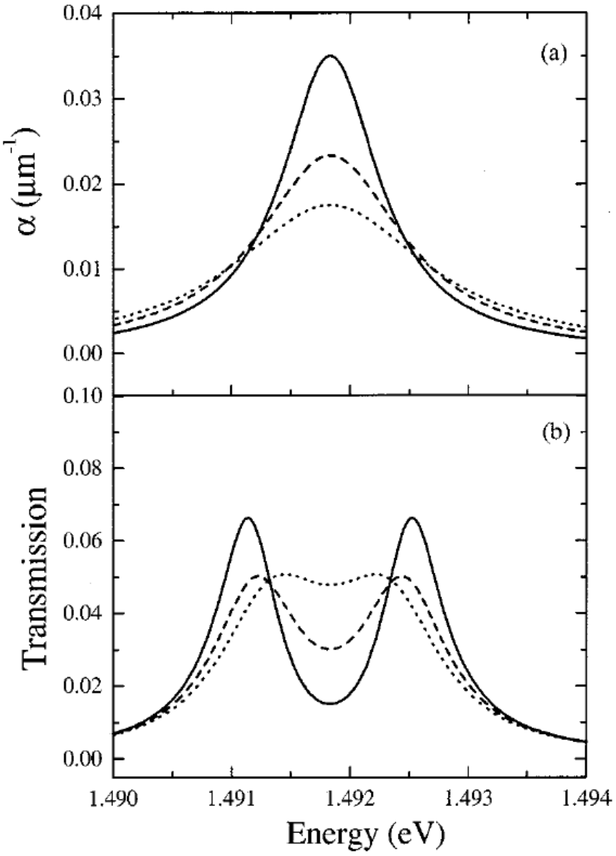

FIG. 2.7. Effect of homogeneous broadening on transmission for barely resolved normal-mode coupling: (a) Oscillator absorption coefficient for a constant oscillator strength and HWHM homogeneous broadenings: solid lines, $\gamma = 0.5$ meV; dashed lines, 0.75 meV; dotted lines, 1.0 meV. (b) Corresponding $\theta = 0$ NMC transmission spectra at zero detuning for [4].

In Figure 2.7, one can see the effect of homogeneous broadening on Rabi splitting Ω. The more the exciton linewidth increases the more the splitting begins to vanish since the strong coupling condition is being marginally satisfied.

On the other hand, the exciton binding energy and oscillator strength for strong coupling applications can be increased by two ways such as exciton confinement or the selection of a material with large oscillator strength. Exciton confinement increases its binding energy by reducing its Bohr radius [17], [14], [15], [18-20].

$$E_{bx}^{3D} = \frac{\hbar^2}{2\mu\alpha_B^2}, \quad (2.15)$$

This confinement is implemented by using quantum wells (QWs) and related strategies, as mentioned in the previous chapter.

Tsintzos et al. [11], [21] have taken advantage of this exciton's property of increasing its binding energy showing a robust polariton emission at 235K and 315K respectively. However this unexpected, from the arsenides system, strong coupling demonstration is on their upper limit of capabilities. The following figure presents the strong decrease of Rabi splitting with temperature due to this characteristic temperature increased broadening of exciton linewidth. This decline creates the motivation for exploring new materials incorporated in microcavities in order to create robust polariton emissions and enhanced splittings for room temperature applications.

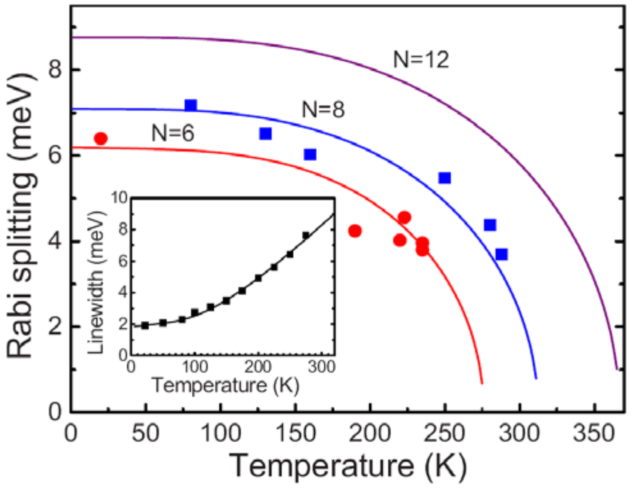

FIG. 2.8. Comparison of theoretical and experimental zerodetuning Rabi splitting as a function of temperature. The circular points refer to MCs with six QWs, while the squares to MCs with eight QWs. Solid lines are theoretical curves for 6, 8, and 12 QWs. The inset shows the temperature dependence of the exciton full width at half maximum linewidth extracted from transmission measurements [11].

Thus, strong coupling arises when exciton binding energy E_{bx} is greater compared to the above mentioned LO-phonon and thermal phonon scatterings ($\gamma_{ex}(T) < k_B T < E_{bx}$), (2.16), where $\hbar\omega_{LO}$ is the LO-phonon energy [14] and big enough to provide a large oscillator strength f_{xy}, forming a large equivalent strong coupling constant V, which in combination to an exciton linewidth γ_{exc} not sufficiently broad does not limit the strong coupling condition $V > |\gamma - \gamma_c|/2$.

2.4 Angle and Cavity Thickness dependent Polariton Properties

A planar cavity provides no confinement perpendicular to its axis, so, just as for electronic states in a QW, the photon has an in-plane dispersion. This can easily be derived by noting that the mirrors force the axial wavevector k_Z in the medium to be quantized to $2\pi/Lc$ [9], [22], [23]. Hence the cavity photon energy is approximately

$$E = \frac{\hbar c}{n_c} k = \frac{\hbar c}{n_c}\left[\left(\frac{2\pi}{L_c}\right)^2 + k_{II}^2\right]^{1/2}, \quad (2.17)$$

This equation provides techniques to probe the cavity polariton dispersion. It is achieved by tuning the cavity length L_c either the in-plane wave vector k_{II}.

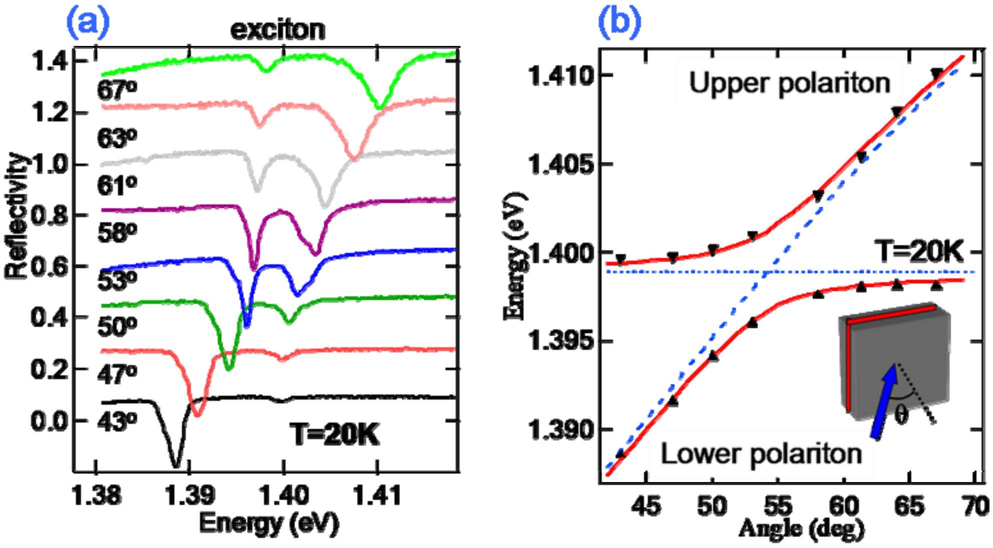

FIG. 2.9. a) Intentionally spaced reflectivity spectras acquired at different angles of incidence at 20K, b) the corresponding polariton dispersion curve with the angle of incidence.

For small k_{II}, this dispersion is parabolic, and so it can be described by a cavity photon effective mass $M = hn_c / cL_c$. This mass is very small, typically ~$10^{-5}m_e$. Such dispersions can be measured directly in angle tuning experiments. Moving away from normal incidence in a reflectivity measurement introduces an in-plane component to the photon wavevector. In-plane wavenumbers up to k_{II} ~ 10^7 m^{-1} can be probed in this way. The energy of a photon with quantized wave vector $k_{II} = 2\pi / L_c$, and in-plane wave vector k_{II} in the medium, is modified to

$$E(k_{II}) = E_0\left(1 + \frac{\hbar^2 c^2 k_{II}^2}{E_0^2 n_{eff}^2}\right)^{1/2}, \quad (2.18)$$

where n_{eff} is the effective refractive index of the structure and $E_0 = hc / n_{eff} L_c$ is the photon energy for $k_{II} = 0$. Each k_{II} in-plane photon mode couples only with exciton states of the same k_{II} to satisfy the requirement of wavevector conservation. The resulting coupled modes, the cavity polaritons, also show strong in-plane dispersion as shown in Figure 2.9. The in-plane wave vector k_{II} is related to the external angle of incidence θ by

$$k_{II} = \frac{E(k)}{\hbar c}\sin\theta, \quad (2.19)$$

and as a result a particular k_{II} mode can be selected simply by varying the external angle of incidence of θ. Elimination of k_{II} between equations (a) and (b) leads to the following expression for the energy of the Fabry–Perot mode as a function of θ:

$$E(\theta) = E_0\left(1 - \frac{\sin^2\theta}{n_{eff}^2}\right)^{-1/2}, \quad (2.20)$$

Tuning of the exciton–cavity interaction can thus be achieved simply by varying θ. Compared with other tuning techniques such as application of external electric or magnetic field, angle tuning has the particular advantage that the exciton energy is independent of angle to a very good approximation.

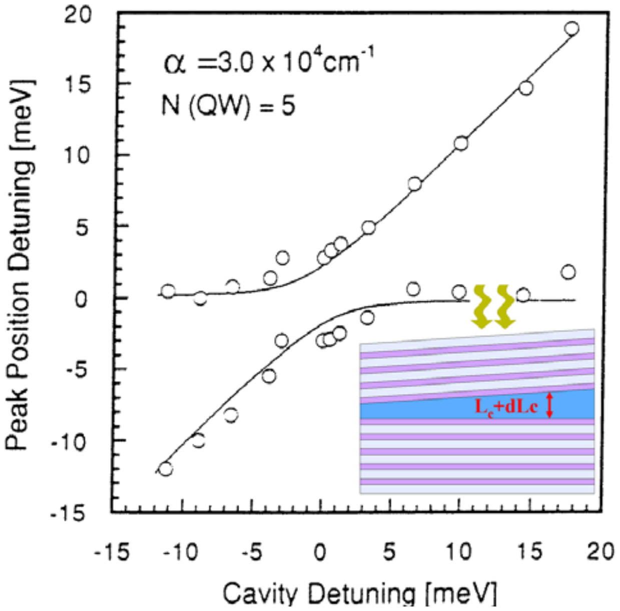

FIG. 2.10. Reflectivity peak positions, and theoretical fit, as a function of cavity detuning for a five-QW sample at T = 5 K. Clear anticrossing behaviour is observed [24].

On the other hand, typical anticrossing in polariton dispertion can be obtained by relying on the variation of cavity thickness L_c across the microcavity surface to tune the cavity mode through the exciton. Such an anticrossing is shown in Figure 2.10.

References

[1] P. Yeh, *Optical Waves in Layered Media*, 2nd ed. Wiley-Interscience, 2005.

[2] M. S. Skolnick, T. A. Fisher, and D. M. Whittaker, Semicond. Sci. Technol. Vol. 13, 645 (1998).

[3] G. Panzarini et al., “Cavity-polariton dispersion and polarization splitting in single and coupled semiconductor microcavities,” *Physics of the Solid State*, vol. 41, no. 8, pp. 1223-1238, 1999.

[4] G. Khitrova, H. M. Gibbs, F. Jahnke, M. Kira, and S. W. Koch, “Nonlinear optics of normal-mode-coupling semiconductor microcavities,” *Reviews of Modern Physics*, vol. 71, no. 5, p. 1591, Oct. 1999.

[5] C. Weisbuch, M. Nishioka, A. Ishikawa, and Y. Arakawa, “Observation of the coupled exciton-photon mode splitting in a semiconductor quantum microcavity,” *Physical Review Letters*, vol. 69, no. 23, p. 3314, Dec. 1992.

[6] Y. Zhu, D. J. Gauthier, S. E. Morin, Q. Wu, H. J. Carmichael, and T. W. Mossberg, “Vacuum Rabi splitting as a feature of linear-dispersion theory: Analysis and experimental observations,” *Physical Review Letters*, vol. 64, no. 21, p. 2499, May. 1990.

[7] V. Savona, “Strong coupling of exciton-polaritons in semiconductor microcavities,” *Journal of Crystal Growth*, vol. 184, pp. 737-744, Feb. 1998.

[8] V. Savona, L. C. Andreani, P. Schwendimann, and A. Quattropani, “Quantum well excitons in semiconductor microcavities: Unified treatment of weak and strong coupling regimes,” *Solid State Communications*, vol. 93, no. 9, pp. 733-739, Mar. 1995.

[9] A. Kavokin, J. J. Baumberg, G. Malpuech, and F. P. Laussy, *Microcavities*. Oxford University Press, USA, 2008.

[10] R. Houdré, C. Weisbuch, R. P. Stanley, U. Oesterle, P. Pellandini, and M. Ilegems, “Measurement of Cavity-Polariton Dispersion Curve from Angle-Resolved Photoluminescence Experiments,” *Physical Review Letters*, vol. 73, no. 15, p. 2043, Oct. 1994.

[11] S. I. Tsintzos, P. G. Savvidis, G. Deligeorgis, Z. Hatzopoulos, and N. T. Pelekanos, “Room temperature GaAs exciton-polariton light emitting diode,” *Applied Physics Letters*, vol. 94, no. 7, p. 071109, 2009.

[12] R. Houdré, R. P. Stanley, U. Oesterle, M. Ilegems, and C. Weisbuch, “Room-temperature cavity polaritons in a semiconductor microcavity,” *Physical Review B*, vol. 49, no. 23, p. 16761, Jun. 1994.

[13] A. K. Viswanath, J. I. Lee, D. Kim, C. R. Lee, and J. Y. Leem, “Exciton-phonon interactions, exciton binding energy, and their importance in the realization of room-temperature semiconductor lasers based on GaN,” *Physical Review B*, vol. 58, no. 24, p. 16333, Dec. 1998.

[14] D. S. Chemla and D. A. B. Miller, “Room-temperature excitonic nonlinear-optical effects in semiconductor quantum-well structures,” *Journal of the Optical Society of America B*, vol. 2, no. 7, pp. 1155-1173, Jul. 1985.

[15] J. H. Chu et al., “Temperature and density dependence of exciton lifetimes in GaAs/AlGaAs multiple quantum wells,” *Optical and Quantum Electronics*, vol. 27, no. 5, pp. 387-393, 1995.

[16] S. Rudin, T. L. Reinecke, and B. Segall, “Temperature-dependent exciton linewidths in semiconductors,” *Physical Review B*, vol. 42, no. 17, p. 11218, Dec. 1990.

[17] T. Shimura and M. Matsuura, “Binding energy and oscillator strength of excitonic molecules in type-II quantum wells,” *Physical Review B*, vol. 56, no. 4,

p. 2109, Jul. 1997.

[18] V. Voliotis, R. Grousson, P. Lavallard, and R. Planel, “Binding energies and oscillator strengths of excitons in thin GaAs/Ga_{0.7}Al_{0.3}As quantum wells,” *Physical Review B*, vol. 52, no. 15, p. 10725, Oct. 1995.

[19] Y. S. Huang et al., “Temperature dependence of the photoreflectance of a strained layer (001) In0.21Ga0.79As/GaAs single quantum well,” *Journal of Applied Physics*, vol. 70, no. 12, p. 7537, 1991.

[20] H. Jeong et al., “Temperature and size dependent excitonic relaxation process in GaAs/AlGaAs quantum wells,” *Solid State Communications*, vol. 85, no. 2, pp. 111-114, 1993.

[21] S. I. Tsintzos, N. T. Pelekanos, G. Konstantinidis, Z. Hatzopoulos, and P. G. Savvidis, “A GaAs polariton light-emitting diode operating near room temperature,” *Nature*, vol. 453, no. 7193, pp. 372-375, May. 2008.

[22] A. Kavokin, “Exciton-polaritons in microcavities: Recent discoveries and perspectives,” *physica status solidi (b)*, vol. 247, no. 8, pp. 1898-1906, 2010.

[23] G. Dasbach, M. Schwab, M. Bayer, D. Krizhanovskii, and A. Forchel, “Tailoring the polariton dispersion by optical confinement: Access to a manifold of elastic polariton pair scattering channels,” *Physical Review B*, vol. 66, no. 20, p. 201201, Nov. 2002.

[24] C. Weisbuch, H. Benisty, and R. Houdré, “Overview of fundamentals and applications of electrons, excitons and photons in confined structures,” *Journal of Luminescence*, vol. 85, no. 4, pp. 271-293, Jan. 2000.

Chapter 3: Design of GaN Microcavities for Room Temperature Operation

3.1 Towards Room Temperature

A polariton strongly coupled microcavity operating at room temperature is of great interest for modern researchers of light-matter interaction scientific field. However this characteristic of polariton microcavities is not trivial to achieve. A key element is to manage to sustain a robust polariton at 300K, in order to be able to fabricate ordinary optoelectronic devices of the future.

In the previous chapter, we have shown the basic requirements for the observation of strong coupling at room temperature, providing the largest possible exciton binding energy and oscillator strength compared to exciton linewidth broadening mechanisms ($\gamma_{ex}(T) < k_B T < E_{bx}$). These characteristics are acquired by selecting the proper materials as active medium of a microcavity (see Fig. 1.4). Materials such as GaN and ZnO are the most suitable inorganic semiconductors whereas j-aggregates and polysilanes are suitable organic semiconducting polymers for realization of microcavites operating at 300K. In this thesis, we focus on GaN and j-aggregate based microcavities.

3.2 Motivation for all-dielectric GaN microcavities

Monolithic growth of GaN based microcavities is extremely challenging due to the build up of mismatch strain and the resulting introduction of structural defects or cracking of the structures [2]. Using lattice matched III-Nitrides alloys for DBR fabrication restricts the refractive index contrast and consequently the width of the mirrors' stopband (see Fig. 3.2(b)), which becomes comparable to the Rabi splitting [3], [4]. At the same time a lot of effort needs to be invested, since a large number of pairs need to be grown with such strain-free BDRs, in order to achieve sufficient reflectivities.

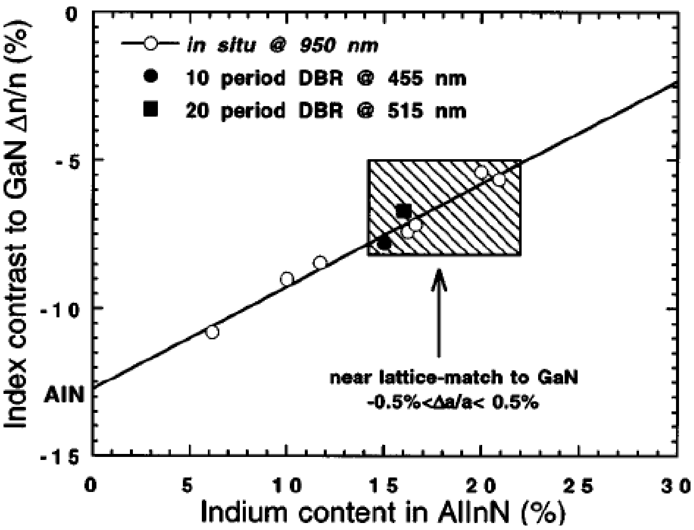

FIG. 3.1. AlInN/GaN optical index contrast versus AlInN indium content, calculated from *in situ* reflectivity experiments (950 nm wavelength) and from *ex situ* analysis of shorter wavelengths DBRs (455 and 515 nm) [1].

To bypass these limitations, several reports have focused on the fabrication of fully dielectric microcavity structures, by either selective wet etching of sacrificial layer [5-7] or mechanical polishing of thicker GaN film to produce membranes [8], [9] [9, 10]. Such High finesse GaN structures with large stopband dielectric distributed Bragg reflectors (DBRs), have been used to demonstrate polariton anticrossing at room temperature, however fabrication challenges remain considerable, particularly due to the optical smoothness requirements of the of GaN membrane surfaces.

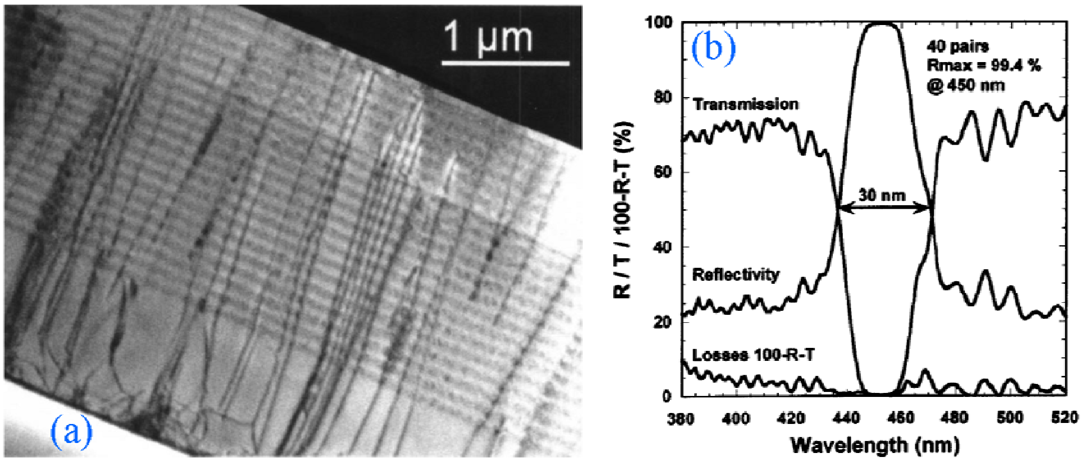

FIG. 3.2. a) TEM image of a 20 pair AlInN–GaN DBR grown on a 1 mm-thick GaN buffer. b) Reflectivity, transmission and losses in a 40 pair AlInN–GaN Bragg reflector [2].

3.3 Excitons in Gallium Nitride

Gallium nitride as a wurzite semiconductor has valence band split into three non-degenerate sub-bands referred to as A, B, and C bands. Correspondingly, we have the A, B and C excitons depicted in Figure 3.3. At room temperature, the *A* and *B* exitons overlap due to phonon broadening to form one peak while the *C* exciton appears as a change in slope. At 77 K, the *A*, *B*, and *C* excitons are clearly resolved showing the excitonic absorption due to the three valence bands [10-14].

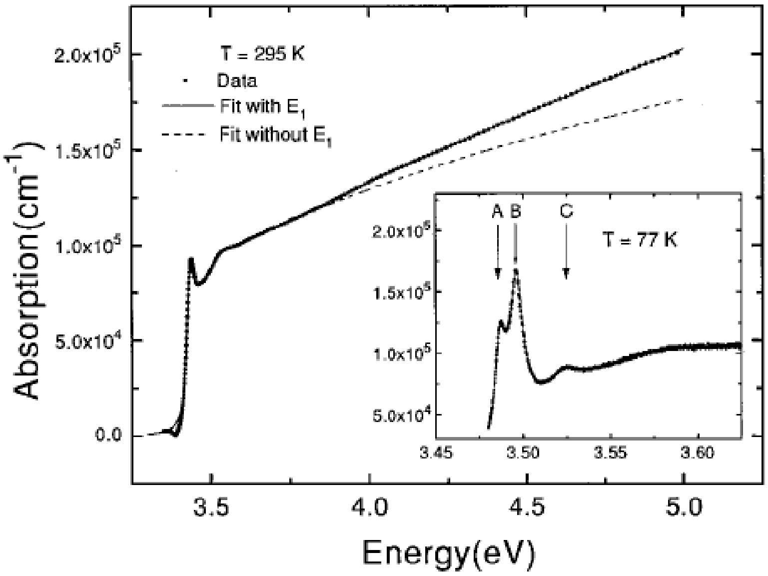

FIG. 3.3. Absorption coefficient dispersion with photon energy for GaN at room temperature. The inset is an expanded view of the excitonic structure at 77 K. At exciton resonance the absorption coefficient is ~10^{-5}cm^{-1} [10].

Gallium nitride A exciton binding energy of ~21meV [10], [12], [13] is larger compared to 4.8meV of bulk GaAs [15-17] and gives GaN a great advantage for showing strong coupling in a microcavity at room temperature. The exciton linewidth is increasing due to the LO-phonon and thermal phonon temperature dependent scatterings, mentioned in the previous chapter. From Figure 3.4(b) we can see that at 300K GaN exciton linewidth is ~25meV, quit broad. However, this is not a disadvantage thanks to GaN exciton robustness at room temperature, due to its high binding energy.

Simultaneously, the exciton's energy red shifts with temperature as demonstrated in Figure 3.4(a), according to Varshni equation, which is used for describing the temperature dependence of band to band transitions. At 300K, GaN exciton's energy is positioned at ~3.44eV [11]. This shift is also verified by temperature resolved white light reflectivity spectras on a c-plane GaN MOCVD remplate, as shown in Figure 3.5.

$$E(T) = E(0) - \frac{aT^2}{(\beta + T)}, \quad \text{(Varshni equation)} \quad (3.1)$$

Experimental and theoretical studies [4], [18-20] have shown that the exciton oscillator strength in GaN is *one order of magnitude larger than in GaAs*. Kavokin et al. [18], have presented a theoretical work on a $\lambda/2$ GaN microcavity, which was solved like a three-oscillator problem, where the cavity modes couples to the two GaN exctions A and B. A giant Rabi splitting of the order of 50meV was shown, growing the expectations for the fabrication of GaN based microcavites.

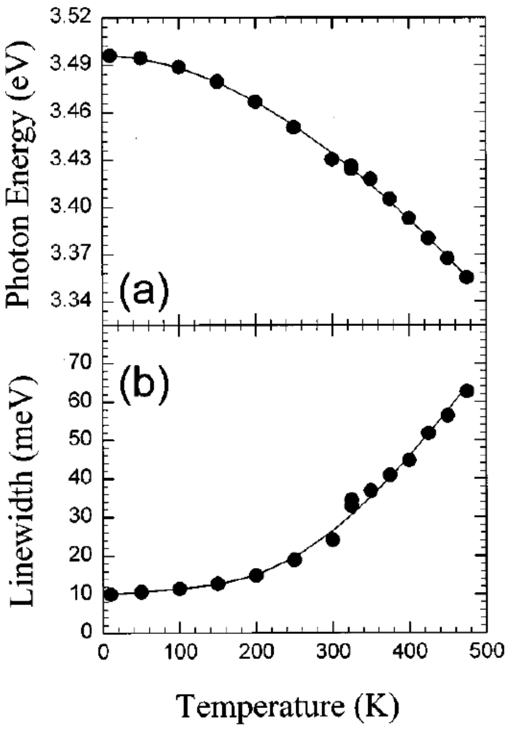

FIG. 3.4. (a) Exciton energy position vs temperature. The solid line is a fit to Varshni equation, (b) Exciton linewidth (FWHM) plotted as a function of temperature. The solid line is a fit to the equation (4) of broadening due to phonon scattering [11].

However, this work did not take into account the fact that at room temperature only the A-exciton, merged with the B-exciton, is robust, as depicted in Figure 3.5.

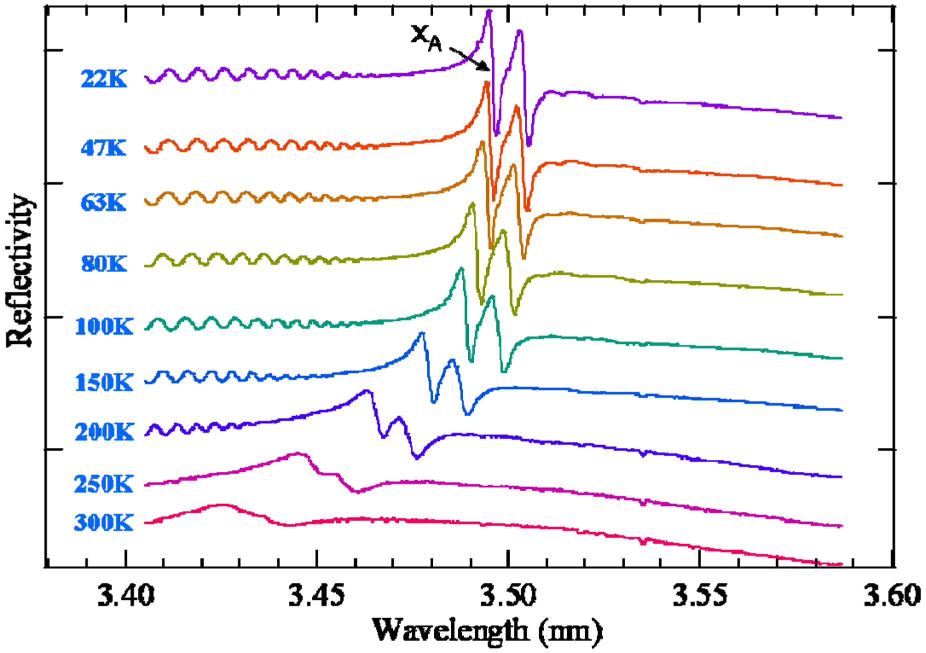

FIG. 3.5. White light reflectivity spectra of an unintentionally doped MOCVD c-plane GaN template, acquired at different temperatures.

Thus, the simulation of an all-dielectric GaN microcavity, operating at room temperature, must be solved as a two-oscillator problem.

3.4 Transfer Matrix Method for GaN microcavity simulation

As shown in Chapter 1, an exciton is described by a Lorentz oscillator, excited by an external electric field. As a result, the semiconducting material that expresses an excitonic transition can be described by a modulated refractive index (see Eq. 1.9). For our simulation, we have used real refractive index dispersion data, derived from ellipsometry experiment, acquired from a 200nm GaN thin film, upon a 50nm InGaN layer, both grown on a standard MOCVD GaN template on sapphire. This specific sample is used for the fabrication of the GaN membranes that are incorporated between dielectric mirrors for the formation of a full dielectric microcavity.

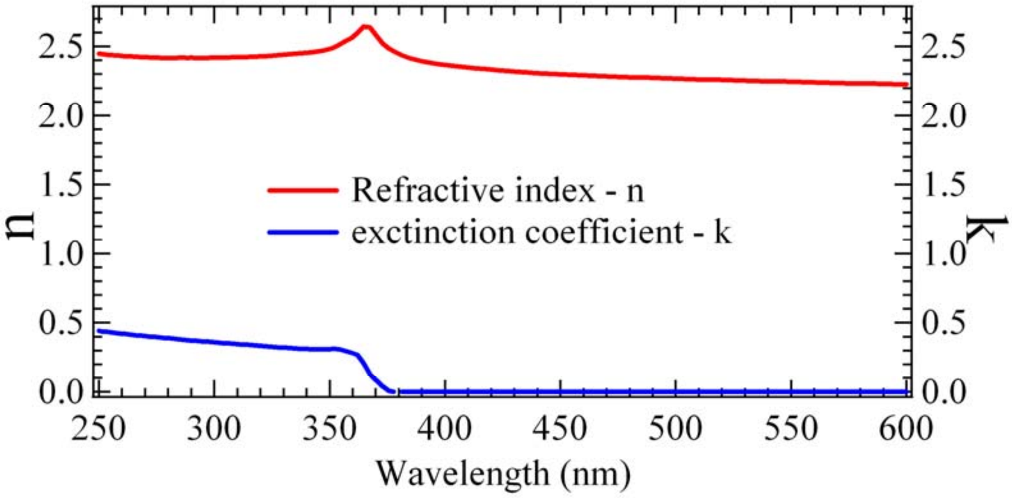

FIG. 3.6. Modulated refractive index and extinction coefficient for Gallium Nitride.

3.4.1 The role of DBRs

Gallium Nitride based microcavities formed by metallic mirrors cannot create the proper conditions for strong coupling. High reflectivities close to 99% are required for vacuum Rabi splitting. The only available technology able to show such reflectivity is that of the *"Distributed Bragg Reflector"* or else DBR. The advantages of Bragg mirrors compared with metallic ones are that they have little loss, their reflectivity can be chosen arbitrarily (by varying the number of layers or the reflective indices of the layers), and if they are epitaxially grown of a semiconducting material, they can be, they can either be electrically insulating or conductive, depending on the doping of the mirror layers. The reflection phase for a wave impinging on the mirror from the spacer is zero at an interface where the refractive index goes from a higher to a lower value, and π at an interface where the refractive index goes from a lower to a higher value. Hence, by putting two mirrors together face to face, a resonant cavity is formed, with standing-wave patterns as schematically outlined in Figure 3.7.

Dielectric DBRs are easier to fabricate using simple evaporation methods such as magnetron and rf sputtering or thermal and e-beam evaporation. However the insertion of a nitride optically active layer in an "all dielectric" optical cavity is not an easy thing to achieve.

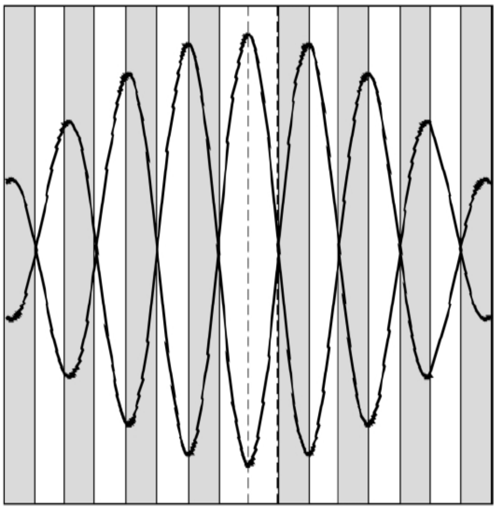

Distributed Bragg Reflectors can be modelled using transfer matrix (TM) simulations. It is the appropriate tool to show light propagation, using only the refractive indexes of the participating to theDBR materials. Transfer Matrix method can also include the active medium of the microcavity, using its modulated refractive index, as seen, for example in Figure 3.6.

FIG. 3.7. Schematic drawing of the standing-wave patterns in a $\lambda/2$ cavity.

This model requires to specify both real and complex part of the refractive indices of the materials for the DBRs and the optically active layer. The number of the pair for each DBR plays also an important role, as expected from the theory.

3.4.2 Quarter-Wave Stack - DBRs

To illustrate the use of the transfer matrix method in the calculation of the reflection and transmission of a multilayer structure, we consider a layered medium consisting of N pairs (period) of alternating quarter waves ($n_1 d_1 = n_2 d_2 = \lambda / 4$), (3.2) with refractive indices n_1 and n_2, respectively. Also, n_0 is the index of refraction of the incident medium and n_s be the index of refraction of the substrate. The reflectance R at normal incidence can be obtained by the following equation:

$$R = |r|^2 = \left| \frac{M_{21}}{M_{11}} \right|^2 , \qquad (3.3)$$

where r is the Fresnel reflection coefficient, described by the matrix elements M_{11} and M_{21} , of the following matrix, which describes the propagation and the refraction of a light beam across a periodic structure like a DBR.

$$\begin{pmatrix} M_{11} & M_{12} \\ M_{21} & M_{22} \end{pmatrix} = D_0^{-1}\left[D_1P_1D_1^{-1}D_2P_2D_2^{-1}\right]^N D_s\,, \qquad (3.4)$$

The propagation matrix for quarter-wave layers (with $\phi_l = \frac{1}{2}\pi$) is given by

$$P_{12} = \begin{pmatrix} i & 0 \\ 0 & -i \end{pmatrix}, \qquad (3.5)$$

The dynamical matrices, which describe the refraction, assuming normal incidence, after some matrix manipulation, are given by

$$D_1P_1D_1^{-1}D_2P_2D_2^{-1} = \begin{pmatrix} \frac{-n_1}{n_2} & 0 \\ 0 & \frac{-n_1}{n_2} \end{pmatrix}, \qquad (3.6)$$

Carrying out the matrix multiplication in equation (3.4) and using the equation (3.3) the reflectance is given by

$$R = \left(\frac{1-(n_s/n_0)(n_1/n_2)^{2N}}{1+(n_s/n_0)(n_1/n_2)^{2N}}\right)^2, \qquad (3.7)$$

The equation can be written as

$$R = \tanh^2(N\ln\frac{n_2}{n_1} + \frac{1}{2}\ln\frac{n_s}{n_a}), \qquad (3.8)$$

For large *N*, the reflectance *R* approaches unity exponentially as a function of *N*. Note that peak reflectance approaches unity as *N* increases.

The bandwidth of the Bragg reflector (stopband) is determined by the forbidden band of the periodic layered structure and is given by

$$\frac{\delta\lambda}{\lambda} = \frac{4}{\pi}\sin^{-1}\frac{|n_2 - n_1|}{n_2 + n_1}, \quad (3.9)$$

The equation above can be written approximately as

$$\frac{\delta\lambda}{\lambda} \approx \frac{2}{\pi}\frac{\Delta n}{n}, \quad (3.10)$$

provided that $n_1 \approx n_2$. Here $\Delta n = |n_1 - n_2|$. Note that the bandwidth of the Bragg reflector is determined by the fractional difference of the index of refraction of the neighboring layers or, equivalently, the fractional index modulation $\Delta n / n$ of the periodic layered medium [21].

3.5 Modeling of all-dielectric GaN microcavity

Modeling all-dielectric nitrides microcavities is important in order to find out what to expect from a real microcavity. For the DBRs, we have picked-up two materials, the most often used for such purposes, the pair of SiO_2/HfO_2. These particular dielectrics are very easy to evaporate in stacks, using e-beam or thermal evaporation and simultaneously are less transparent in the ultraviolet (UV) spectrum, where the nitrides microcavities emit. The modulation of their refractive indexes with wavelength is shown in the following figure.

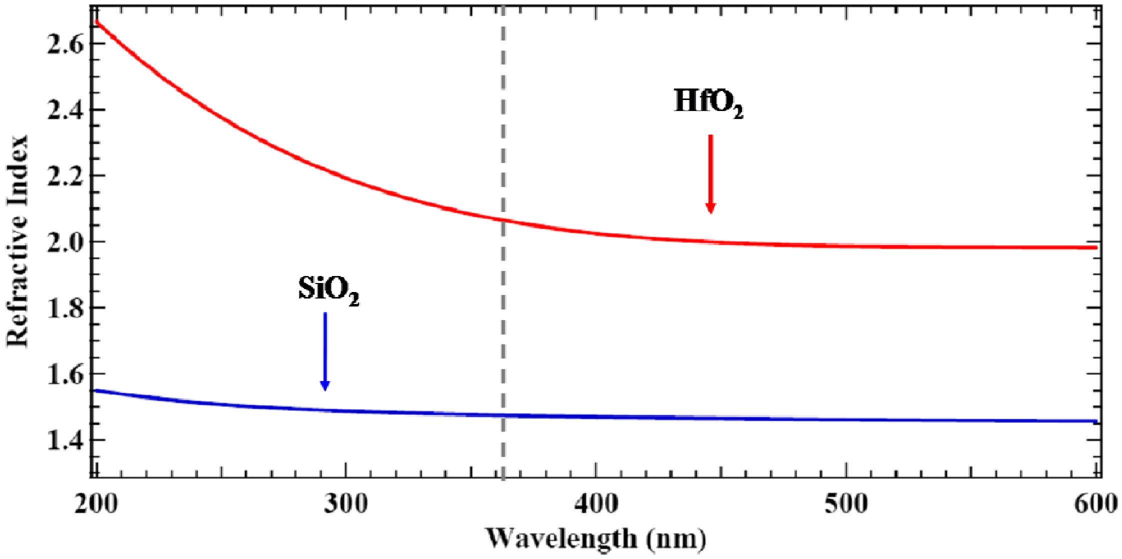

FIG. 3.8. Refractive index dispersion curves for SiO_2 and HfO_2.

The corresponding to these materials refractive indexes on GaN resonance (365nm) are $n_{SiO_2} = 1.475$ and $n_{HfO_2} = 2.067$ respectively, yielding a high refractive index contrast of $\Delta n = 0.592$. This is why this pair of dielectric materials gives us a 77nm stopband (according to Eq. 3.9) when we design a DBR being centered to 365nm, as depicted in Figure 3.9.

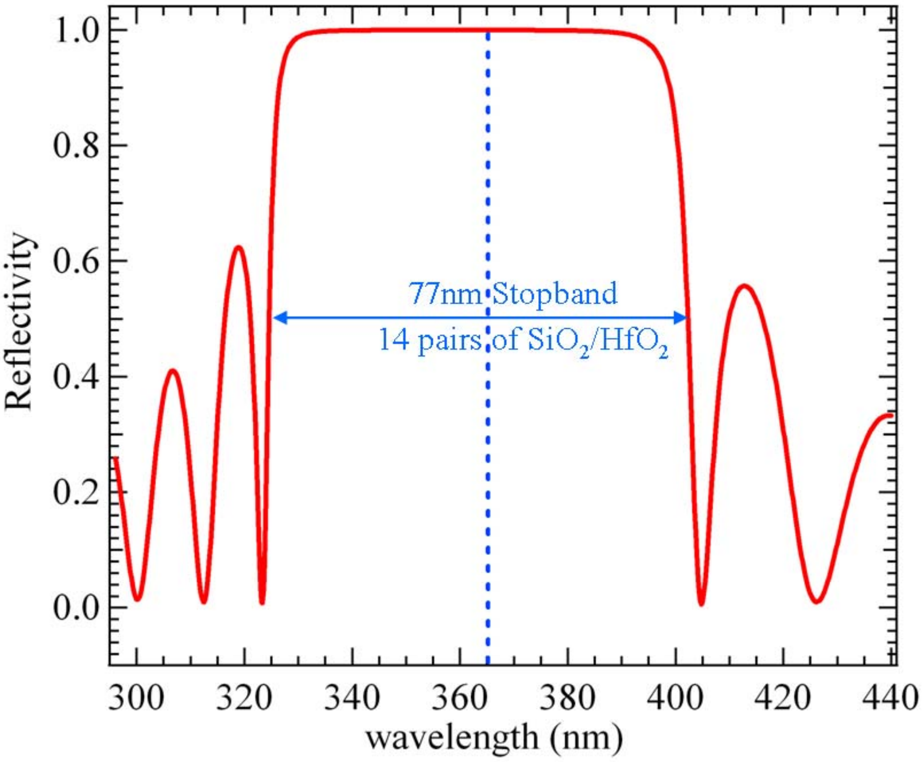

FIG. 3.9. Reflectivity spectra of a 14-pair SiO_2/HfO_2 DBR, calculated using Transfer Matrix simulations.

We simulate the reflectivity spectrum for few (*N=8*) periods-pairs of SiO_2/HfO_2 and then for twelve (*N=12*) and fourteen (*N=14*) pairs, as seen in figure 9. As expected from theory (see Eq. 3.7), reflectivity increases with the number of pairs.

This DBR simulation shows clearly that the dielectric Bragg mirrors are better than the monolithically grown ones [2], providing larger stopbands and high reflectivities of more than 99%, preventing us also from growing big numbers of stacks.

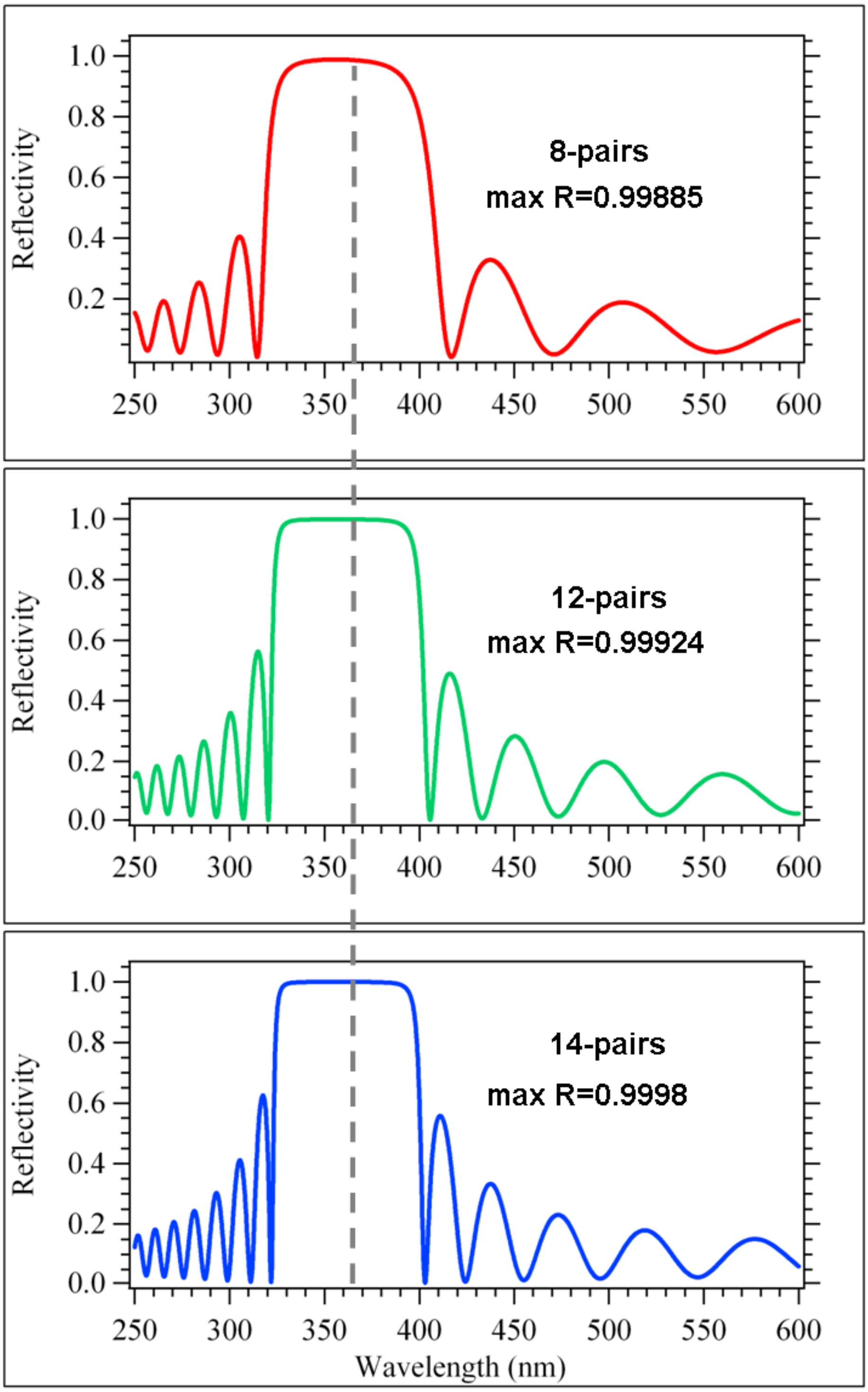

FIG. 3.10. Reflectivity spectra from SiO_2/HfO_2 DBRs with 8, 12 and 14 pairs respectively.

3.6 Microcavity Structure

We simulate a microcavity structure, consisting of fourteen (14) SiO_2/HfO_2 pairs for its first dielectric mirror on quartz substrate. A 207nm thick bulk Gallium Nitride was used as an active layer. The top DBR is a twelve (12) pair stack, made of SiO_2/HfO_2. The whole structure is represented by a matrix similar to that of Eq. 3.4.

From Eq. 3.6 it is obvious that the refractive indexes play the most important role in the transfer matrix simulations of DBRs. The active GaN layer is incorporated in the microcavity matrix as an intermediate stack of corresponding matrices, with elemnts the modulated refractive index of GaN. This layer has its own real and complex parts of refractive index (see Fig. 3.6). The peak modulation of the refractive index is directly related to the excitonic absorption of the active layer. This modulation introduces in the Transfer Matrix the GaN oscillator strength (see Eq. 1.8-1.12), defining the coupling constant *V*, as described by the Eq. 2.6. It also introduces all possible broadenings of exciton linewidth, attributed to several reasons such us temperature, LO–phonon scattering etc. Thus, with this method we can find out whether our microcavity will be strongly or weakly coupled.

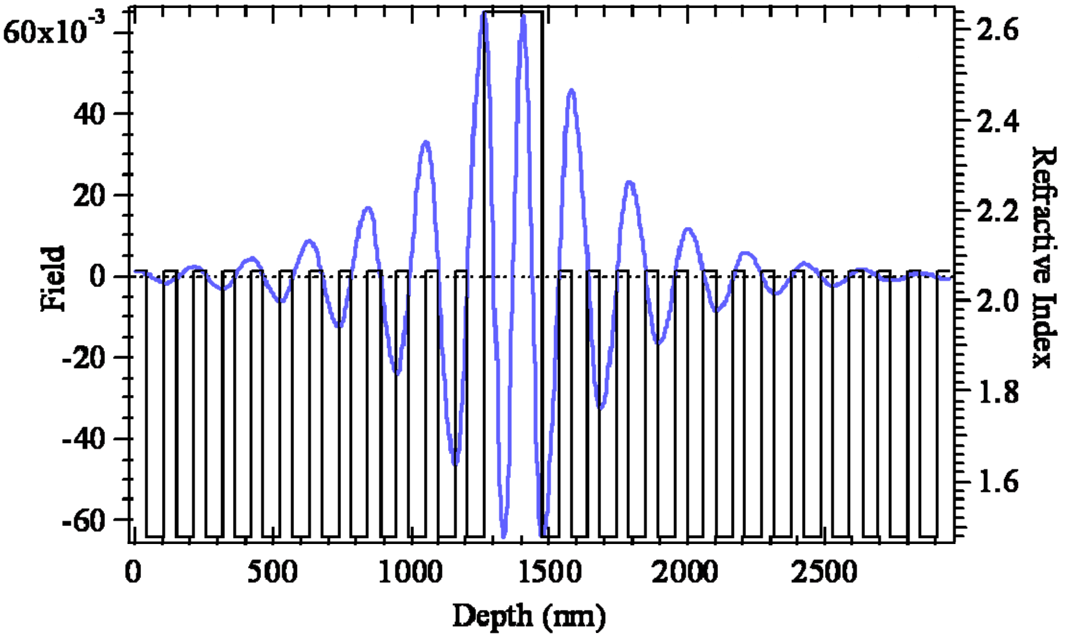

FIG. 3.11. Calculated photon field distribution for the designed all dielectric GaN microcavitiy, with its refractive index profile.

The microcavity we simulate is a 3λ/2 cavity according to the following calculation.

$$\frac{3}{2}\lambda_{cavity} = \frac{3}{2}\frac{\lambda_{exc}}{n_{cav}} = \frac{3}{2}\left(\frac{362nm}{2.62}\right) = 207nm.$$

This is in aggrement with the 3λ/2 modulation of the electric field in the active layer in Figure 3.11. In this figure at every phase difference of $\delta\varphi=\pi/4$ the field passes from one dielectric layer to the other validating that BDRs are quarter-wave multilayered structures. The designed thickness of the active medium is also very close to the 210nm thickness of bulk GaN used by Christopoulos et al. [22], who have shown optically pumped polariton lasing, in a semi-dielectric GaN microcavity.

The optimization of the thickness not only of the dielectrics but also of the active layer gives us a Rabi splitting of 93meV. When, thus, the microcavity is strongly coupled, the modulation of the electric field in the centre of the cavity within the active layer maximizes, as depicted in Figure 3.11.

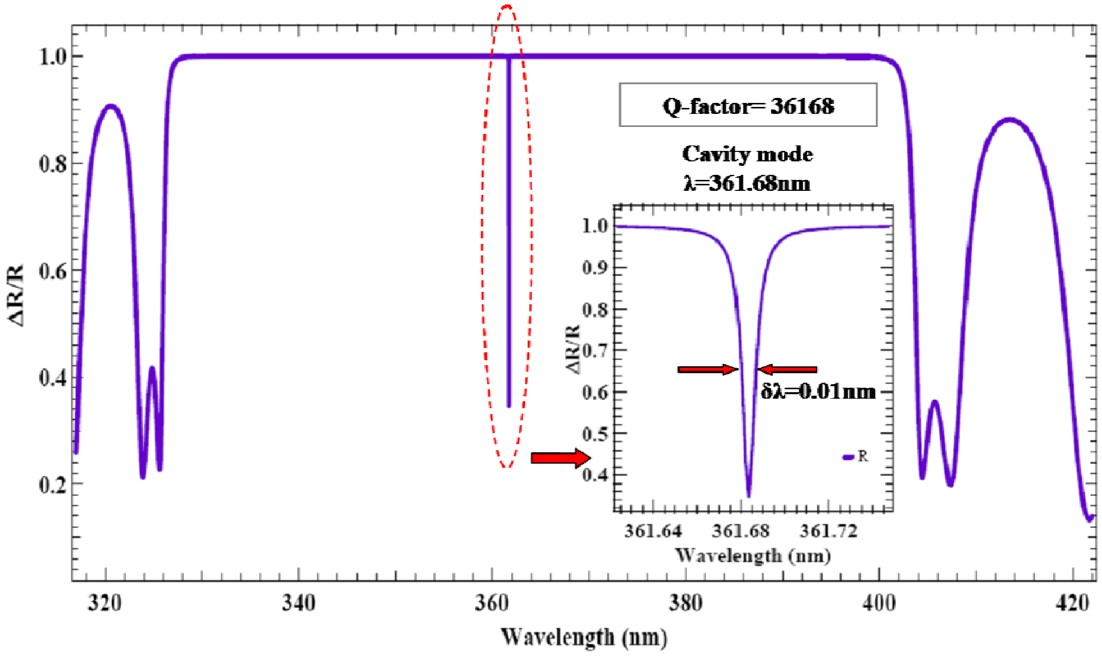

FIG. 3.12. Calculated reflectivity spectra of the designed microczvity. The high Q factor is its main characteristic.

We also simulate a microcavity detuning, assuming a linear variation of angle θ of incidence. We record as series of reflectivity spectra, which we intentionally space them in the y-axis, in order to show in Figure 3.13 the resulting characteristic anticrossing of the upper and lower polartion branches.

Before we evaluate this 93meV of splitting we check also the quality of the microcavtiy. It is defined by the quality factor-Q of the corresponding empty optical cavity, as described in Eq. 2.19. For this reason, we reform a bit our simulation model and instead of an absorbing medium with an excitonic modulation of refractive index, we use a constant value of it (n=2.3) while zeroing its complex part, related to the absorption. Practically, we replace the optically active medium with a simple non-absorbing spacer. In order to preserve the same optical thickness and the 3λ/2 cavity, we increased the actual thickness of the spacer according to the calculation $(3/2)(362nm/2.3) = 236nm$. The resultant cavity mode is a very sharp and intense in the reflectivity spectrum. So sharp (0.02nm linewidth), that we can hardly measure it with the resolution of a modern spectrometer. The resonance is at 361.68nm and according to the equation $Q=\lambda/\delta\lambda$ we get a quality factor of $Q\approx 36168$, which is a value quiet high compared to these from literature.

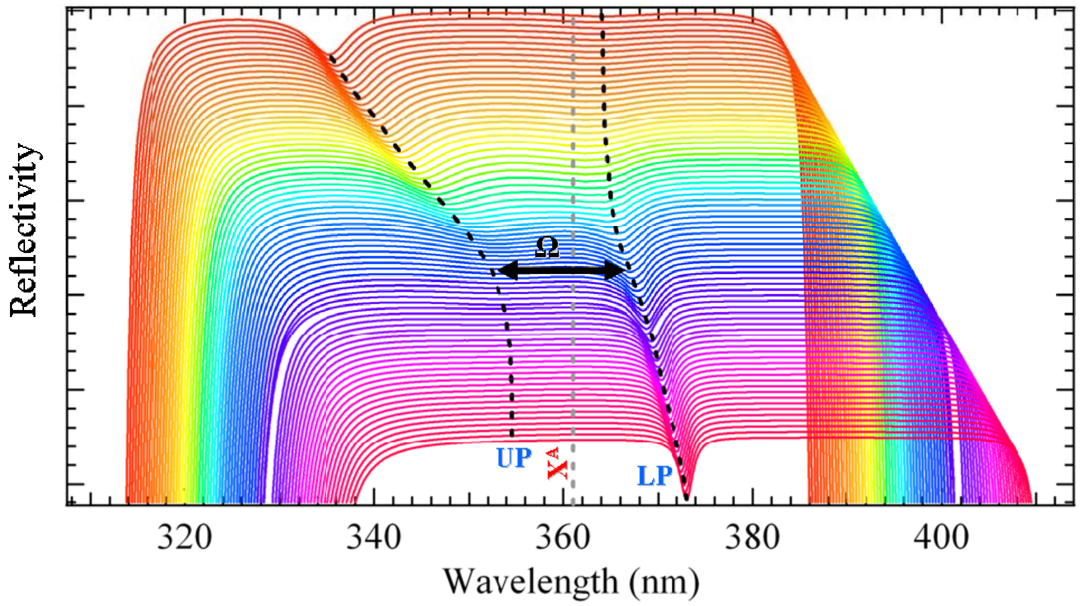

FIG. 3.13. Intentionally spaced calculated reflectivity spectras of the designed microcavity, showing the desired strong coupling of exciton and photon and the famous anticrossing of the polariton branches.

This very high value of the Q-factor is attributed to the fact that no losses of the dielectric layers are taken into account, resulting in a strong confinement of the cavity mode. We also do not take into account any broadenings coming out of surface roughness of the dielectrics and the nitride layer.

3.7 PEC process scheme

The fabrication of an all-dielectric GaN microcavity, as already discussed in the beginning of this Chapter, is not an easy task, since we require optical flatness of each layer of the microcavity and especially for the active medium. We propose a novel fabrication approach based on the removal of a sacrificial InGaN layer, using a photoelectrochemical (PEC) wet etching technique.

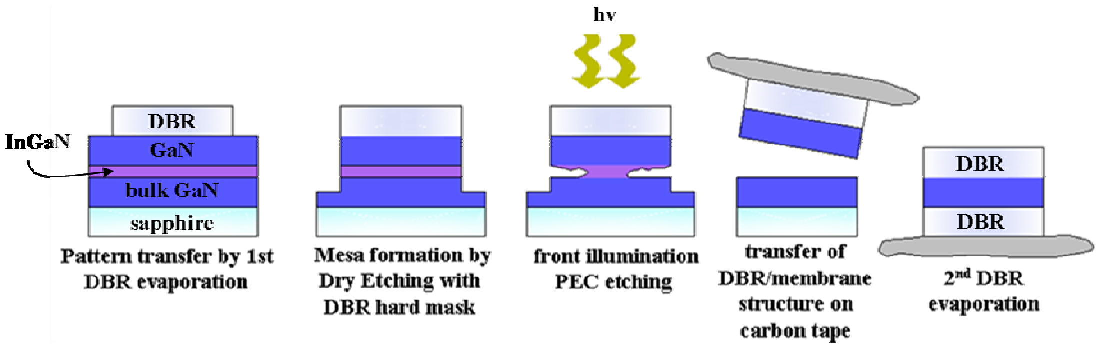

FIG. 3.14. schematic of the proposed process method for the fabrication of an all-dielectric microcavity.

As depicted in Figure 3.14, the GaN active medium of the microcavity is grown above a thinner InGaN film, on a c-plane GaN template. Using a lithographic technique, we evaporate squares of dielectric Bragg mirrors, which play the dual role of the first mirror of the microcavity and that of the hard mask for mesa formation after a dry etching technique. This way, the InGaN facets may be exposed to alkali or acid solvents for their lateral photoelectrochemical etching, exciting it with a photon energy above its bandgap and below GaN bandgap. The mirror must be designed that way so the excitation photon may pass through it and excite the sacrificial layer. After the complete removal of it, a free standing pair of DBR/GaN membrane is yielded, which can be easily manipulated with a common carbon tape. After, turning this structure up side down we evaporate the second dielectric Bragg mirror, creating an all-dielectric GaN microcavity. The main advantage of this method is the fact that it requires less processing steps in order to detach the GaN membrane from its substrate and incorporate it within an all dielectric cavity.

References

[1] J. Carlin and M. Ilegems, “High-quality AlInN for high index contrast Bragg mirrors lattice matched to GaN,” *Applied Physics Letters*, vol. 83, no. 4, p. 668, 2003.

[2] J. Dorsaz, J. Carlin, S. Gradecak, and M. Ilegems, “Progress in AlInN–GaN Bragg reflectors: Application to a microcavity light emitting diode,” *Journal of Applied Physics*, vol. 97, no. 8, p. 084505, 2005.

[3] R. Butté et al., “Room-temperature polariton luminescence from a bulk GaN microcavity,” *Physical Review B*, vol. 73, no. 3, p. 033315, Jan. 2006.

[4] G. Christmann, R. Butté, E. Feltin, J. Carlin, and N. Grandjean, “Impact of inhomogeneous excitonic broadening on the strong exciton-photon coupling in quantum well nitride microcavities,” *Physical Review B*, vol. 73, no. 15, p. 153305, Apr. 2006.

[5] F. Réveret et al., “Strong light-matter coupling in bulk GaN-microcavities with double dielectric mirrors fabricated by two different methods,” *Journal of Applied Physics*, vol. 108, no. 4, p. 043524, 2010.

[6] D. Simeonov et al., “High quality nitride based microdisks obtained via selective wet etching of AlInN sacrificial layers,” *Applied Physics Letters*, vol. 92, no. 17, p. 171102, 2008.

[7] K. Bejtka et al., “Strong light-matter coupling in ultrathin double dielectric mirror GaN microcavities,” *Applied Physics Letters*, vol. 92, no. 24, p. 241105, 2008.

[8] F. Rizzi et al., “(In,Ga)N⁄GaN microcavities with double dielectric mirrors fabricated by selective removal of an (Al,In)N sacrificial layer,” *Applied Physics Letters*, vol. 90, no. 11, p. 111112, 2007.

[9] C. Youtsey, I. Adesida, L. T. Romano, and G. Bulman, “Smooth n-type GaN surfaces by photoenhanced wet etching,” *Applied Physics Letters*, vol. 72, no. 5, p. 560, 1998.

[10] J. F. Muth et al., “Absorption coefficient, energy gap, exciton binding energy, and recombination lifetime of GaN obtained from transmission measurements,” *Applied Physics Letters*, vol. 71, no. 18, p. 2572, 1997.

[11] A. J. Fischer, W. Shan, J. J. Song, Y. C. Chang, R. Horning, and B. Goldenberg, “Temperature-dependent absorption measurements of excitons in GaN epilayers,” *Applied Physics Letters*, vol. 71, no. 14, p. 1981, 1997.

[12] W. Shan et al., “Binding energy for the intrinsic excitons in wurtzite GaN,” *Physical Review B*, vol. 54, no. 23, p. 16369, Dec. 1996.

[13] A. K. Viswanath, J. I. Lee, D. Kim, C. R. Lee, and J. Y. Leem, “Exciton-phonon interactions, exciton binding energy, and their importance in the realization of room-temperature semiconductor lasers based on GaN,” *Physical Review B*, vol. 58, no. 24, p. 16333, Dec. 1998.

[14] A. Hoffmann, “Dynamics of excited states in GaN,” *Materials Science and Engineering B*, vol. 43, no. 1, pp. 185-191, Jan. 1997.

[15] D. S. Chemla and D. A. B. Miller, “Room-temperature excitonic nonlinear-optical effects in semiconductor quantum-well structures,” *Journal of the Optical Society of America B*, vol. 2, no. 7, pp. 1155-1173, Jul. 1985.

[16] V. Voliotis, R. Grousson, P. Lavallard, and R. Planel, “Binding energies and oscillator strengths of excitons in thin GaAs/Ga_{0.7}Al_{0.3}As quantum wells,” *Physical Review B*, vol. 52, no. 15, p. 10725, Oct. 1995.

[17] J. C. Maan, G. Belle, A. Fasolino, M. Altarelli, and K. Ploog, “Magneto-optical determination of exciton binding energy in GaAs-Ga_{1-x}Al_{x}As quantum

wells," *Physical Review B*, vol. 30, no. 4, p. 2253, 1984.
[18] A. Kavokin and B. Gil, "GaN microcavities: Giant Rabi splitting and optical anisotropy," *Applied Physics Letters*, vol. 72, no. 22, p. 2880, 1998.
[19] T. Tawara, H. Gotoh, T. Akasaka, N. Kobayashi, and T. Saitoh, "Cavity Polaritons in InGaN Microcavities at Room Temperature," *Physical Review Letters*, vol. 92, no. 25, p. 256402, Jun. 2004.
[20] M. Saba et al., "High-temperature ultrafast polariton parametric amplification in semiconductor microcavities," *Nature*, vol. 414, no. 6865, pp. 731-735, Dec. 2001.
[21] P. Yeh, *Optical Waves in Layered Media*, 2nd ed. Wiley-Interscience, 2005.
[22] S. Christopoulos et al., "Room-Temperature Polariton Lasing in Semiconductor Microcavities," *Physical Review Letters*, vol. 98, no. 12, p. 126405, Mar. 2007.

Chapter 4: Bandgap Selective Photoelectrochemical Etching of Nitrides

4.1. Photoelctrochemical (PEC) etching vs Dry Etching of Nitrides

As mentioned in the previous Chapter the photoelectrochemical (PEC) etching of nitrides is an essential tool for the proposed process scheme towards fabrication of all-dielectric GaN microcavities. Compared to other etching techniques, it is the only available promising processing method, able to achieve lateral etching and yield GaN membranes, as desired in the all-dielectric GaN microcavities technology.

Most processing of the III-nitrides is conducted by dry-plasma etching because of the absence, until today, of a wet etching method, due to the strong chemical stability of the Ga-polar GaN and its high resistance to all kinds of solutions at room temperature. This behaviour is attributed to the fact that group-III nitrides have high bond energies compared to conventional III-V semiconductors. The bond energies are 7.7eV/atom for InN, 8.9eV/atom for GaN, and 11.5eV/atom for AlN compared to 6.5eV/atom for GaAs. These high bond strengths and wide bandgaps make nitrides essentially chemically inert and highly resistant to bases and acids at room temperature [1], [2]. However, this technique has two main disadvantages: (i) creation of ion-induced damages and (ii) difficulty to obtain smooth sidewall etches, required in many optoelectronic devices [3], like nitrides microcavities. On the other hand, modern technology of photoelectrochemical (PEC) wet etching of nitrides [2-8], which has played an important role in fabricating novel electronic [9], optoelectronic [10] devices and MEMS [11] etc, has not been optimized up to the point of yielding ultra thin and ultra smooth nitride membranes, characteristics which are key elements for exciton-photon strong coupling.

In this thesis, we develop this method by exploiting PEC's bandgap selective nature, showing a significant etching rate increase on resonance with the exciton of GaN. Nobody had so far had explored any photocurrent and etching rate dependence with the excitation wavelength. This discovery helps us to show a truly selective PEC etching, able to self stop when the etching front reaches another nitride layer with a greater bandgap. Using this newly discovered advantage of PEC etching, we manage to fabricate ultra smooth and thin GaN membranes, with their exciton robustness sustained. These membranes are used in the proposed processing scheme, as illustrated in Chapter 3, for all-dielectric GaN microcavity fabrication.

4.2 The Semiconductor-Electrolyte System in Equilibrium

When a semiconductor is immersed in an electrolyte's solution with ionic species an interface potential difference, called *galvanic potential*, arises as a result of the transfer of charges across the semiconductor/electrolyte boundary [12], [13]. According to Gerischer [14], in analogy with semiconductor physics, the oxidised and reduced species of the electrolyte may be linked with a conduction band (i.e. an unoccupied electron state) and a valence band (i.e. an occupied electron state), respectively. A term similar to the Fermi level E_F of a semiconductor can be defined for a redox couple also, abbreviated as $E_{F,redox}$. If the redox potential of the solution and the semiconductor's Fermi level do not lie at the same energy, a movement of charge between the semiconductor and the solution is required in order to equilibrate the two phases. This charge transfer shall continue till the Fermi level positions in the semiconductor equals $E_{F,redox}$, ($E_{F(semiconductor)} = E_{F, redox}$), (4.1) as shown in Figure 4.1.

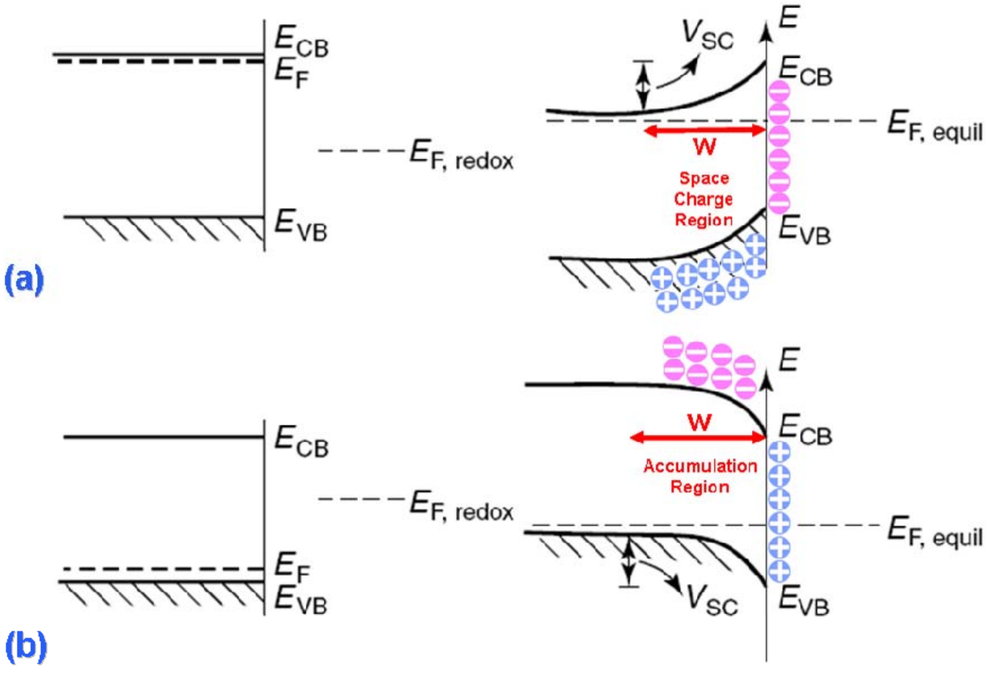

FIG. 4.1. The semiconductor/electrolyte interface before (left) and after (right) equilibration shown a) for an n-type semiconductor, (b) for a p-type semiconductor.

When equilibrium is established a “built-in” voltage, $V_{SC} = -\left(eN_D / 2\varepsilon_1\right)W$, (4.2), develops within the semiconductor phase, which is attributed to an excess charge extended into the electrode for a significant distance $W = \sqrt{\varepsilon_1 kT / 4\pi e^2 N_D}$ (4.3), the Debye Length , where N_D is the concentration of majority carriers and ε_1 is the static dielectric constant of the semiconductor. This region is referred as the *Space Charge Region* (SCR) [15].

For an *n*-type semiconductor electrode at open circuit, the Fermi level is typically higher than the redox potential of the electrolyte, and hence electrons will be transferred from the electrode into the solution. Therefore, there is a positive charge associated with the space charge region, and this is reflected in an upward bending eV_{SC} of the band edges (see Fig. 4.1a). Since the majority charge carrier of the semiconductor has been removed from this region, this region is also referred to as a *depletion* layer.

For a *p*-type semiconductor, the Fermi layer is generally lower than the redox potential, and hence electrons must transfer from the solution to the electrode to attain equilibrium. This generates a negative charge in the space charge region, which causes a downward bending eV_{SC} in the band edges (see Fig. 4.1b). Since the holes in the space charge region are removed by this process, this region is again a depletion layer.

4.3 Charge Transfer Reactions in a Semiconductor/Electrolyte Electrode

The charge transfer reactions in a semiconductor/electrolyte electrode are important to understand, in order to see how the PEC etching of nitrides behaves and the microscopic parameters like charge transfer reactions may affect PEC’s result in terms of quality of etched surfaces, anisotropy of the etched profiles and bandgap selectivity. These reactions can be modified by changing either:

(i) the position of E_c and E_v band edges by applying a bias (*V*), or

(ii) the position of E_c and E_v by light induced carrier generation [14].

<u>*A. The effect of bias*</u>: When we apply a negative bias (*V<0*) to the semiconductor electrode (reverse-anodic polarisation), an increase $e(V_{SC}^{REV} - V_{SC})$ (4.4) in upward bending of conduction and valence band would take place for an n-type semiconductor, as shown in Figure 6b.

Contrary, a positive bias (*V>0,forward*-cathodic polarisation) would create a downward band bending [15].

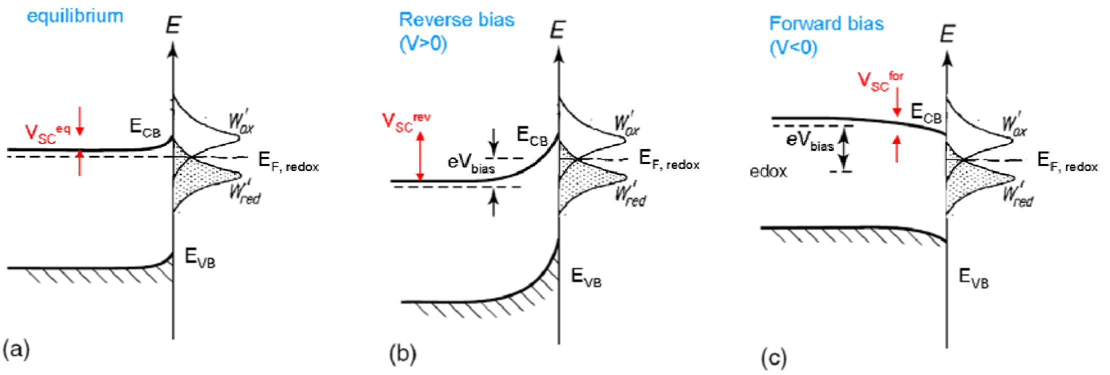

FIG. 4.2. Three situations for an n-type semiconductor/electrolyte interface a) at equilibrium, b) under reverse bias and c) under forward bias.

Most important for our photochemical technique is the reverse bias of Gallium nitride, since this upward band bending may act as a trap for the photogenerated holes, which play a significant role in the etching process of GaN.

<u>*B. The Photoeffect*</u>: When a semiconductor, immersed in an electrolyte, is illuminated with a photon energy above its bandgap, the density of energy dissipated on absorption of the light, as a function of the coordinate x, is described by the expression

$$g(x) = I_0 \alpha e^{-\alpha x}, \qquad (4.5)$$

where a is the coefficient of light absorption by the semiconductor and

$$I_0 = \int_0^\infty g(x)dx, \quad (4.6)$$

is the intensity of the light flux falling on the semiconductor surface. The function $g(x)$ is illustrated by the solid red curve in Fig. 4.3

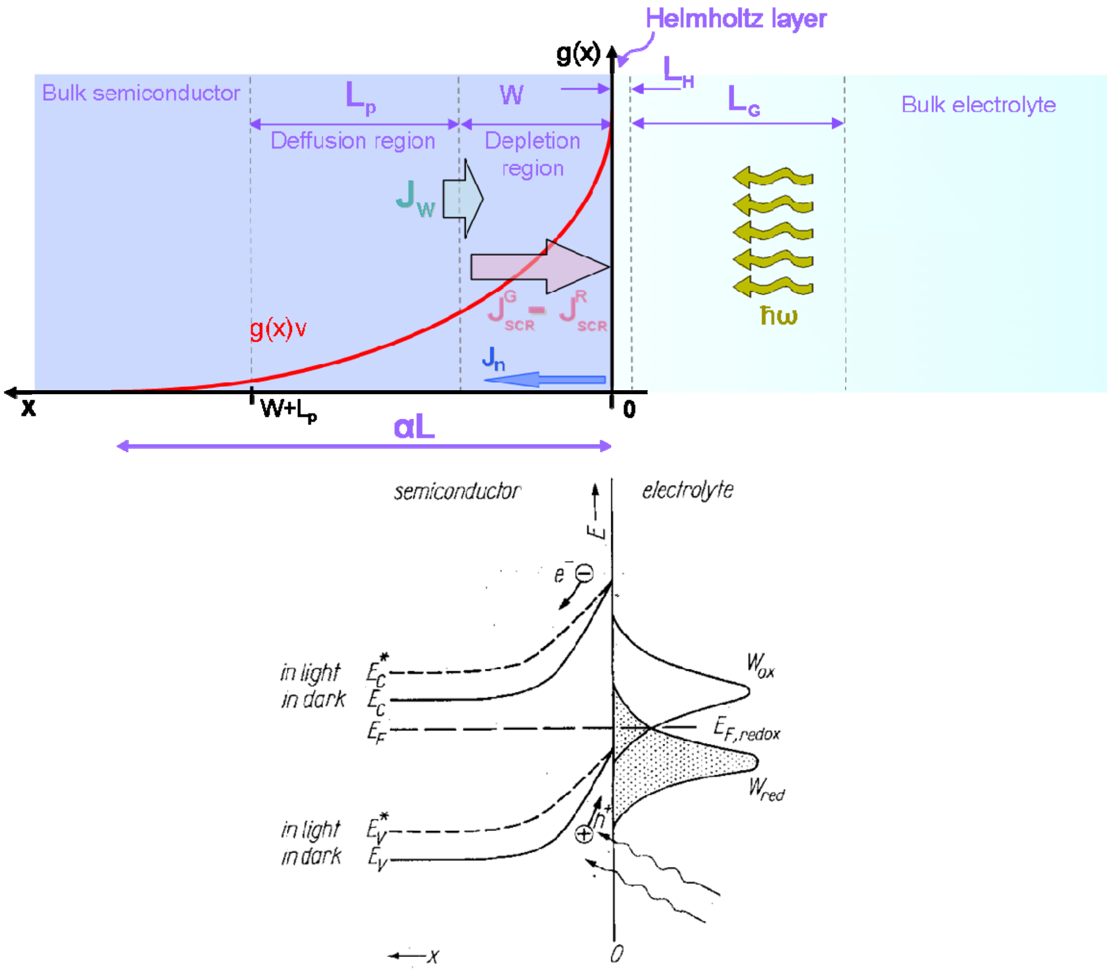

FIG.4.3. Diagram of light absorption in an n-type semiconductor and origin of the photo-effect in the depletion layer. [A way to describe the semiconductor/electrolyte electrode is the formation: a) of a *depletion layer* (*space charge region*) and a *diffusion region of minority carriers* within the semiconductor mass, b) of a dense ionic double *Helmholtz layer* very close to the semi/electrolyte interface and c) of a *Gouy-diffuse layer* in the *bulk* of the semiconductor [16]].

On absorption of photons in the semiconductor, electron-hole pairs are generated and in the simplest case, when quantum efficiency equals unity, the generation function coincides with $g(x)$. The illumination leads to photogenerated minority excess carriers (holes for n-type semiconductor) and the quasi-Fermi levels are disturbed [14], as depicted in Figure 4.3. To this charge transfer reaction of minority excess carriers is attributed the band bending change at the interface, as shown in Figure 7(b), which changes the charge distribution within the space charge layer and hence the electrode potential. The corresponding field creates a potential well for the holes which are swept to the surface and the electrons are driven to the bulk of the semiconductor.

The extent of collection of nonequilibrium minority carriers from the region beyond the depletion layer is dictated by their diffusion process [15-17]. This characteristic diffusion length L_p defines the region within which electron-hole pair generation is fully effective. Pairs generated at depths $1/a$ longer than the sum of Debye length W and the diffusion length L_p simply recombine. Thus, the effective quantum yield for a given interface will depend on the relative magnitudes of $(W + L_p)$ and the light penetration depth $1/a$ [15], [18].

The current density J across a semiconductor/electrolyte interface according to the Reichman model [17], is the sum of electron current densitiy J_n, the hole current density at the edge of space charge region J_w, the hole generation and the recombination current densities J_{SCR}^{G} and J_{SCR}^{R} respectively.

$$J = J_n + \left(J_w + J_{SCR}^{G} - J_{SCR}^{R}\right), \quad (4.7)$$

The hole current density at the edge of space charge region J_w is obtained by the following equation:

$$J_w = -J_0\left(\frac{p_w}{p_0} - 1\right) + \frac{qI_0 a L_p \exp(-aW)}{1 + aL_p}, \qquad (4.8)$$

where q is the elementary charge, p_w is the hole concentration derived from diffusion region, p_0 is the equilibrium hole concentration, I_0 is the monochromatic photon flux incident on the semiconductor, and α is the absorption coefficient.

On the other hand, the current density in the space charge region generated by photon absorption is: $J_{SCR}^{G} = qI_0(1 - \exp(-aW))$, (4.9), however there is an effect of recombination whose corresponding recombination current density in the space charge region is

$$J_{SCR}^{R} = \frac{\pi kTn_iW \exp(-qV/2kT)}{4\tau(V - V_{fb})} \sqrt{\left(\frac{p_s}{p_{s0}}\right)}, \quad (4.10)$$

where n_i is the intrinsic carrier density, V is the applied bias, V_{fb} is the flatband potential and p_s, p_{s0} are the hole concentrations in excited and equilibrium state respectively.

For majority carrier in *n*-type semiconductor, the electron current density is given by the equation:

$$J_n = -I_n^0[\exp(-qV/kT) - 1], \quad (4.11)$$

where I_n^0 is the electron current density in equilibrium.

It is easy to understand that the photocurrent is affected by many parameters. For a given light absorption coefficient, depending on the semiconductor, its doping defines the width of the depletion region and thus the relative difference between the light penetration depth and the sum of Debye length W and the diffusion length L_p, which sets the recombination region. This way J_w is affected. For example, at constant potential, a highly doped semiconductor having a narrower depletion layer, yields smaller photocurrent. An increase of reverse bias, also, decreases the recombination current, while it enhances the confinement of minority carriers on the semiconductor/electrolyte interface. In general, we can tune the behavior of a PEC etching experiment by modifying the charge transfers via modulation of material parameters like the absorption coefficient and the doping, as such as the applied voltage and the illumination power density.

4.4 The Photoelectrochemical Etching of GaN.

The photoelectrochamical (PEC) wet atching of c-plane GaN was first shown by Minsky et al. [4], who had demonstrated rapid etching of n-type GaN in aqueous KOH solution. An etching process similar to that of GaAs was suggested. According to this suggestion the anode (GaN film) and the cathode (platinum electrode) are dipped in the electrolyte (usually KOH) solution.

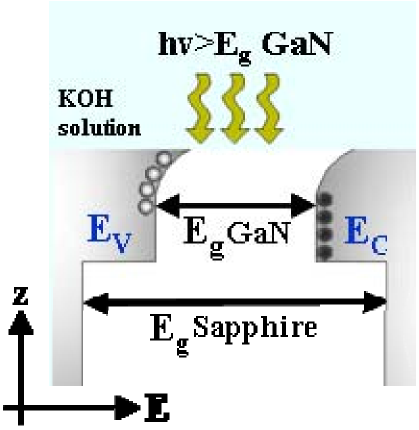

FIG. 4.4. Schematic of the band diagram of the electrolyte/GaN on c-plane sapphire system during PEC etching.

The electrolyte/GaN interface forms a Schottky contact (see Fig. 4.4) and has the characteristic upward band bending presented in the previous paragraph. When the sample is illuminated with photon energies above GaN bandgap at 300 K, electron-hole pairs are generated in the semiconductor, producing measurable photocurrent. The application of a reverse dc bias to the semiconductor further confines the holes at the electrolyte/semiconductor interface, where they participate in the etching process consisting of the Ga oxidation and its oxide dissolution, as described from the following chemical equations:

Ga oxidation:

$$2GaN + 6h^{+} + 6OH^{-} \rightarrow Ga_2O_3 + 3H_2O + N_2 \uparrow \qquad \text{(CE.4.1)}$$

oxide dissolution:

$$Ga_2O_3 + 6OH^- \rightarrow 2GaO_3^{-3} + 3H_2O \qquad (CE.4.2)$$

According to Faraday’s law of electrolysis, the current flow between the sample (anode) and Pt (cathode) is proportional to the reaction rate at the semiconductor/electrolyte interface, and therefore provides an instantaneous measure of the etch rate of the semiconductor [3]. The chemical equations above were derived from the integral of photocurrent versus time.

4.5 Experimental Setup & Photoelectrochamistry of GaN

In order to optimize the PEC etching method in the fabrication process of the so-called all-dielectric GaN based microcavities we investigate fundamental properties and behaviour of the simple vertical PEC etching effect. Thus, we designed a series of experiments and samples dedicated to this work. The samples used for vertical PEC etching are the following:

Sample 1: Structure from top to bottom:

- 10nm AlAs, undoped
- 30nm GaAs, undoped
- 10nm AlAs, undoped
- GaAs substrate, undoped

Sample 2: An unintentionaly doped 3μm c-plane GaN template

Sample 3: Structure from top to bottom:

- 300nm $Al_{0.32}Ga_{0.68}N$, undoped
- 50nm Si-doped GaN, undoped
- 1μm c-plane GaN template, unintentionaly doped

Sample 4: Structure from top to bottom:

- 50nm $In_{0.1}Ga_{0.9}N$, undoped
- 3μm c-plane GaN template, unintentionaly doped

Sample 5: Structure from top to bottom:

- 350nm GaN, undoped
- 100nm $Al_{0.2}Ga_{0.8}N$, undoped
- 3μm c-plane GaN template, undoped
- GaAs substrate, unintentionaly doped

All samples are lithographically patterned into a grid of 40x40 μm^2 squares with 100 nm thick Ti layer as a mask, whose period is depicted in Figure 4.5a. This was done in order to create dense micrometer scale patterns able to show the contrast between the etched and non etched surfaces of the samples. Additionally, the resulting from etching sidewall of the etch front may be more discernible. Figure 4.5b shows a pair of exposed to electrolyte and light semiconductor squares, defined by a Ti grid, after a PEC etching experiment. The semiconductor is not biased via this Ti-grid. An Indium (In) Ohmic contact is formed on the edge of every sample for the application of reverse voltage, usually of the value of 4Volts (see also the PEC cell in Fig. 4.7).

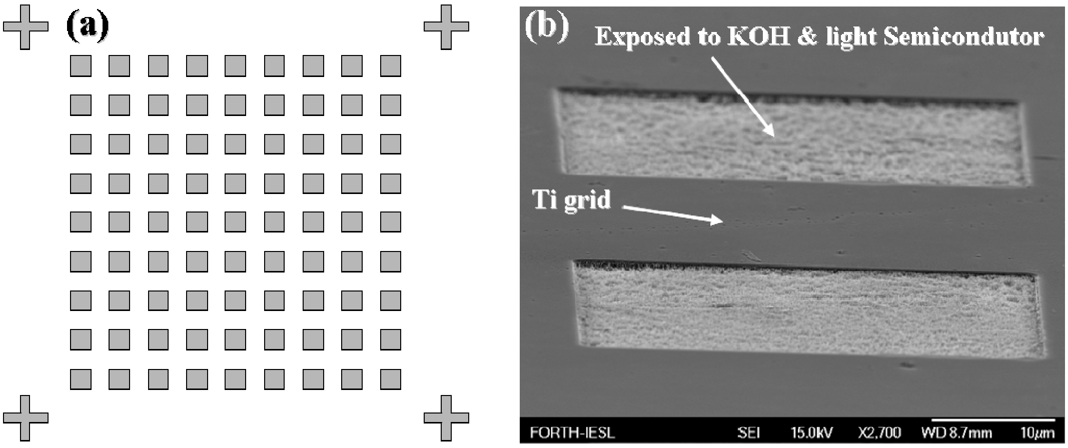

FIG.4.5. a) Pattern of the mask used for the formation of 4x40 μm^2 squares. Dark areas correspond to Chromium. b) SEM image of exposed to electrolyte and photons pair of semiconductor squares, derived from the mask depicted on the side.

Most photochemical etching experiments of our nitrides samples are carried out in an electrochemical cell at room temperature using (in most cases) stirred 0.01M KOH solution. Although a number of different electrolyte solutions such as KOH, HCl, H_3PO_4 have been used in the literature for PEC, we have chosen KOH because previous results show that it yields smoother etched surfaces and sharper vertical sidewalls [7], [19].

The experimental setup of the PEC etching of nitrides is very simple. Its schematic is shown in Figure 4.6. The cell is a Teflon vial on which the nitride semiconductor is attached by a specially designed clamp. The semiconductor closes a hole on the Teflon cube with an intermediate cone shaped O-ring. Opposite to the semiconductor, there is a quartz window which allows its excitation, even with wavelengths in the ultraviolet spectrum. A wire made of platinum (Pt) is suspended from the top surface, into the interior of the cell. A bigger hole is done in order to have access to it for filling it with the proper electrolyte and for withdrawing possible N_2 bubbles formed on the etched surface with a common syringe. Finally, a specially designed hole is used for the drainage of the electrolyte after PEC etching.

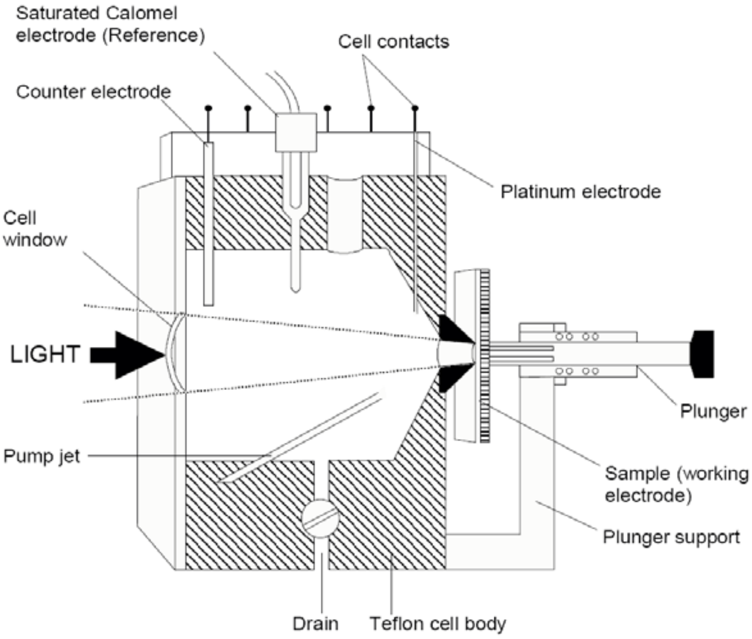

FIG.4.6. Schematic of the Teflon made cell for PEC etching experiments. The counter and saturated calomel electrodes are not used in our case.

The corresponding electrochemical circuit is also very simple. The semiconductor is biased using a tunable voltage source in series with an ammeter. We setup a photocurrent vs time monitoring system, using a standard GPIB connection between a computer and the ammeter, since we are interested in measuring the variations of photocurrent during the evolution of the PEC etching. That way we are able to investigate oxide formation and transitions of the etching front when a different bandgap semiconductor is reached.

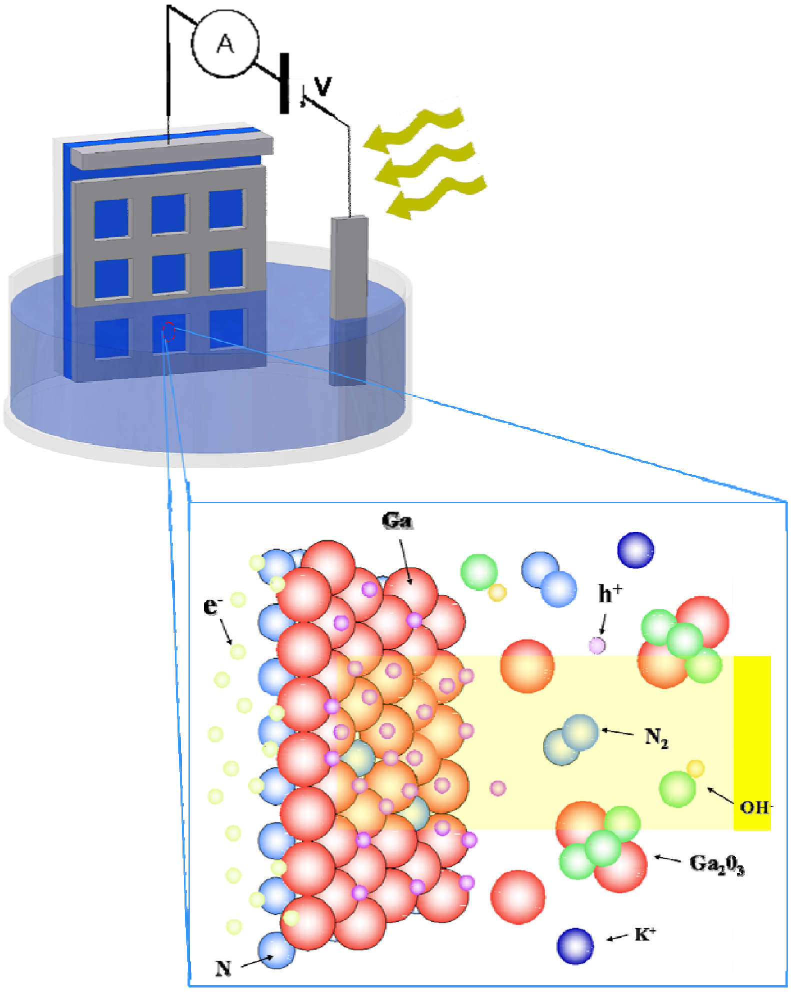

FIG.4.7. Schematic of experimental setup of the photoelectrochemical etching of nitrides. The samples are patterned with a standard lithographic process and a Ti mask was fabricated to yield measurable etching profiles. An Ohmic contact is applied on the edge of the sample for the biasing of the samples. If it is immersed in the solution, a short circuit is forming, stopping the PEC effect.

We test this interface and photo-oxidation monitoring tool by using a GaAs/AlAs structure (sample 1), which does not have any resistance to etching agents. Figure 4.8 clearly illustrates these interfaces existing in the sample structure, corresponding to the change of the photocurrent constant level. This is a strong proof that the monitoring steup is reliable. Thus, we can use it in PEC etching experiments for the rest of the nitrides samples.

.

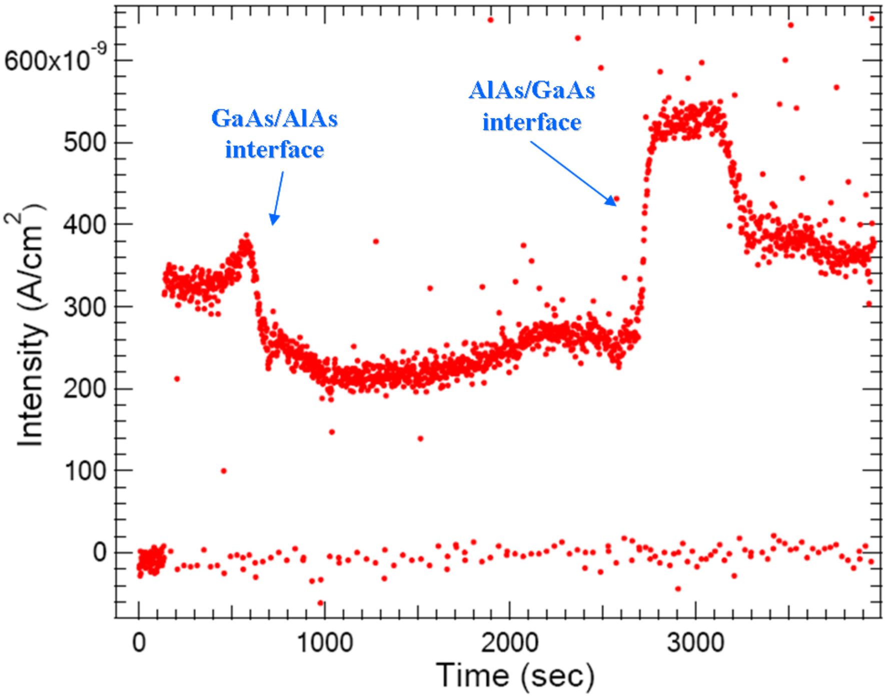

FIG. 4.8. Plot of the photocurrent density time evolution during the PEC etching of GaAs/AlAs interfaces in sample 1.

With this monitoring apparatus we can also acquire I-V measurements from the semiconductor/electrolyte system when being illuminated above bandgap or not. Figure 4.9 illustrates the Schottky like behavior of the GaN/electrolyte system. Negative bias corresponds to forward bias of the contact and the positive to a reverse one

In the dark (curve (a)) diode characteristics are observed. At negative potentials (range I) a cathodic current mainly due to hydrogen evolution results from the reduction of water by conduction band electrons.

$2H_2O + 2e^- \rightarrow H_2 + 2OH^-$ (CE.4.3)

The flat-band potential (the case in which theoretically the boundaries of the energy bands are not deformed by the electric field) is located in this range ($U_{fb} \approx$-

0.7V for undoped GaN), so that the electron concentration at the surface is high. At positive potentials the current is very low. Under illumination, electron–hole pairs are generated. In the potential range I the band bending is small and the electric field is not sufficiently strong to separate the electrons and holes; they recombine both in the bulk and at the surface and, consequently, no photocurrent is observed.

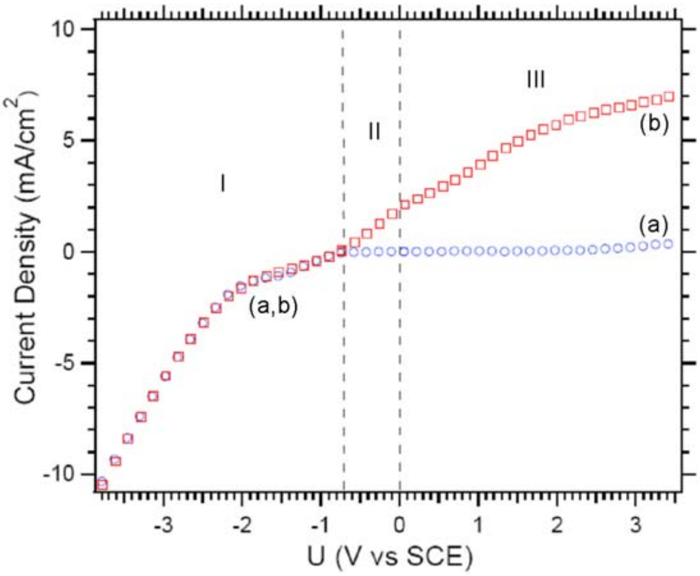

FIG. 4.9. Typical current density–potential plots for an n-type epitaxial GaN electrode: with a carrier concentration of 1.5×10^{17} cm^{-3} in 0.004M KOH solution: (a) in the dark and (b) under illumination. The corresponding energy band diagrams are also shown.

At more positive potential (stronger band bending in range II) a partial spatial separation of the charge carriers occurs. The holes driven to the surface can cause one of two electrochemical reactions: the oxidation of GaN as shown above, or the formation of oxygen,

$4OH^- + 4H^+ \rightarrow O_2 + 2H_2O$ (CE.4.4)

The electrons are detected as a photocurrent in the external circuit (at the counter electrode they give rise to a reduction reaction e.g. hydrogen evolution). It is clear that in this potential range not all the photogenerated holes contribute to the photocurrent. Since the band bending is moderate, the surface electron concentration is still rather high and some recombination occurs. As the potential is made more positive, the recombination rate of electrons and holes decreases due to increase in the electric field and the photocurrent increases. In range III the photocurrent begins to level off [20].

4.6 Excitation sources

In our experiments we use a series of the following excitation sources to provide photons above nitrides bandgap:

a) a cw He-Cd laser at 325nm , ?mW

b) a laser diode at 405nm, 22mW and

c) a tuneable Ti:Sapphire 150fs laser. The power extracted at each wavelength varies.

This femtosecond laser produces pulses from 680nm-2μm. These wavelegths correspond to energies below GaN bandgap. For this reason we frequency doubled the pulses using a BBO crystal (see Fig. 4.10). Thus, the available spectra range ofexcitation pulses during PEC etching is from 335nm to 380nm or 3.3–3.6 eV, (i.e., from 100meV below to 200 meV above the GaN bandgap at room temperature). Frequency doubling or Second Harmonic Generation (SHG) is the generation of light with a doubled frequency (half the wavelength). This BBO (β-barium borate) crystal has the necessary properties of being strongly birefringent, necessary to obtain phase matching. It has a specific crystal symmetry and it is transparent for and resistant against the high-intensity laser light.

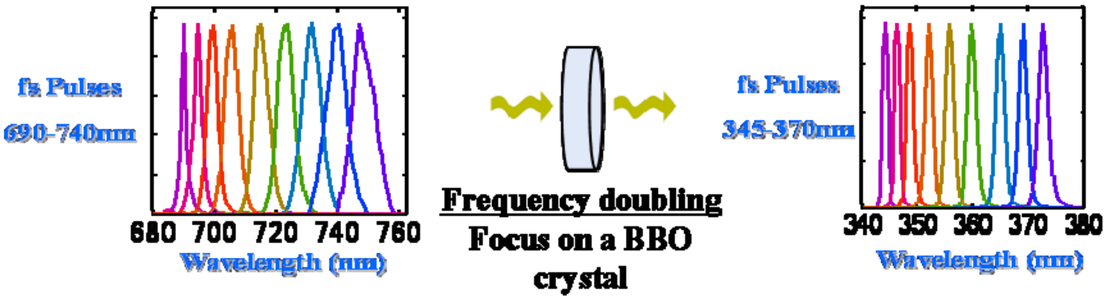

FIG. 4.10. Schematic of the frequency doubling method by focusing an ultrafast pulsed laser beam on a β-barium borate crystal, producing the dersired range of wavelengths.

4.7 Resonantly Enhanced PEC Etching of GaN

Previous PEC etching experimental works, by other groups, do not show any study on the dependence of nitrides PEC etching on the excitation energy, which would be a key element in expressing the bandgap selective nature of the method. Excitation sources typically used in those experiments are either He–Cd lasers at 325 nm [4] and [6] or filtered [10] and unfiltered [3] broadband excitation sources, such as xenon or Hg arc lamps, incapable of achieving high illumination densities. Contrary, the illumination with our UV pulses, having a spectral full width at half maximum of ~15meV and high intensity allows the careful study of the etching process dependence on the excitation energy.

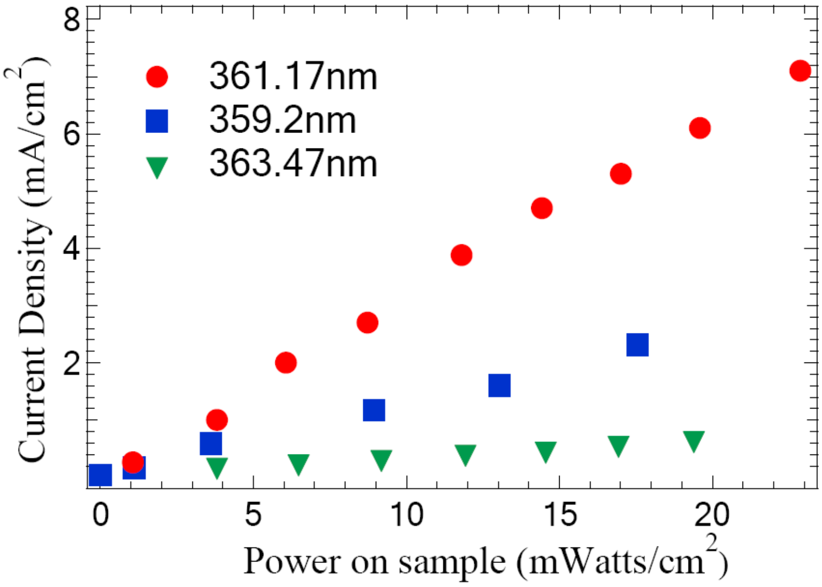

FIG. 4.11. Induced photocurrent vs excitation wavelength. Shows linear dependence of photocurrent on power density and sharp increase when exciting at 361.17 nm.

To study the dependence of the photogenerated carriers participating in the etching process on the excitation wavelength and power, we bias the GaN sample 2 at 4V (moderate band bending of region III in Fig. 4.9), while continuously stirring the 0.01M KOH solution. The induced photocurrent is recorded at different wavelengths with increasing power density. In Figure 11 the linear dependence of the measured photocurrent on the excitation density for selected wavelengths around GaN bandgap is clearly seen. Linear dependence of the photocurrent on illumination power density has been previously observed in similar experiments [5], [7], [10], [20], [21] under broadband excitation from a lamp. This result is expected since there is direct correspondence between the photon flux and the number of photogenerated holes. However the photocurrent results only from the holes that participate in the etching process according to the chemical equation (CE. 41). This is because OH^- ions are essential for the Ga oxidation, thereby, at a given OH^- concentration, the photocurrent (detected electrons in an external circuit; equal to the number of holes participating in the etching process) increases linearly with the light intensity [20].

Our data are coherent with Youtsey's [3] who shows this linearity up to the power of 50mW/cm^2 for stirred KOH solution. However, we do not observe any sublinear behaviour of the photocurrent due to the fact that we do not use such big powers. For such sublinearity, Macht et al [20] have claimed that the photon flux is higher than the flux of OH^- ions $(\Phi_{OH^-})<(\Phi_p)$ (4.12). The OH^- ions at the etched surface are depleted. In this case the rate of the surface reaction is determined by mass transport of OH^- ions and the limiting photocurrent depends on the pH of the solution and the hydrodynamics of the system. In contrast, in the linear regime the flux of OH^- ions (Φ_{OH^-}) to the surface is larger than the flux of the photogenerated holes to the surface (Φ_p); i.e. $(\Phi_{OH^-})>(\Phi_p)$ (4.13), then the photocurrent is determined by the light intensity. In this case the number of holes transferred across the semiconductor/solution interface per absorbed photon is high. It corresponds to normal depletion, i.e. a change in applied potential results in a corresponding change of the space-charge layer potential (see Eq. 4.2 & 4.3). If the solution is not stirred then a considerably lower photocurrent is observed. Since the rate of photogeneration of holes is higher than the rate of their reaction at the surface, considerable electron-hole recombination must occur, even in the limiting photocurrent range. The surface reaction is kinetically limited and the space-charge layer potential becomes independent of the applied potential because of the accumulation of positive charge at the interface, the potential changes across the Helmholtz layer in solution.

Figure 4.11 also reveals strong dependence of the photocurrent on the excitation wavelength near GaN bandgap. Notably there is an apparent increase in the photocurrent when illuminating at 361.17nm. This could be attributed to the onset of absorption at the GaN bandgap. Such enhancement in the photocurrent would not have been possible to observe using broadband excitation of previous reports. To shed more light on this resonant behaviour we performe several experiments on GaN and $Al_{0.32}Ga_{0.68}N$ samples (sample 2 and 3), keeping same conditions (KOH concentration

0.01M, dc bias 4V, and stirring) while tuning the excitation wavelength between 345-375 nm (see Fig. 4.12a), keeping the same power density of 8.4 mW/cm^2.

The samples are lithographically patterned into a grid of 40x40 μm^2 squares with 100 nm thick Ti layer as a mask, as depicted in Figure 4.5 & 4.7. The bias is applied through an Indium contact on the side of the sample and a Pt-electrode dipped inside the electrolyte solution, as shown in Figure 4.7.

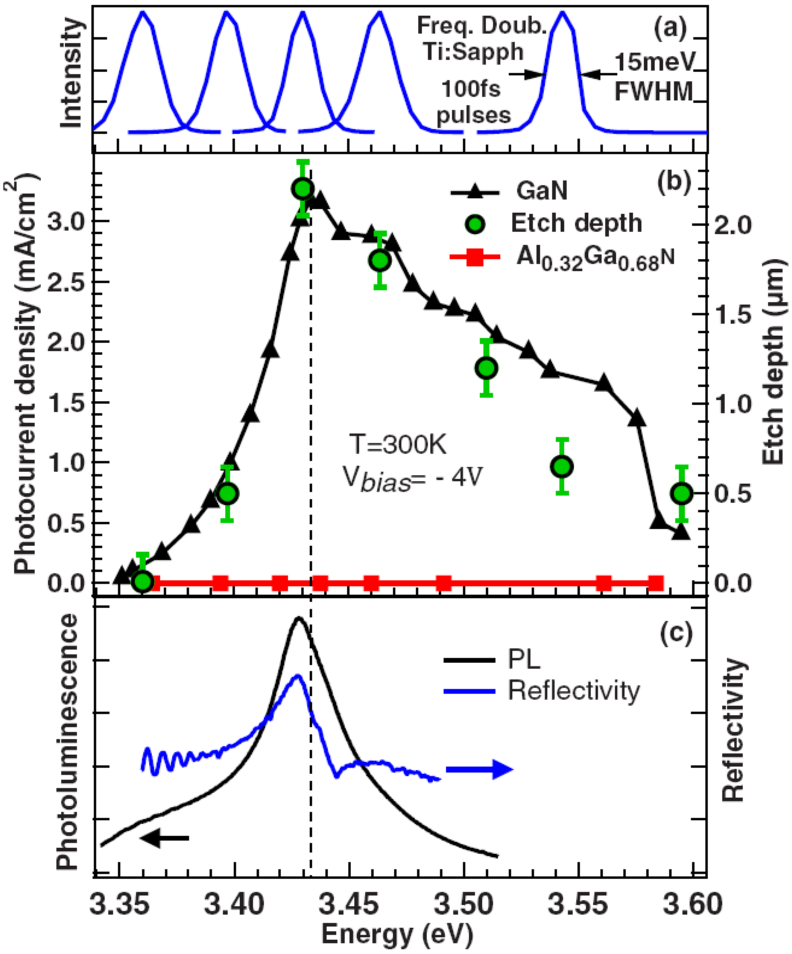

FIG. 4.12. (a) Frequency-doubled, Ti:Sapphire 100 fs pulses with photon energies ranging from 3.3 to 3.6 eV used in PEC etching. (b) Excitation energy dependence of the photocurrent (triangles) during PEC etching of the GaN sample and the corresponding etch depths (circles). The photocurrent under same conditions for the AlGaN sample is also shown (squares), (c) photoluminescence, and reflectivity spectra at room temperature of the GaN sample.

The excitation source is the femtosecond laser described in paragraph 4.6. Typical spectra from UV laser pulses with excitation energies tuned across the GaN bandgap are presented in Fig. 12(a). The resulting photocurrent is measured using the digital multimeter monitoring apparatus when the sample is reversed biased at 4 V.

Figure 4.12(b) shows photocurrent measurements taken on the GaN sample with varying excitation energy, keeping the excitation power density constant at 8.4 mW/cm^2. We observe a sharp increase in the photocurrent with the onset of GaN absorption at 3.40 eV. For comparison, same measurements are performed on the AlGaN sample. As expected, for excitation below AlGaN bandgap no photocurrent is observed underscoring the fact that no photogenerated carriers are produced. Figure 4.12(b) also reveals a strong resonance in the photocurrent centered at 3.43 eV. This is attributed to the excitonically enhanced absorption as evidenced from the reflectivity and luminescence data on the same sample shown in Figure 4.12(c). The detailed study of reflectivity as a function of temperature clearly shows that the reflectivity spectrum at room temperature is dominated by the *A* and *B* excitonic absorption resonances of GaN, separated by a kink in the reflectivity spectrum of Figure 4.12(c). The photoluminescence data strongly support the above claim.

To confirm that the photochemical etch rate is proportional to the photocurrent we performe several etching runs at various excitation energies, keeping the same excitation power density and exposure time. Following the etching, the samples are dipped in a concentrated KOH solution to remove the residual oxide by-products and are then characterized by scanning electron microscope (SEM). Their etch depths are analyzed by alpha step profilometer.

In Fig. 4.13, a series of SEM images are presented corresponding to excitation at selected excitation energies across the GaN bandgap: (a) before the etching, (b) at 3.36 eV, (c) at 3.43 eV, and (d) at 3.54 eV. Before the etching, a smooth GaN surface is seen, patterned with the 100 nm thick Ti mask. The Ti mask serves multiple purposes. First, it allows an assessment of the etch anisotropy and second it provides precise reference for the determination of the etch depth. As expected, negligible etch rates are seen in Fig. 4.13(b) for excitation below the GaN bandgap. The small roughness is attributed to etching caused by the photogenerated carriers in the absorption tail and to the small spectral broadening of the excitation pulse. Excitation at the photocurrent peak, exploiting resonantly enhanced excitonic absorption, results in an etch depth of 2.2 μm with relatively sharp sidewalls. The resonant behaviour is further confirmed in Fig. 4.13(d), where excitation at higher energy, yields smaller etching depth.

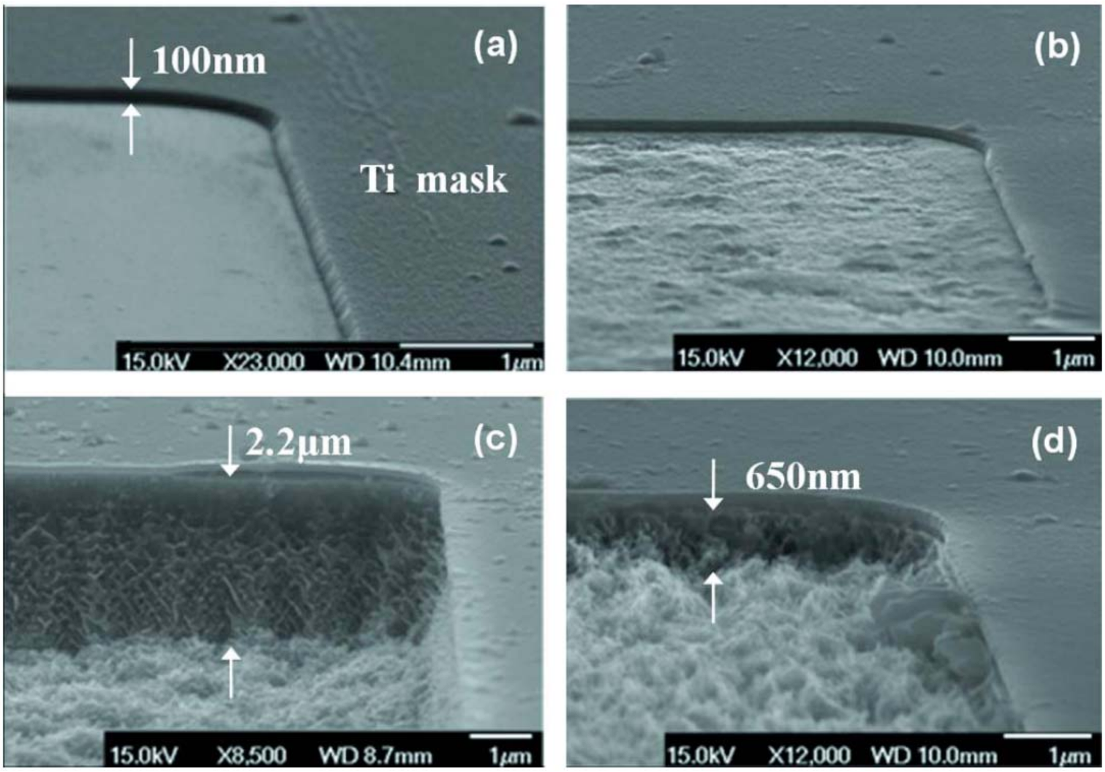

FIG. 4.13. SEM pictures of: (a) Ti patterned GaN sample before the etching, (b) when PEC etched under illumination at 3.36 eV, (c) at 3.43 eV, and (d) at 3.54 eV. All samples were dipped in a KOH solution to remove the residual oxide by-products.

The extracted etch depths in Fig. 13(b) are recorded for several excitation energies, as shown in Fig. 12(a). The resulting etching depths follow nicely the measured photocurrent profile. Small discrepancies between etch depths and photocurrent profile for excitation at higher energies could result from particular surface morphology during etch, affecting the intensity of the penetrated light at the etch front and modifying slightly the etch rates.

The above results suggest that PEC etching under resonant excitation at the GaN exciton energy is by far more efficient compared to the excitation by broadband lamp source. In addition, it opens exciting possibilities to exploit the bandgap selective nature of PEC etching, as a tool to achieve a truly selective etching technique for fabrication of optoelectronic devices that require smooth optical quality surfaces. Indeed, PEC experiments on the AlGaN sample with excitation at 3.43 eV reveale no etching at all.

4.8 Surface Morfology of PEC GaN Etching

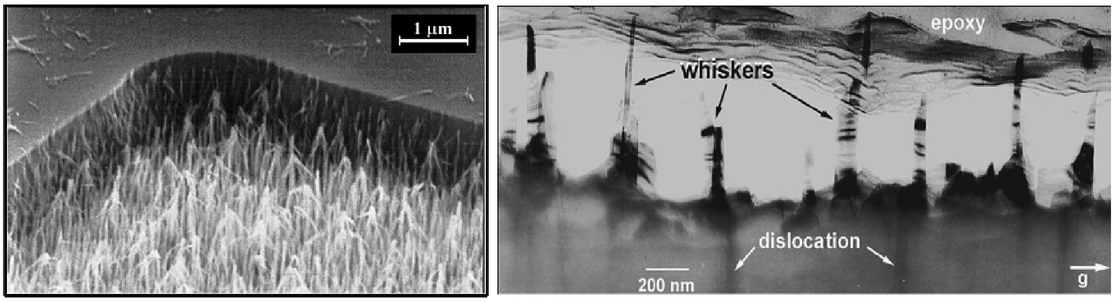

FIG. 4.14 (a). Scanning electron micrograph of a PEC etched GaN surface after 60min of etching. The etched whiskers exhibit diameters between 10 and 50nm and lengths of 1 mm or more. (b) Low-magnification cross-sectional transmission electron micrograph of the etched GaN film. Visible in this image are the etched whiskers as well as the dislocations in the underlying, unetched GaN film [8].

The Photoelectrochemical etching was initially used as an essential, fast (compared to the TEM method) and affective tool for the assessment of the defect density in GaN. This method was used after one-to-one correlation between whiskers and dislocation sites for Ga-polar layers showing also that whiskers are formed on narrow inversion domains in N-polar layers [22], [23]. In addition, C. Youtsey [8] and R. P. Strittmater [11] showed a correlation between the etched features called whiskers and threading dislocations in the unetched film, using transmission electron microscopy studies, as depicted in Figure 4.14.

On the other hand, surface morphology in PEC etching, when it is used as a nitrides processing tool, instead of a defect characterization technique, is critical for the fabrication of new optoelectronic devices which require optical flatness in order to achieve good performance. When PEC etching is conducted in the "carrier limited" regime, during which the recombination of photogenerated holes with electrons reduces the dissolution rate at surface defects, needles are formed at threading dislocations sites in GaN (see Figures 4.14(a) & (b)). Clearly these conditions correspond to potential range II of Figure 4.9. On the other hand, smooth surfaces and polishing of GaN is expected in the limiting photocurrent range III ("diffusion limited" regime), when the flux of OH^- ions is rate-determining $(\Phi_{OH-})<(\Phi_p)$ [20]. It is obvious that when PEC etching is about to be used in the all-dielectric GaN microcavity fabrication process, it must be performed in a “diffusion limited” regime.

4.8.1 The Role of Stirring

Stirring plays a significant role on the surface morphology. When the solution is stirred, what happens is an increase of the OH^- ions flux in comparison to the photon flux. Thus, it is more possible to create a “carrier limited” regime than a “diffusion limited” regime. In general , stirring leads to rough surfaces.

Youtsey et al [3] observe that the stirred solutions show an approximately linear relationship between light intensity and etch rate. A similar dependence is reported by Minsky *et al.* [4] and is characteristic of photoenhanced etch processes in which the etch rate depends upon the number of photogenerated carriers. The unstirred solution exhibites a saturation in etch rate at higher light intensities, which indicates that the etch process becomes diffusion limited for the increased reaction rates in this high intensity regime.

4.8.2 Oxide Removal

An inevitable consequence of the PEC etching process is the creation of oxide by-products at the semiconductor surface. Several methods have been proposed in the literature as possible techniques for oxide removal [23] based on concentrated HCl or KOH solutions. Under certain etching conditions, the etched surface has the ability to self-clean, often seen as an oscillation of the photocurrent due to the buildup and gradual dissolution of the oxide layer as depicted in Figure 4.15 [24]. This behaviour is confirmed in most cases of our experiments since dipping the etched samples in a concentrated KOH solution does not alter the depth nor the roughness of the etched surface.

The surface cleaning mechanism can be understood from the data below. The oscillations mentioned above, as depicted in Figure 4.15, are extracted by another PEC experiment on an unintentionally doped uid 10^{16} cm^{-3} GaN (0001) (sample 2), blocking periodically the excitation beam for twenty seconds, creating “light” and “dark” time windows. This exponential photocurrent degradation during “light” times is attributed to the oxide formation (see Fig. 4.16). During “dark” times, dissolution of the oxide layer cleans the etched surface, exposing a new GaN interface in the electrolyte for further etching.

Oxides are not always dissolved. In Figure 4.16(a) one can see a characteristic SEM image of the porous oxide formed during PEC etching of GaN, which by coincidence, is not dissolved during the etching process. This turns to be a good occasion to study its structure and learn how to remove it after every PEC etching experiment.

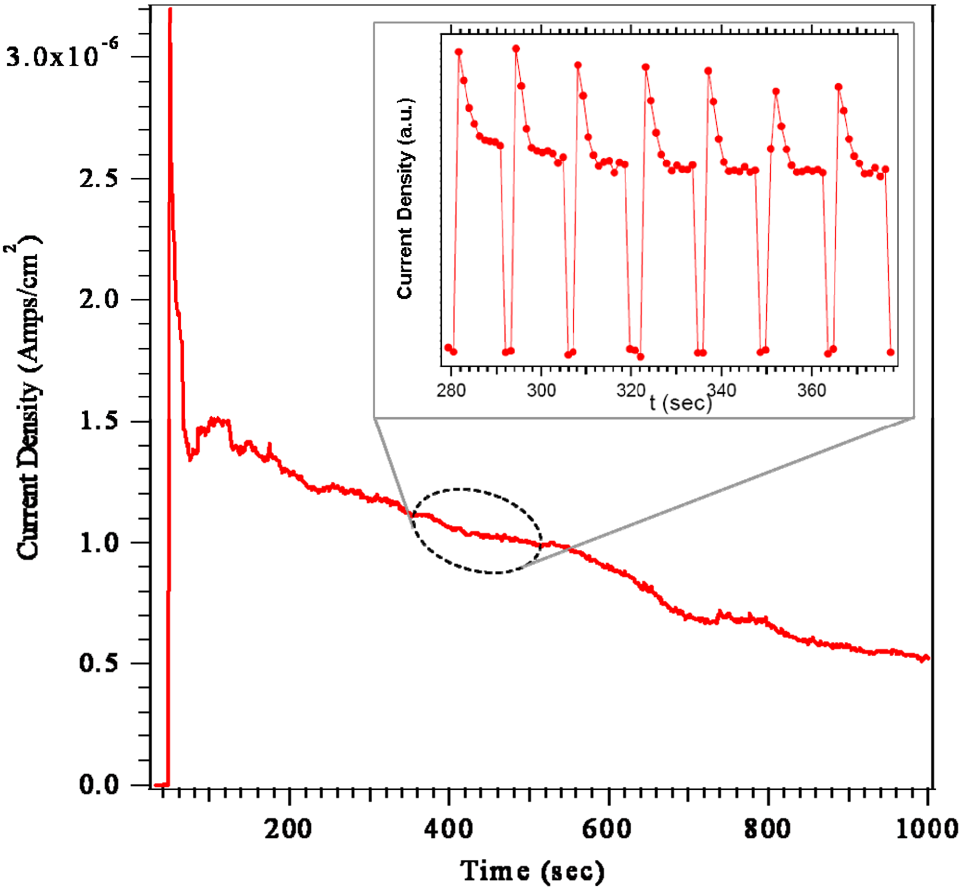

FIG. 4.15 Typical “saw” structure oscillation of the photocurrent during PEC etching of GaN. The exponential decay of the photocurrent is attributed to the oxide formation. When the shutter closes the electrolyte etches the oxide and when it opens, the photocurrent reaches its initial value

This porous oxide layer, was completely removed when immersed in concentrated HCl solution, exposing a deep square of recessed GaN with a rough surface, as illustrated in Figure 4.16(b). We believe that this oxide has no residual chemical bonds with the underlying GaN layer and it may also be removed mechanically, as it will be shown in the next paragraph.

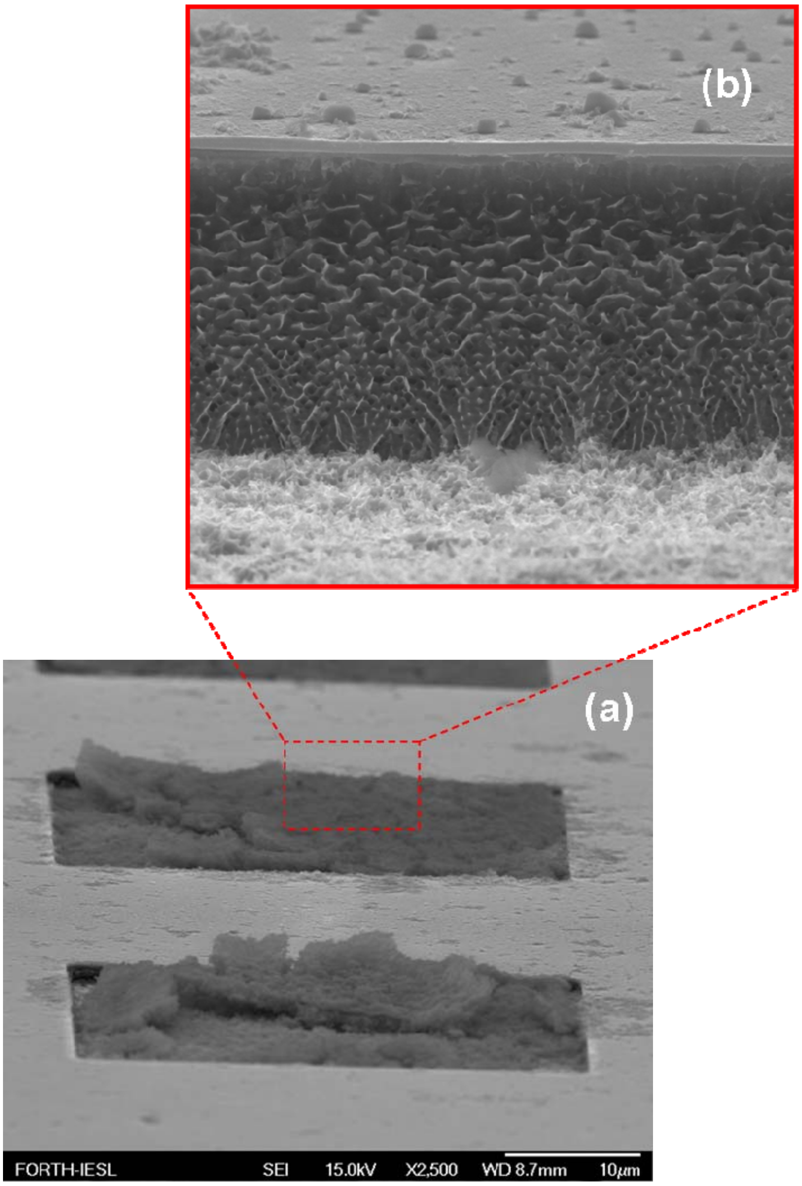

FIG.4.16. a) SEM image of a porous GaN oxide after PEC etching experiment, b) SEM image of a recessed GaN patterned square after PEC etching experiment and itsoxide removal.

4.9 Truly Bandgap Selective PEC Etching of Nitrides

Since we show this resonant photocurrent enhancement, which is a direct evidence of selectivity of PEC etching method, we design a series of experiments to investigate this issue. High bandgap selectivity corresponds to ultra smooth etched surfaces of nitride layers, required for high performance of optoelectronic devices.

Samples 4 and 5, described in paragraph 4.5, are used in such bandgap selective PEC etching experiments. In the case of sample 4 we selectively etch the whole top 50nm $In_{0.1}Ga_{0.9}N$ layer until we reach the bulk GaN layer below. As an excitation source we use a solid state laser diode, emitting at 405nm, very close to resonance of $In_{0.1}Ga_{0.9}N$, so we can achieve maximum photocurrent and etch rate. The illumination power density is 22mW/cm^2, which is quit high compared to other PEC etching experiments of other groups.

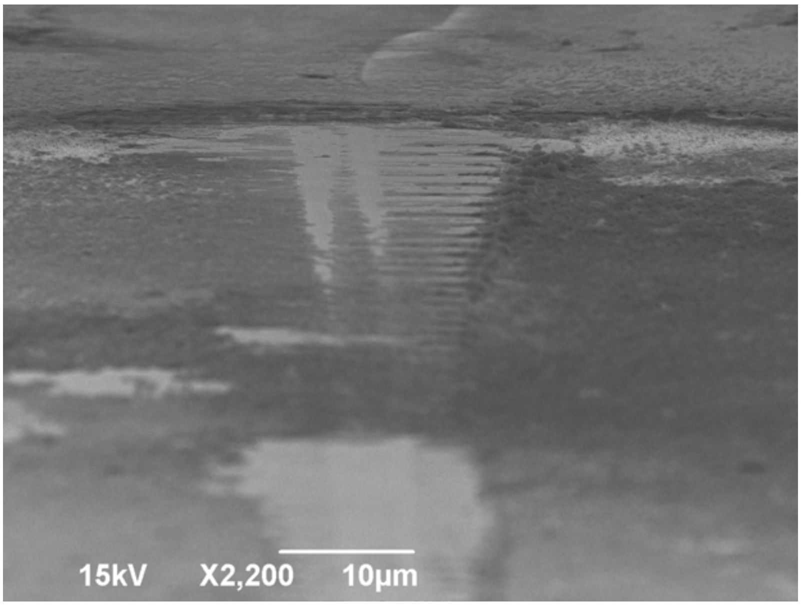

FIG. 4.17. SEM image of the a-step tip scan on a PEC etched $In_{0.1}Ga_{0.9}N$ surface.

Initially, the sample is not lithographically patterned. Thus, the exposed to the electrolyte and photons circular area is Ø1mm wide. The PEC etching of $In_{0.1}Ga_{0.9}N$ is terminated by itself when the underlying GaN layer is reached. It seems possible obtaining smooth surfaces by simply allowing a long enough exposure to obtain a clean etched surface, without causing damage to the underlying higher bandgap semiconductor layer. Interestingly, the implementation of this bandgap selective PEC etching experiment lifts the necessity to perform oxide removal, after confirming its existence using an SEM image. An attempt to mechanically remove this porous oxide film using the tip of an alpha-step profilometer, reveals an evidence of a scratch of this oxide and a very smooth GaN surface beneath, as illustrated in Figure 4.17.

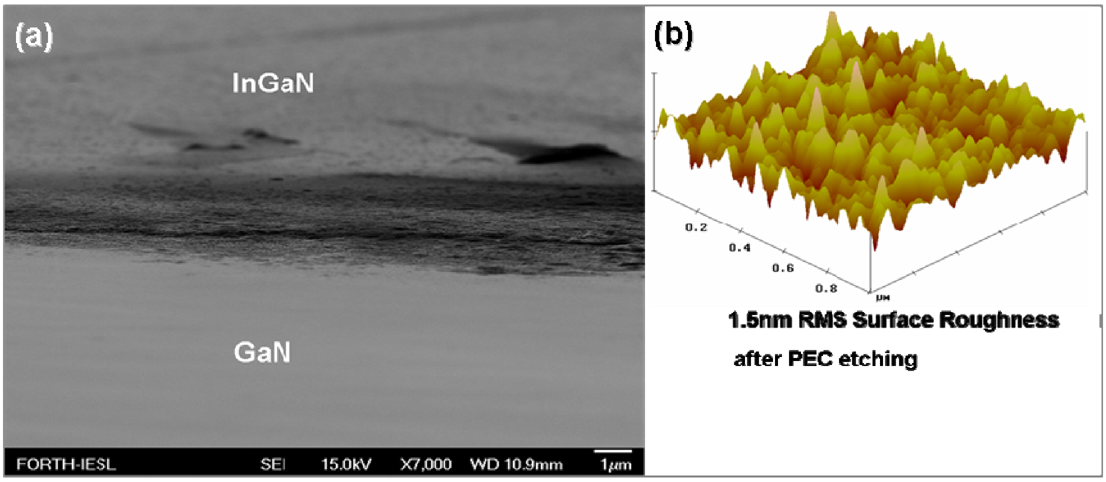

FIG. 4.18. a) SEM image of the a-step tip scan on a PEC etched $In_{0.1}Ga_{0.9}N$ surface. The sample was used is consisted of 50nm thick $In_{0.1}Ga_{0.9}N$ layer, undoped, b) AFM image of the GaN layer just above the fully etched $In_{0.1}Ga_{0.9}N$ layer.

This etched broad and unpatterned surface, permits the use of an ordinary cotton bud to wipe out the oxide by-products of the PEC etching, when immersed in to acetone, in a very gently way, without harming the GaN surface (see Fig. 4.18(a)). An AFM experiment on this cleaned GaN surface measured 1.5nm RMS surface roughness, depicting the fact that resonantly enhanced bandgap selective PEC etching among nitrides with different bandgap may yield ultra smooth surfaces, appropriate for optoelectronic applications.

Such bandgap selective PEC etching is verified by performing experiments on sample 5, using excitation centered at 3.40 eV to selectively etch GaN over $Al_{0.2}Ga_{0.8}N$. The sample is patterned with Ti to assess the etch anisotropy and etch depth, which is found to be independent of exposure time. The PEC etch process stops naturally as the etching front reaches the $GaN/Al_{0.2}Ga_{0.8}N$ interface, resulting in a sharp 350 nm sidewall, shown in Figure 4.19. This shows also that the underlying etched surface is smooth and requires no oxide removal procedure. Lying on that we may claim that resonantly enhanced bandgap selective PEC etching of nitrides is a usefull tool for pattern transfer from a top nitride layer to an other below, with a greater bandgap.

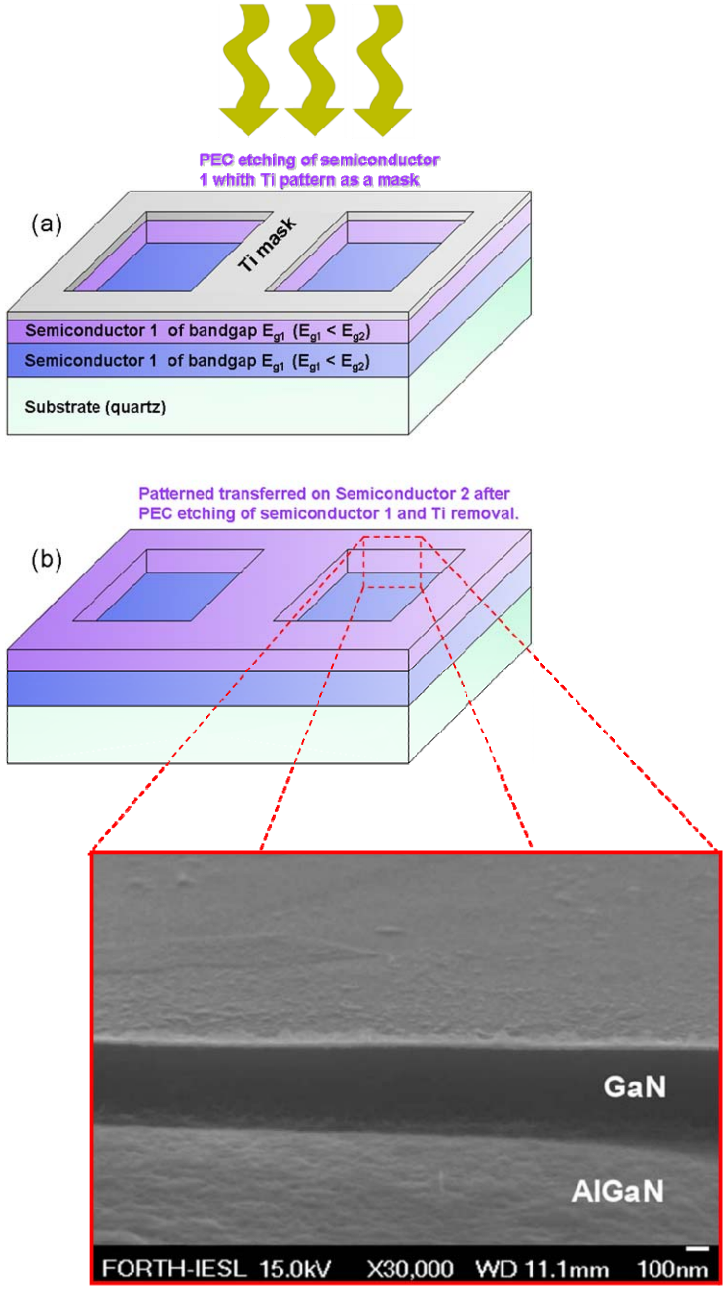

FIG. 4.19. SEM picture following selective PEC etching of GaN on $Al_{0.2}Ga_{0.8}N$ showing sharp sidewalls and smooth etched surface. The 350 nm sidewall which is independent of etch time proves the bandgap selective nature of the etching process. The Ti mask was removed to measure the real etch depth, corresponding to the thickness of the GaN layer

In these bandgap selective PEC etching experiments os samples 4 and 5, the photocurrent begins with the high value of ~1mA/cm^2 and then it follows almost an exponential decay (Fig.4.20), until it reaches a plateaux. This behaviour of the exponentially decreasing photocurrent is due to the formation of an oxide film on the etched surface during etching. This oxide acts as a spacer between the solution and the semiconductor, decreasing the photocurrent and the etch rate respectively. The decrease lasts until the establishment of a dynamic equilibrium state in which the dissolution of the oxide is equal to the semiconductor oxidation, leading to a constant value of photocurrent (plateaux).

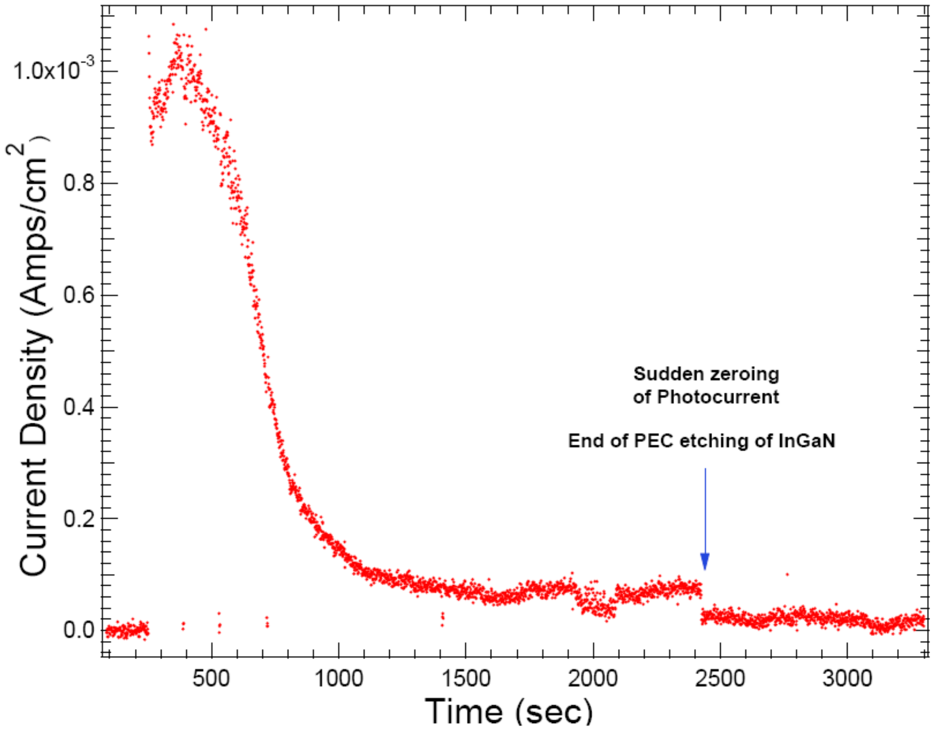

FIG. 4.20. Plot of the photocurrent density versus time during the PEC etching of an InGaN layer. At ~2400sec one can clearly see the PEC etching process stopping by itself when reaching a layer of a greater to the excitation energy bandgap.

When the $In_{0.1}Ga_{0.9}N$ layer, for example, is entirely etched (see Fig. 4.20), the photocurrent stops by itself evidencing the fact that the photoelectrochemical wet etching of the InGaN layer has been terminated. This very fast drop in the photocurrent clearly shows the selective nature of the PEC etching. As soon as InGaN bonds have completely vanished, the combination of the electrolyte and the biasing cannot not attack the underlying GaN layer without the presence of the proper excitation energy above GaN bandgap. Therefore, PEC etching was instantly stopped, yielding instantly zero photocurrent.

4.10 N-face Polarity of GaN & Inversed Pyramid Morphology

One of the samples grown for the study on the dependence of nitrides PEC etching on the excitation energy, replica of sample 4, has shown an anusual surface morphology. The inversed pyramid structure. This InGaN layer has a thickness above its critical one, due to excess of Indium content in its alloy, resulting in a cracked surface.

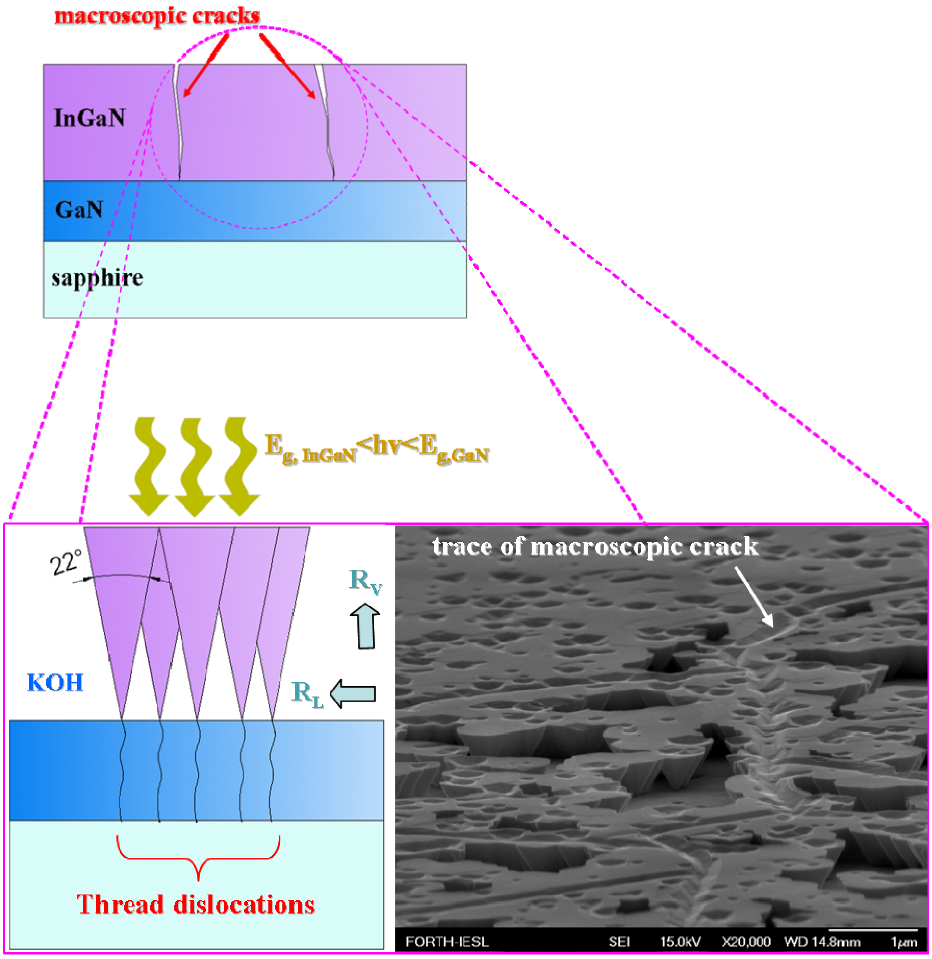

FIG. 4.21. SEM image of the inversed InGaN pyramids corresponding to the thread dislocations.

During PEC etching, the electrolyte penetrates its macroscopic cracks and attacks its facets (see Figure 4.21), which exhibit a mixed Ga and N-face polarity, as depicted in Figure 4.22. N-face polarity $\left(000\bar{1}\right)$ of GaN and in nitrides in general exhibits negligible resistance to alkali and acid solutions [25]. Thus, the InGaN layer is etched in both lateral and vertical direction, as depicted in Figure 4.21.

Thread dislocations within the InGaN layer derived from the bulk GaN below, behave as recombination centers, suppressing the PEC etching. This leads to reduced etching around each thread dislocation. Simultaneously, the naturally evolution of pure chemical etching along the vertical axis shows a crystallographic preference. The combination of crystallographic vertical etching and the suppressed due to recombination lateral etching of the InGaN layer results in the pyramidal structure depicted in Figure 4.20.

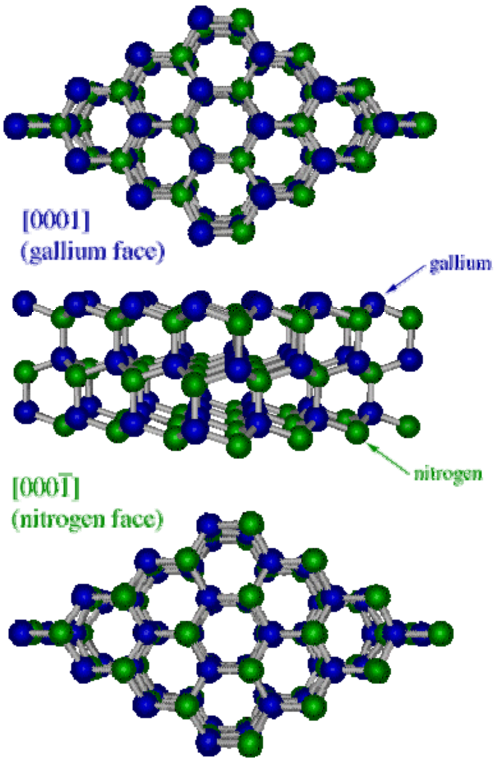

FIG. 4.22. The hexagonal wurtzite crystal structure of GaN. The c-plane or $\left(0001\right)$ direction is a very resistive to all kind of etchants (including HF) at room temperature. On the contrary, the $\left(000\bar{1}\right)$ direction can be very easily etched even by low concentration acid or alkali solutions. (www.ece.cmu.edu/~dwg/research/polarity.html).

This inversed pyramid structure is important because we will meet it in the case of lateral PEC etching. Pyramids increase the N-face surface roughness of the GaN membranes which will be incorporated in all-dielectric GaN microcavities. Suppressing this pyramid formation by tuning the lateral PEC etching conditions is a critical factor for the performance of a stongly coupled GaN polariton microcavity.

4.11 Conclusions

In conclusion, we demonstrate strong dependence of the PEC etching photocurrent on the excitation energy marked by sharp resonant excitonically enhanced absorption in GaN. The corresponding etching rates are consistent with the photocurrent measurement on the same sample. The demonstrated selective etchings of GaN on AlGaN and of InGaN on GaN suggest that the technique can be used as a fundamental tool for processing nitride semiconductors. This gives particular advantages for the fabrication of optoelectronic devices that require optical flatness, like all-dielectric GaN microcavities.

References

[1] I. M. Tiginyanu, G. Irmer, J. Monecke, and H. L. Hartnagel, “Micro-Raman-scattering study of surface-related phonon modes in porous GaP,” *Physical Review B*, vol. 55, no. 11, p. 6739, Mar. 1997.

[2] H. Morkoç, *Handbook of Nitride Semiconductors and Devices, Electronic and Optical Processes in Nitrides*. Wiley-VCH, 2008.

[3] C. Youtsey, I. Adesida, and G. Bulman, “Highly anisotropic photoenhanced wet etching of n-type GaN,” *Applied Physics Letters*, vol. 71, no. 15, p. 2151, 1997.

[4] M. S. Minsky, M. White, and E. L. Hu, “Room-temperature photoenhanced wet etching of GaN,” *Applied Physics Letters*, vol. 68, no. 11, p. 1531, 1996.

[5] L. Peng, C. Chuang, J. Ho, C. Huang, and C. Chen, “Deep ultraviolet enhanced wet chemical etching of gallium nitride,” *Applied Physics Letters*, vol. 72, no. 8, p. 939, 1998.

[6] T. Rotter et al., “Photoinduced oxide film formation on n-type GaN surfaces using alkaline solutions,” *Applied Physics Letters*, vol. 76, no. 26, p. 3923, 2000.

[7] C. Youtsey, I. Adesida, L. T. Romano, and G. Bulman, “Smooth n-type GaN surfaces by photoenhanced wet etching,” *Applied Physics Letters*, vol. 72, no. 5, p. 560, 1998.

[8] C. Youtsey, L. T. Romano, and I. Adesida, “Gallium nitride whiskers formed by selective photoenhanced wet etching of dislocations,” *Applied Physics Letters*, vol. 73, no. 6, p. 797, 1998.

[9] Y. Gao, I. Ben-Yaacov, U. K. Mishra, and E. L. Hu, “Optimization of AlGaN/GaN current aperture vertical electron transistor (CAVET) fabricated by photoelectrochemical wet etching,” *Journal of Applied Physics*, vol. 96, no. 11, p. 6925, 2004.

[10] E. D. Haberer et al., “Free-standing, optically pumped, GaN/InGaN microdisk lasers fabricated by photoelectrochemical etching,” *Applied Physics Letters*, vol. 85, no. 22, p. 5179, 2004.

[11] R. P. Strittmatter, R. A. Beach, and T. C. McGill, “Fabrication of GaN suspended microstructures,” *Applied Physics Letters*, vol. 78, no. 21, p. 3226, 2001.

[12] V. A. Myamlin and Y. V. Pleskov, “THE ELECTROCHEMISTRY OF SEMICONDUCTORS,” *Russian Chemical Reviews*, vol. 32, no. 4, pp. 207-223, 1963.

[13] F. O. Arntz, “Electrochemistry of Semiconductors. Viktor A. Myamlin and Yurii V. Pleskov. Translated from the Russian edition (Moscow, 1965). Plenum, New York, 1967. xxiv + 430 pp., ilius. $19.50,” *Science*, vol. 160, no. 3831, pp. 984-984, 1968.

[14] S. Chandra and R. K. Pandey, “Semiconductor Photoelectrochemical Solar Cells,” *physica status solidi (a)*, vol. 72, no. 2, pp. 415-454, 1982.

[15] A. J. Bard et al., *Encyclopedia of Electrochemistry, 10 Volume Set + Index*, 1st ed. Wiley-VCH, 2007.

[16] J. Reichman, “The current□voltage characteristics of semiconductor□electrolyte junction photovoltaic cells,” *Applied Physics Letters*, 1980. [Online]. Available: 10.1063/1.91551. [Accessed: 29-Aug-2010].

[17] M. Ono et al., “Photoelectrochemical reaction and H[sub 2] generation at zero bias optimized by carrier concentration of n-type GaN,” *The Journal of Chemical Physics*, vol. 126, no. 5, p. 054708, 2007.

[18] V. M. Arutyunyan, “Physical properties of the semiconductor-electrolyte interface,” *Soviet Physics Uspekhi*, vol. 32, no. 6, pp. 521-542, 1989.

[19] V. Cimalla, J. Pezoldt, and O. Ambacher, “Group III nitride and SiC based MEMS and NEMS: materials properties, technology and applications,” *Journal of Physics D: Applied Physics*, vol. 40, no. 20, pp. 6386-6434, 2007.

[20] L. Macht, J. Kelly, J. Weyher, A. Grzegorczyk, and P. Larsen, “An electrochemical study of photoetching of heteroepitaxial GaN: kinetics and morphology,” *Journal of Crystal Growth*, vol. 273, no. 3, pp. 347-356, 2005.

[21] E. Trichas et al., “Selective photochemical etching of GaN films and laser lift-off for microcavity fabrication,” *physica status solidi (a)*, vol. 205, no. 11, pp. 2509-2512, 2008.

[22] J. L. Weyher, F. D. Tichelaar, H. W. Zandbergen, L. Macht, and P. R. Hageman, “Selective photoetching and transmission electron microscopy studies of defects in heteroepitaxial GaN,” *Journal of Applied Physics*, vol. 90, no. 12, p. 6105, 2001.

[23] J. Skriniarová, A. van der Hart, H. P. Bochem, A. Fox, and P. Kordos, “Photoenhanced wet chemical etching of n+-doped GaN,” *Materials Science and Engineering B*, vol. 91, pp. 298-302, Apr. 2002.

[24] M. Mynbaeva, M. Kayambaki, K. Mynbaev, and K. Zekentes, “On application of electrochemical capacitance–voltage profiling technique for n-type SiC,” *Semiconductor Science and Technology*, vol. 23, no. 7, p. 075039, 2008.

[25] J. L. Weyher, L. Macht, F. D. Tichelaar, H. W. Zandbergen, P. R. Hageman, and P. K. Larsen, “Complementary study of defects in GaN by photo-etching and TEM,” *Materials Science and Engineering B*, vol. 91, pp. 280-284, Apr. 2002.

Chapter 5: Selective Lateral Photoelectrochemical Etching of Nitrides

5.1 From Vertical to Lateral Direction

Wet photo-electrochemical (PEC) etching of nitrides has emerged as a promising tool for all-dielectric GaN microcavity fabrication, since we managed achieving smooth Ga-face polarity GaN etched surfaces and selective etching among nitrides with different bandgap [1], [2] in vertical direction (0001). This is attributed to the combination of resonantly enhanced etching rates with a thin KOH solution of 0.01M, in the "diffusion limited" regime of PEC etching. However, whenever PEC etching has been used, in the lateral direction, especially in applications requiring thin membranes [3-6] , no significant evidence of ultra smooth N-face polarity nitride etched surfaces is demonstrated. Contrary, cone-shaped (inversed pyramid) morphology [7-10] is observed, similar to that shown in paragraph 4.10, limiting the membranes' optical quality and their usability in devices. It is clear that the implementation of lateral PEC etching in optoelectronic device processing requires further optimization of the process, such that it will be able to produce optically flat laterally etched surfaces without any optical damage.

5.2 Inversed Pyramid Morphology

Stonas et. al. [8], [9], who are the first showing the dopant selective nature of the photoelectochemical etching of III-nitrides, observe the inversed pyramid structure, depicted in Figure 5.1(a). The pyramids, as all ready mentioned in the previous Chapter, are the result of the same order of magnitude of both the vertical and lateral etch rates of the sacrificial layer. The combination of pure chemical crystallographic vertical etching of the N-face polarity n-GaN and the suppressed due to recombination lateral PEC etching of this sacrificial layer results in the pyramidal structure (see Fig. 5.1(b)).

The angle of the cone (22°) is preserved through the etch process and is determined by the choice of the of PEC and material parameters, including the absorption depth of the incident light within the GaN, the distribution of photogenerated holes on the illuminated surface, the chemical reactivity of the electrolyte used (KOH) and its crystallographic dependence. Especially when the sample is illuminated from the backside (sapphire side), areas with defects (dislocations) are slowly etched, enhancing the pyramidal structure.

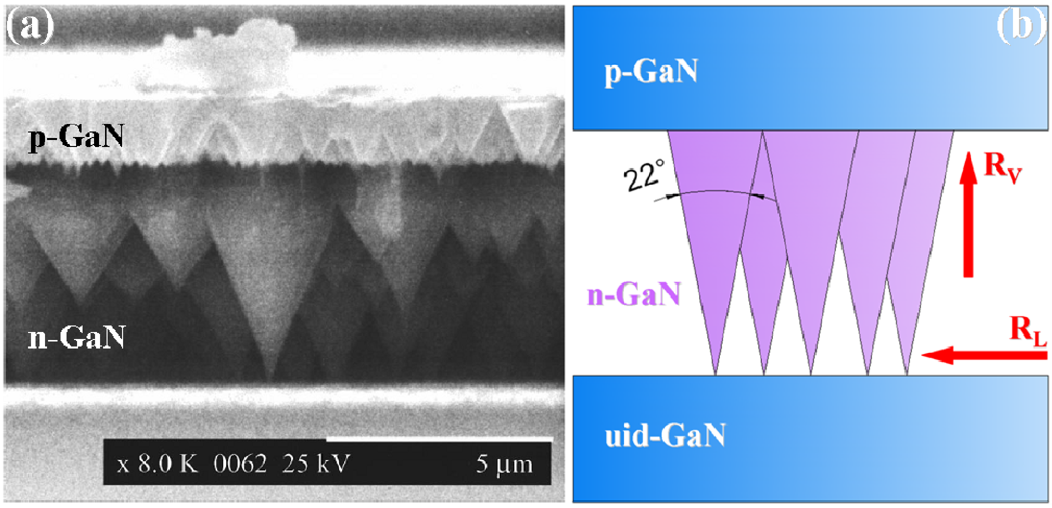

FIG. 5.1. a) SEM image of an n-type sacrificial GaN layer etched below a p-type GaN top layer [8], [9]. One can clearly see the inversed pyramid features transferred into the p-type etch-stop layer, “destroying” the selectivity of the PEC lateral process, resulting in an increase of surface roughness. b) Schematic illustration of the inversed pyramid formation mechanism during dopant selective lateral PEC etching of a sacrificial n-type GaN layer.

The transmission of the inversed pyramid feature to the p-type layer above, revealing a fundamental problem in lateral etching PEC experiments in III-nitrides, is attributed to a pure chemical wet etching of the N-face of GaN which shows minimum chemical resistance to acid or alkali solutions, in respect to their concentration. When any kind of selective lateral PEC etching of nitrides (dopant or bandgap) begins, a part of the N-face polarity $\left(000\bar{1}\right)$ GaN surface of the etch-stop layer (ie. p-type GaN) is directly exposed to the etching solution. Low resistivity of $\left(000\bar{1}\right)$ GaN to chemical etching agent tends to suppress the selectivity of the lateral PEC etching.

We believe that our method, based on the advantage of resonantly enhanced bandgap selective PEC etching of an InGaN sacrificial layer, will yield much faster lateral etch rates. The use of the low concentration 0.01M KOH solution will also suppress the pure chemical etching of N-polarity $\left(000\bar{1}\right)$ GaN surface, diminishing the inversed pyramidal structure, leading to better surface quality of GaN membranes, appropriate for the fabrication of all-dielectric microcavities.

5.3 Experimental details

The sample used in these lateral bandgap selective PEC etching experiments is shown in Figure 5.2.

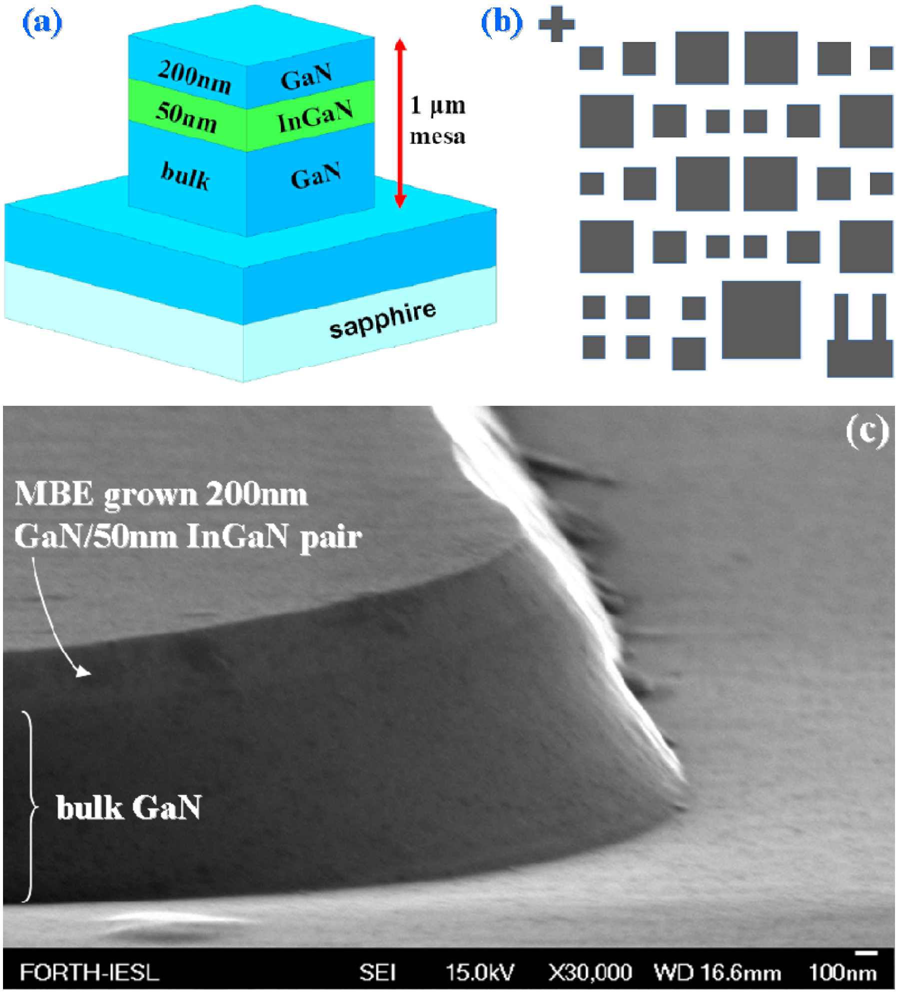

FIG. 5.2. a) Schematic illustration of the sample, specially designed for the bandgap selective lateral PEC etching experiments. b) Figure also shows the mesa formed, in order to expose the facets of the $In_{0.1}Ga_{0.9}N$ layer to the electrolyte, derived from the mask design depicted above. c) SEM image of the 1μm high mesa formed after RIE dry etching.

It consists of a 200nm GaN film followed by a 50nm $In_{0.1}Ga_{0.9}N$ sacrificial layer below critical thickness, grown on top of a 3µm-thick unintentionally-doped GaN on sapphire template (see Fig. 5.2a). The sample is patterned using standard lithographic process into a complex of square mesas of several dimensions ranged from 45x45μm^2 to 155x155 μm^2,, as depicted in Figure 5.2b. 1µm tall mesas are fabricated by vertical reactive ion etching in order to expose the sacrificial $In_{0.1}Ga_{0.9}N$ layer for subsequent selective PEC etching (see Fig. 5.2c). A part of the same sample is patterned using the same mask design with an image reversal process for the fabrication of recessed square patterns.

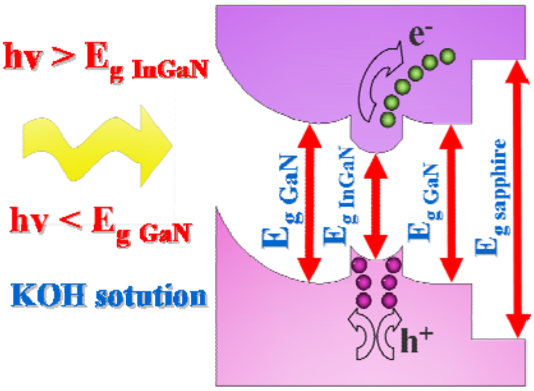

FIG. 5.3. Qualitative schematic illustration of the band diagram of the laterally etched structure with the $In_{0.1}Ga_{0.9}N$ sacrificial layer, when immersed in the electrolyte and excited by a laser diode.

The PEC etching is carried out in an electrochemical cell at room temperature using several concentrations of KOH solution in a setup described in detail in the previous chapter. An Indium ohmic contact was used to apply a reverse DC bias of 4V to the semiconductor, required for the strong confinement of photogenerated holes at the electrolyte/semiconductor interface. Selectivity of the PEC etching process is ensured by resonantly exciting only the sacrificial $In_{0.1}Ga_{0.9}N$ layer, using a below GaN bandgap laser diode source at 405nm as illustrated in Figure 5.3, while varying the concentration of the electrolyte solution by two orders of magnitude. It should be noted that the power density of 0.32 W/cm^2, delivered to the sacrificial layer by bandgap selective excitation, is two orders of magnitude higher than in previous reports [3], [4], [7], [11]. The resulting undercuts of the $In_{0.1}Ga_{0.9}N$ layer and the creation of free-standing GaN membranes are presented in Figure 5.4

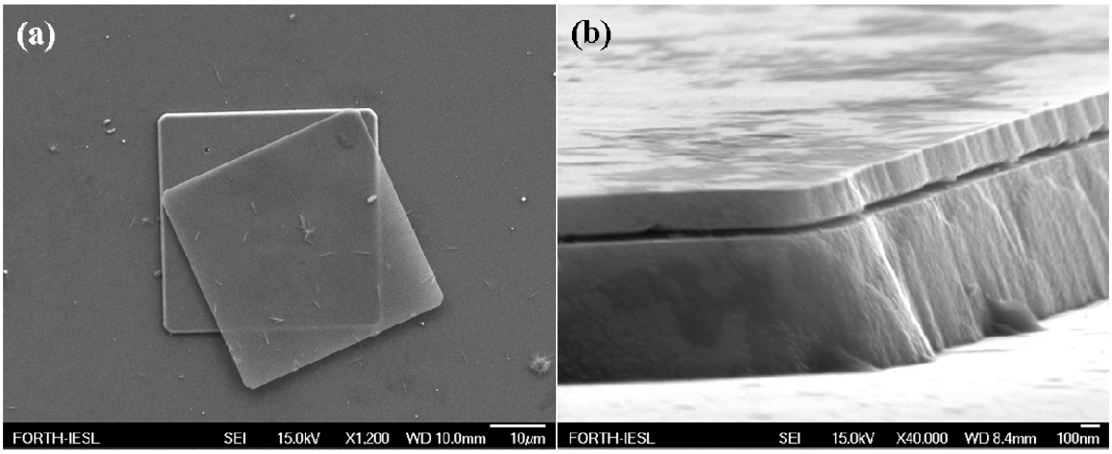

FIG. 5.4. a) Top view,and b) side view of SEM images of a fully under-etched 200nm GaN membranes, standing on top of their corresponding mesas.

5.4 Membrane Manipulation & Optical Characterization

The use of mesas allows easy transport of the detached GaN membranes onto a standard conductive carbon tape without damaging the membranes, provided that the etching has progressed throughout the mesa. This is shown in Figure 5.5, where an array of membranes is transferred onto a carbon tape.

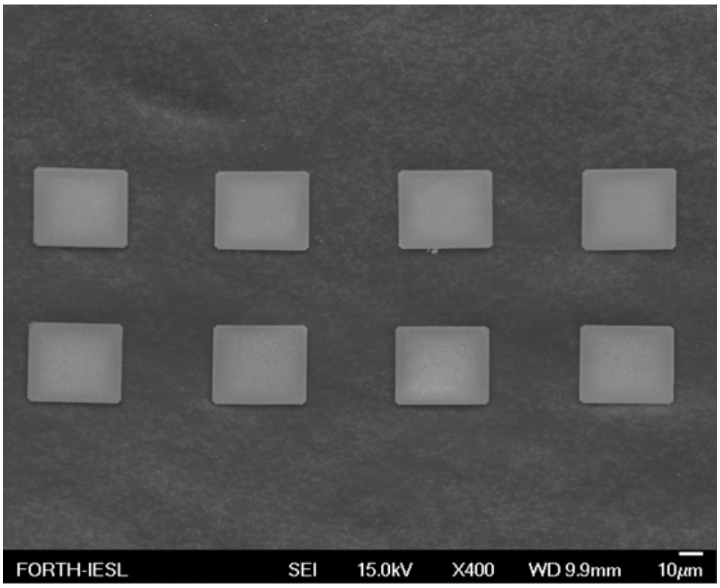

FIG. 5.5. SEM image of detached GaN membranes transferred to carbon tape. The membranes remain intact retaining their original pattern.

It is clear that the lateral PEC etching method can yield a significant number of membranes, over a broad area of a nitride wafer, when done repeatedly, opening exciting possibilities for further processing and integration of the membranes into all-dielectric microcavities.

The technique proved to be very efficient in producing thin GaN membranes whose quality was high. This is verified by Photoluminescence (PL) spectra acquired at room temperature from the GaN membranes mounted on carbon tape. They reveal no apparent degradation in the emission properties of the detached GaN membranes, whereas a small redshift in the PL peak confirms their fully relaxed state, due to bond braking with the underlying $In_{0.1}Ga_{0.9}N$ sacrificial layer. In terms of N-face side surface roughness, best etch results are obtained for low electrolyte concentrations of 0.01MKOH, yielding optically smooth etched surfaces of ~ 6nm rms roughness. The formation of cone shaped surface is confirmed only at higher KOH concentrations in agreement with previous results [7-9].

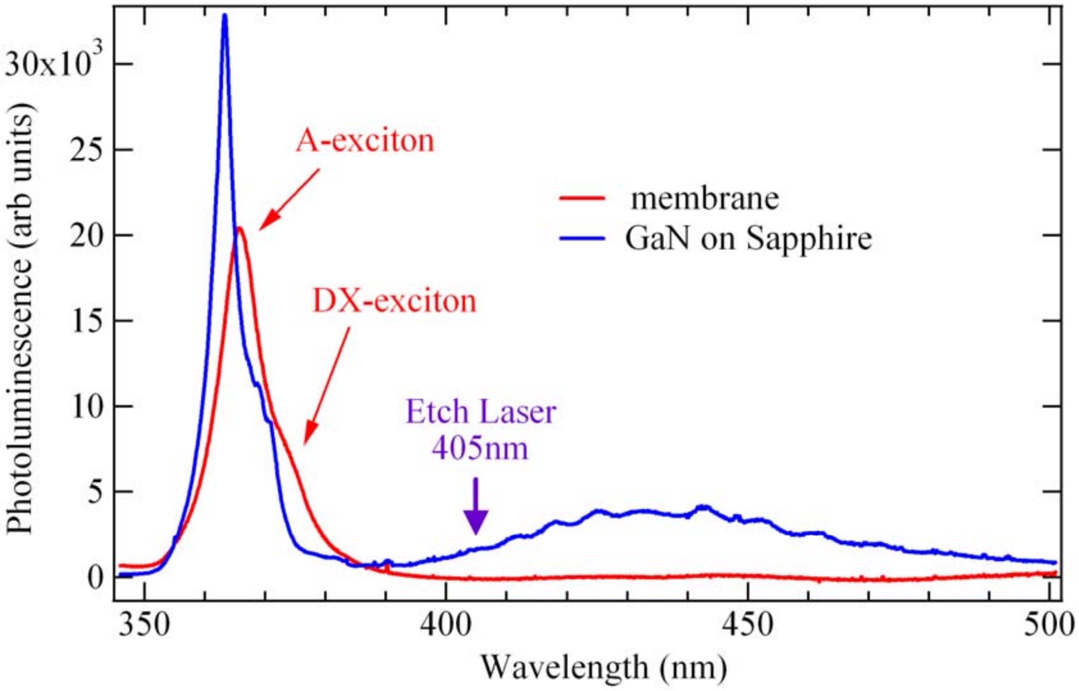

FIG.5.6. Room temperature PL taken from full structure before etching (blue) and from a single freestanding GaN membrane (red), showing redshift due to strain relaxation.

Photoluminescence spectrum shows also another peak, attributed to its donor bound axiton (DX or DBE). Its position suggests complete stress relief [12] This excitonic feature has an oscillator strength, since it corresponds to a radiative transition. However donor bound exciton oscillator strength is not sufficient enough to give strong coupling with a cavity mode when being incorporated in a microcavity. This kind of excitonic emission is verified by the following PL and reflectivity spectra of an MOCVD homoepitaxially grown GaN [13].

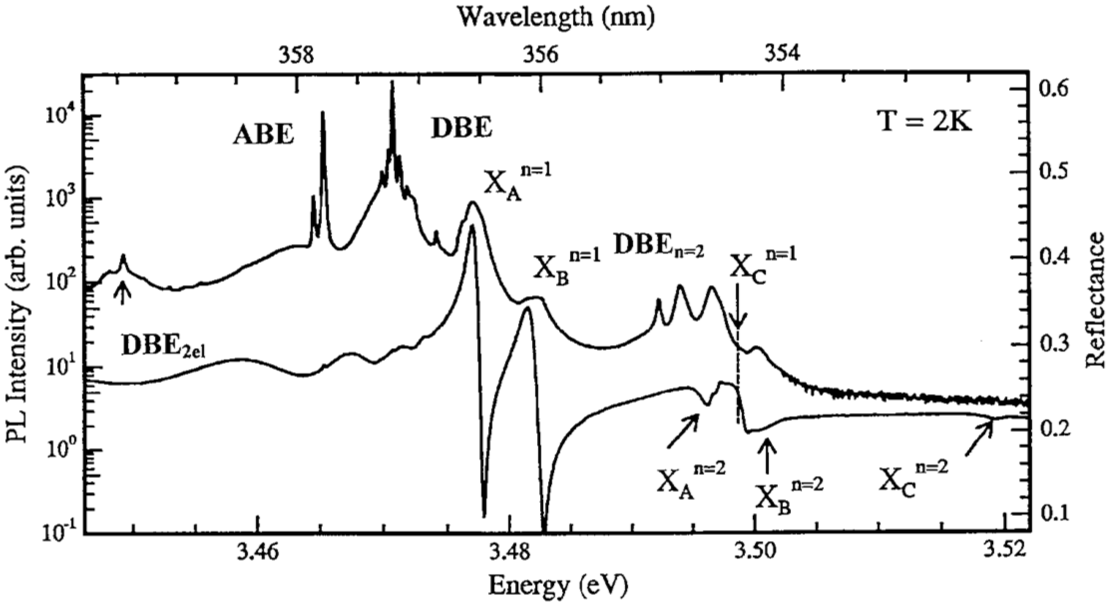

FIG. 5.7. Low-temperature PL and reflectivity spectra of the homoepitaxial GaN layer in the band-edge region, in a wider spectral range. The resolution is 0.12 meV. In addition to the intrinsic exciton peaks and the BE peaks, excited DBE states related to the *n* = 2 free excitons are observed close to 3.494 eV. A DBE related to the B free exciton is seen at about 3.475 eV, and a two-electron replica related to the principal DBE at 3.471 Ev is observed at about 3.450 eV [13].

5.5 Optimizated Lateral PEC Etching for Ultra-Smooth GaN Membranes

Nitrides microcavites need very smooth surfaces to keep their cavity mode as sharp as possible, in order to acquire large Rabi splittings and high Q-factors. Any roughness introduced in any step of the fabrication process flow broadens the cavity mode, reducing that way the possibility of showing a polariton emission.

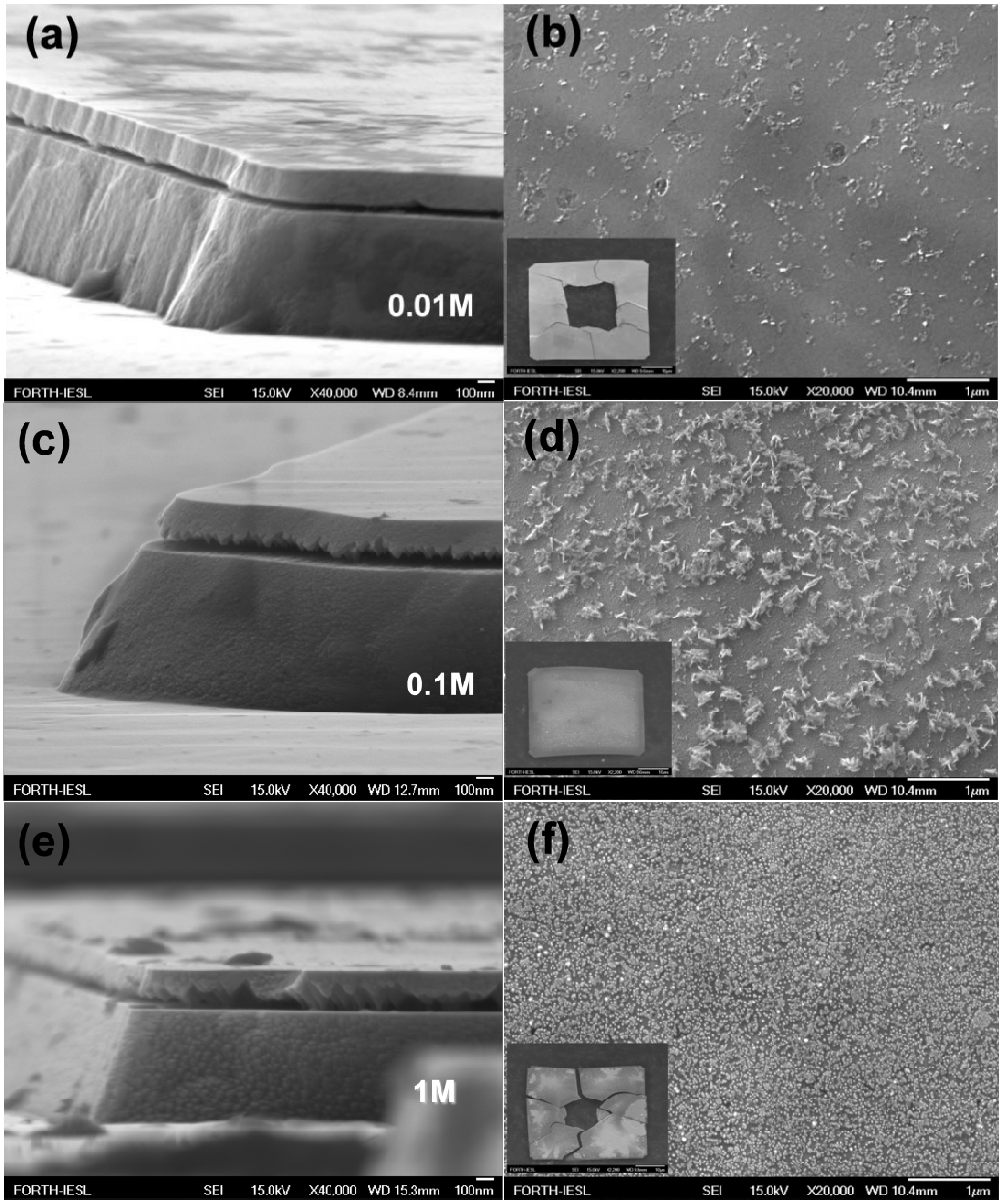

FIG. 5.8. (a), (c), (e), SEM images of undercuts achieved after the removal of the $In_{0.1}Ga_{0.9}N$ sacrificial layer at the specified KOH concentrations, and (b), (d), (f), zoomed-in SEM images of the corresponding N-face surfaces revealed after etching. The insets show zoomed-out images of the complete membranes after transfer on carbon tape. In cases where the etch process is incomplete the membrane cracks during the transfer process revealing the edges of the etch front (b),(f), from which the etch rates can be readily extracted as shown in Fig. 5.12.

For that reason, a study of optimization of the lateral PEC process for yielding smooth surfaces is necessary. In Fig. 5.8 several scanning electron microscopy (SEM) images after the PEC etch are shown corresponding to electrolyte KOH concentrations of 0.01M, 0.1M, 1M under constant bias and etch time of 1hour ((b),(d) insets) and 15min in (f). Following the etching, the membranes are transferred onto a carbon tape and the quality of the underlying N-face GaN surface is carefully examined by SEM and atomic force microscopy (AFM). As seen in Figs. 5.8(b),(d),(f) and Figs.5.9(a),(b),(c) the bottom N-face GaN membrane surface exhibits etch byproducts which decrease in density with decreasing KOH concentration. At lowest concentration, the surface is nearly free of byproducts (independently confirmed by electron diffraction X-ray emission), as shown in Fig. 5.8(b) and Fig. 5.9(a), producing optically smooth etched surfaces of ~6nm rms roughness.

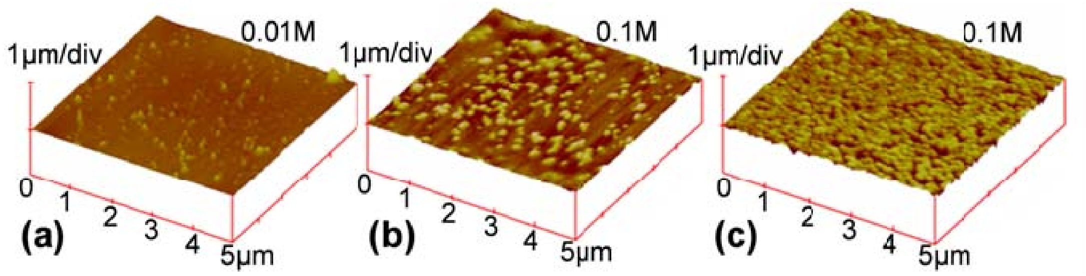

FIG. 5.9. AFM images of N-face membrane surface following lateral PEC etching with KOH concentrations of 0.01M (a), 0.1M (b) and 1M (c).

Using a top view image of a non-fully etched mesa as this depicted in Figure 5.10 we evaluate the average lateral etching rate R_L.

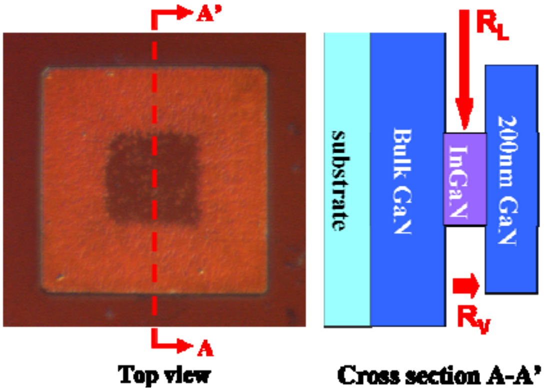

FIG.5.10. a) Image of a membrane (not fully free standing) from an optical microscope. b) schematic of the cross section of the mesa during lateral PEC etching.

This image clearly shows the existence of a residual square $In_{0.1}Ga_{0.9}N$ layer in the center of the mesa, which acts as a post of the overlaying GaN membrane. The vertical etching rate R_V is evaluated by using the cross section of this image. Additionally, the square shape of the remaining $In_{0.1}Ga_{0.9}N$ post layer depicted in Figure 5.10, suggests that the lateral PEC etching of InGaN has no preference in any direction.

The dependence of calculated etching rates and surface roughness on KOH concentration, extracted from SEM and AFM images, are presented in the histograms of Figure 5.11.

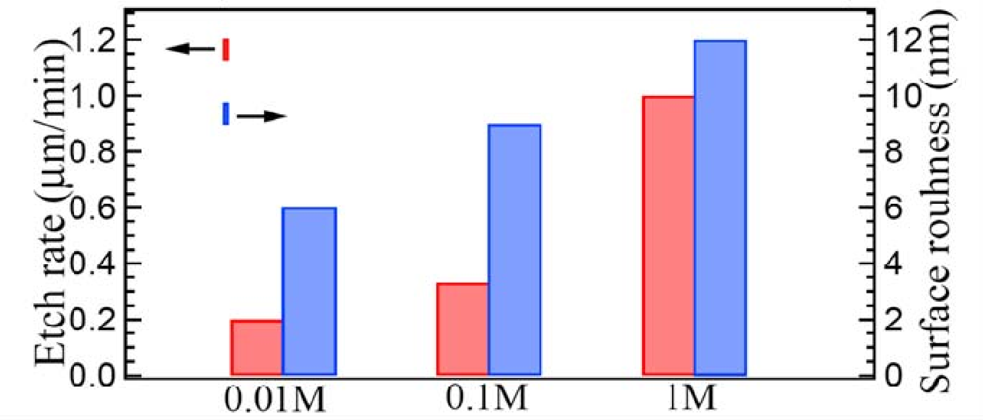

FIG. 5.11. Histogram of etch rate (red) and rms surface roughness (blue) for the specified concentrations, showing clear correlation between etch rate and surface quality.

Clear correlation between the surface quality and KOH concentration is found showing that fine interplay between etching rate and selectivity is required for the optimization of the etched surface quality, which is improved at low KOH concentrations. The above results are remarkable since they suggest that by carefully tuning the etching conditions it is possible to achieve bandgap dependent etching selectivity better than 1:2000 in the InGaN/GaN material system. The relatively low KOH electrolyte concentrations in combination with the high optical power and spectrally narrow excitation source of this study enhance the bandgap selective nature of the lateral PEC etching process and are crucial for our findings.

Increased roughness of the etched surface and cone-shaped morphology is obtained with increasing KOH concentration, in agreement with previous results using broadband excitation and similar electrolyte concentrations. Notably, for high KOH concentrations the N-face of GaN appears chemically unstable yielding cone shaped surface, depicted in Figure 5.12.

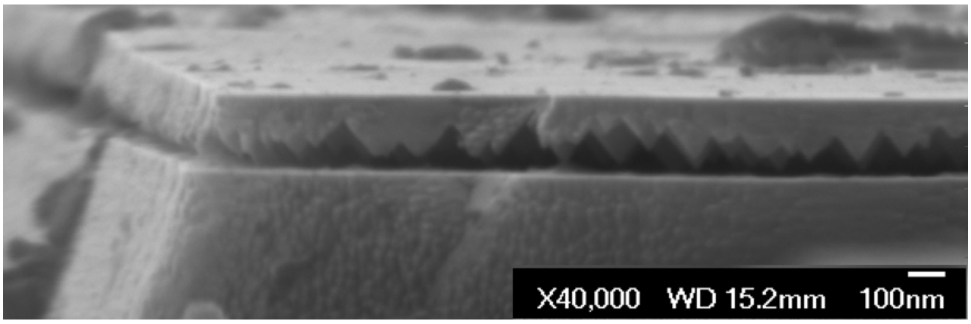

FIG.5.12. SEM image of the characteristic inversed pyramids derived from PEC lateral etching in a high (1M) KOH concentration electrolyte.

This inversed pyramid formation fades out as the etching process evolves towards the centre of the mesa, as seen in Figure 5.13. Instead of the pyramids, we observe the etching byproducts, which correspond to thread dislocation sites, preserving a relatively small roughness across the membrane N-face polarity surface.

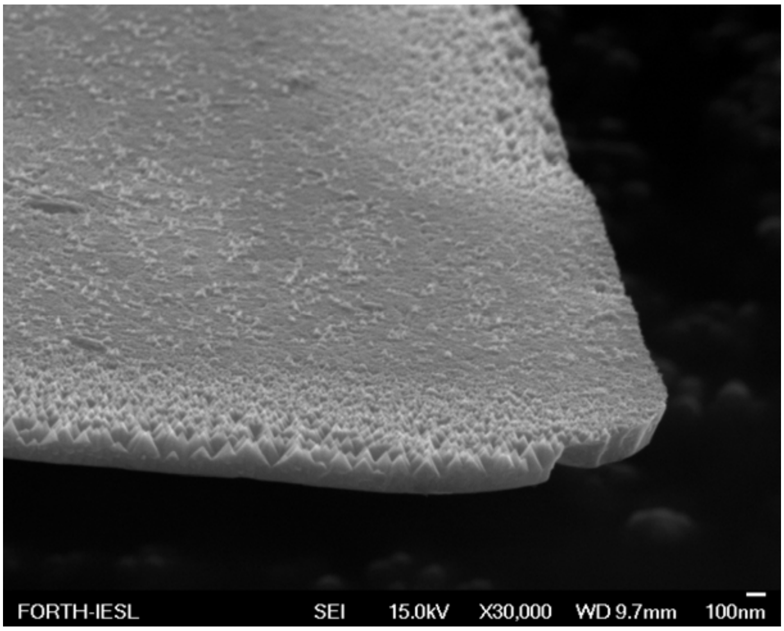

FIG.5.13. SEM image of N-face polarity GaN membrane surface after lateral PEC etching in a high KOH concentrated solution of 1M.

5.6 Interfacial Preference of Bandgap Selective PEC etching

The following SEM images of Figure 5.14 reveal another characteristic of the resonantly enhanced bandgap selective etching of nitrides. It is its interfacial preference. In Figure 5.14 we compare two lateral PEC etching experiments on the same sample which differ only in the illumination power density. We use a thick electrolyte of 1M KOH. This high KOH concentration begins a pure electrochemical (not PEC) etching of the exposed to the electrolyte facets of GaN and InGaN layers, which exhibit a mixture of Ga and N-face polarities [14]. As already mentioned, N-face nitrides are sensitive to all kinds of alkali and acid solutions [15]. This is why the facet of the mesa in Figure 5.14(a) shows an increased roughness after two and a half hours of etching. However, we can also see in this picture that even though there is very little lateral etching due to the low illumination power density of 38mW/cm^2, an evidence of interfacial preference of the bandgap selective PEC etching occurs. It appears that the upper interface of $In_{0.1}Ga_{0.9}N$/ 200nm GaN concentrates higher hole population and thus is etched at higher rate.

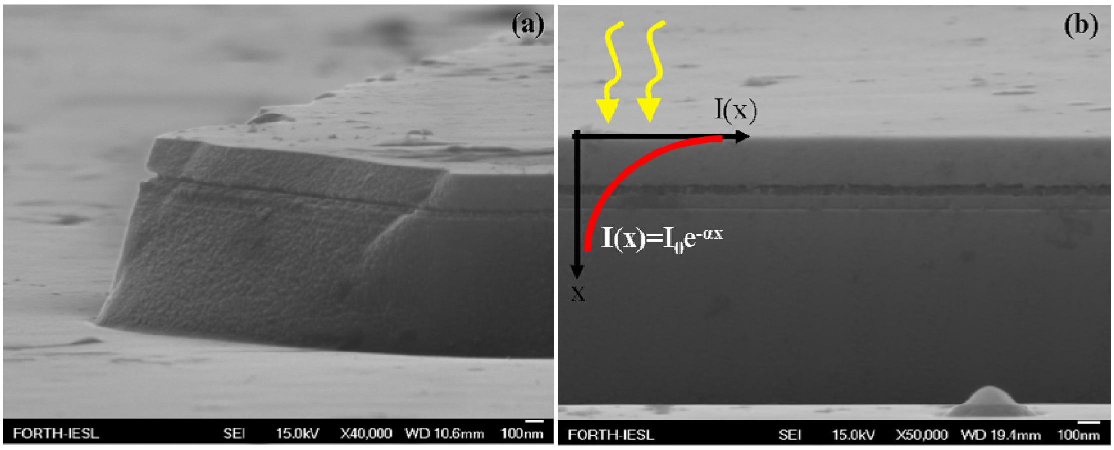

FIG.5.14. (a) and (b)SEM images of the attacked top and bottom GaN/ $In_{0.1}Ga_{0.9}N$ interfaces during resonantly enhanced lateral PEC wet etching.

This interfacial preference of only the photoelectrochemical (PEC) etching is becoming much stronger when we illuminate the sample with a much higher power density of 1.78W/cm^2, as shown in Figure 5.14(b), which suppresses the pyramid formation, even at high KOH concentration.

The existence of the two dimensional electron gas (2DEG) and respectively hole gas (2DHG), very close to the $In_{0.1}Ga_{0.9}N$/GaN interface, may be the explanation of the interfacial preference of the bandgap selective etching. Holes which play an important role in the PEC etching according to the chemical reaction described by Eq. CE.4.1 of the previous chapter are gathered on the $In_{0.1}Ga_{0.9}N$ side of the $In_{0.1}Ga_{0.9}N$/GaN interface. There is also a slightly bigger preference of PEC etching of the upper $In_{0.1}Ga_{0.9}N$/GaN interface, due to the fact that it experiences a greater illumination intensity compared to the same interface 50nm below.

The following SEM image, Figure 5.15, evidences this strong interfacial preference of resonantly enhanced PEC etching, in which one can see $In_{0.1}Ga_{0.9}N$ sheets being extruded from the mesa facets. Top and bottom $In_{0.1}Ga_{0.9}N$/GaN interfaces are fully etched, while intact $In_{0.1}Ga_{0.9}N$ thin sheets are removed.

FIG.5.15. SEM image of extruded InGaN sacrificial layer sheets from the mesa facets.

5.7 Evidence of Strain Relaxation

It is well known that strain strongly modifies band structure of wurtzite GaN [16]. Both the band gap and the splitting of the valence band are changed. For example in case of compressive strain the splitting between the *A*, *B*, and *C* bands increases. Thus, there is an equivalent strong dependence of excitonic transitions on strain. Such dependence is expressed in Figure 5.6, where the photoluminescence peak of the GaN membranes redshifts, confirming their fully relaxed state.

This claim is reinforced by the following SEM image of Figure 5.16, showing a bending part of such a membrane. The existence of compressive stress in the as grown GaN membrane before etching is confirmed by reversing the patterning of the sample into a two dimensional grid instead of regularly spaced mesas, as described in the previous chapter. Since the separated film is still attached on a macroscopic grid the existing strain in the structure is expected to showup as bending, clearly seen in Figure 5.16.

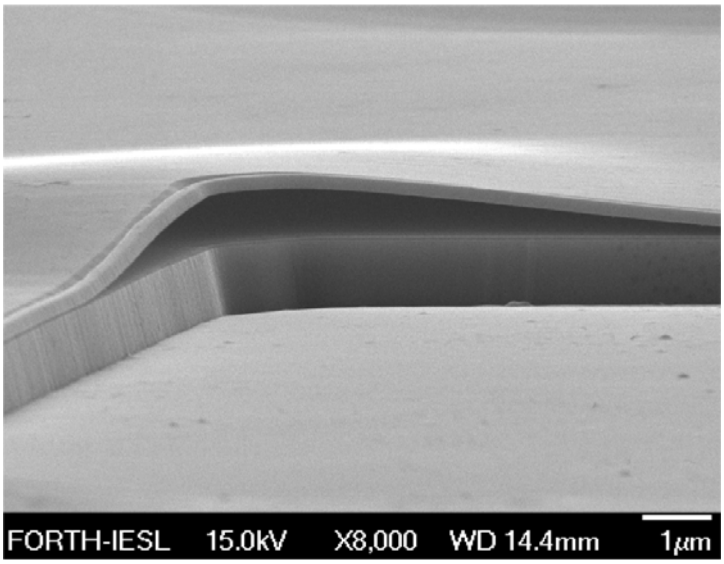

FIG.5.16. SEM image of a partially relaxed 200nm GaN membrane anchored on the macroscopic scale grid after PEC etching in a 1M KOH solution.

Notably, it appears that the interfacial preference of PEC etching, described in paragraph 5.6, may be enhanced if it is combined with the residual stresses derived from the macroscopic grid, resulting in smoother N-face polarity GaN surfaces.

5.8 Interfacial InGaN/GaN Etching in the Absence of Illumination

The interface preference of nitrides etching is not only met in its lateral version but also in the vertical one. More precisely, sample 4 of Chapter 4, which is a 50nm $In_{0.1}Ga_{0.9}N$ layer grown on an un-intentionally doped, 3μm c-plane GaN template, is patterned with a 100nm Ti grid, leaving squares of exposed to electrolyte and light $In_{0.1}Ga_{0.9}N$ surfaces. The Indium Ohmic contact was done on the Ti grid and the semiconductor. After an hour of $In_{0.1}Ga_{0.9}N$ etching in "diffusion limited" conditions we observe strong separation of the top $In_{0.1}Ga_{0.9}N$ layer from the rest of the sample in non-illuminated Ti patterned areas around the non masked squares of the lithographic pattern. In some cases (see Fig. 5.17), the Titanium has not been moved away, remaining still on top of the $In_{0.1}Ga_{0.9}N$ layer protecting it from photo-etching, and in others it is etched, leaving a free-standing $In_{0.1}Ga_{0.9}N$ membrane, as shown in Figure 5.14).

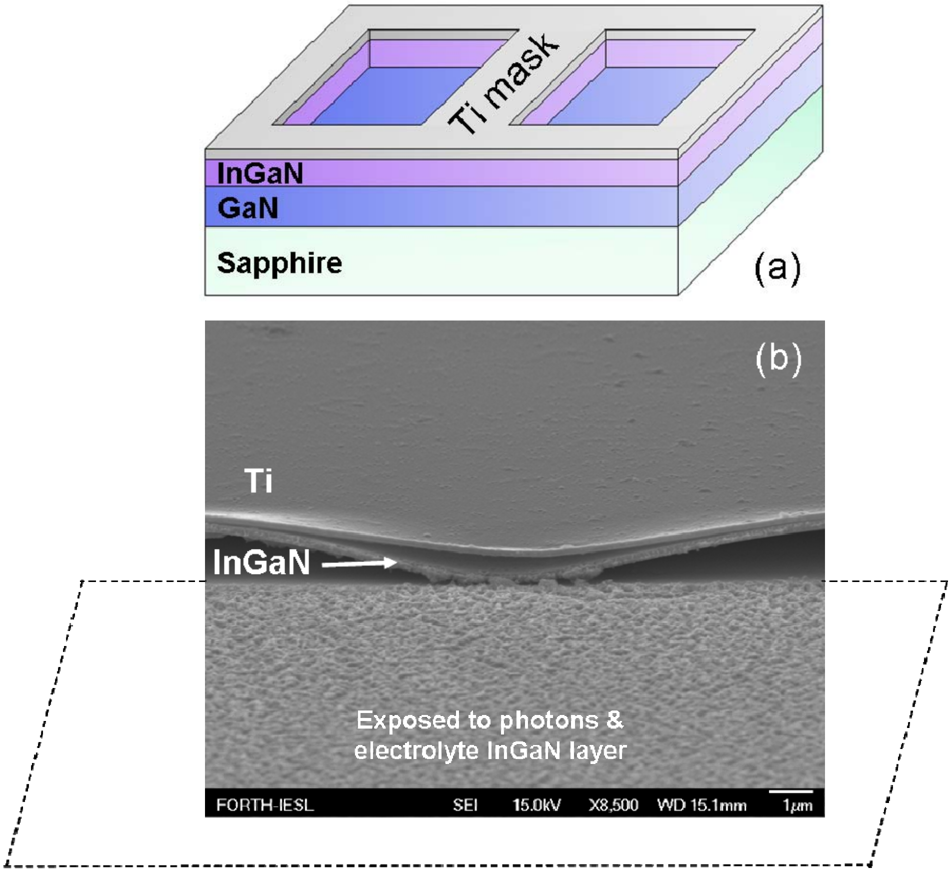

FIG. 5.17. a) Schematic and b) SEM image of the etched non-illuminated $In_{0.1}Ga_{0.9}N$ areas, bended due to their anchoring to the macroscopic $In_{0.1}Ga_{0.9}N$ grid. Ti pattern still remains on top of the detached $In_{0.1}Ga_{0.9}N$ parts.

There are two findings that have come up after the mask bias during this PEC etching experiment. The first is the degradation of the exposed $In_{0.1}Ga_{0.9}N$ layer into a porous surface, full of etch pits, without showing any thinning attributed to etching.

The second are the free standing non-illluminated In$_{0.1}$Ga$_{0.9}$N membranes showing an extremely smooth N-face surface roughness, probably of better optical quality than the GaN membranes yielded using the resonantly enhanced lateral PEC etching technique, as depicted in Figure 5.19.

This separation of the In$_{0.1}$Ga$_{0.9}$N layer, without any evidence of photo-etching, since Ti mask blocks its excitation, might be explained as following. The In contact we use applies to both sample and mask simultaneously. If the bias is only applied to the Ti mask, the nitride sample is excluded from the circuit of the etching, however, under these conditions it is not. This suggests that large part of the applied voltage is “consumed” mostly across the Ti-grid.

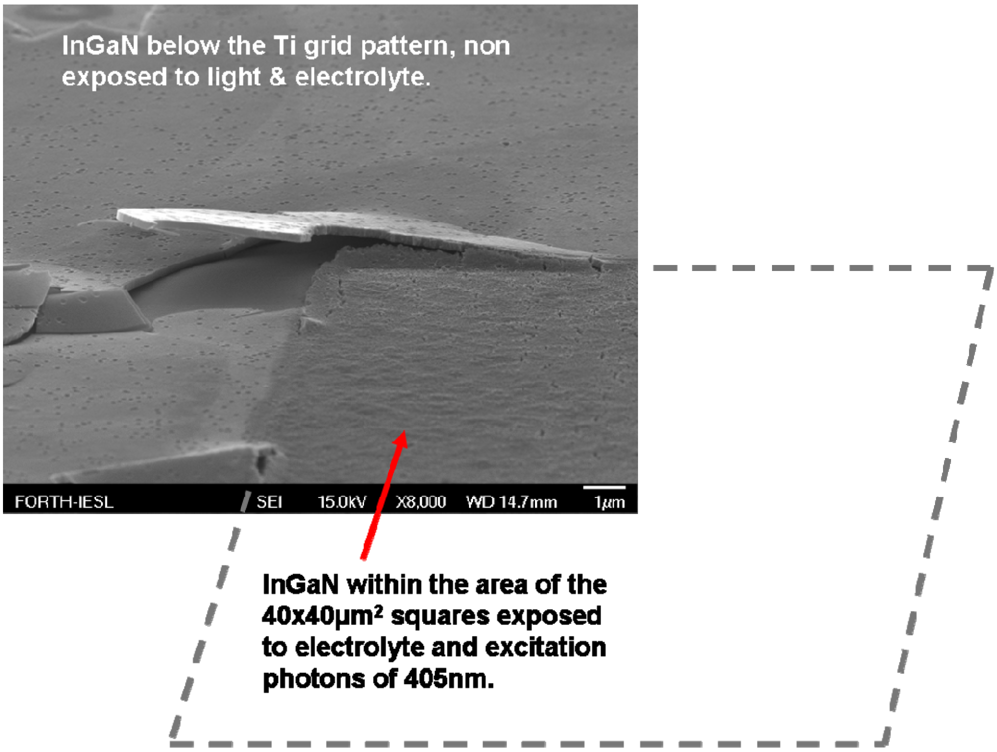

FIG.5.18. SEM image of the In$_{0.1}$Ga$_{0.9}$N etched non-illuminated In$_{0.1}$Ga$_{0.9}$N areas having the above Ti pattern completely etched.

This drainage of electrons through the Ti grid may increase the 2DEG and thus the 2DHG at the In$_{0.1}$Ga$_{0.9}$N/GaN interface, resulting into an enhanced lateral-interfacial etching, yielding the smooth N-face polarity In$_{0.1}$Ga$_{0.9}$N surface, depicted in figure 5.19. Further experiments should be done, also on GaN/AlGaN heterostructures, to investigate the claims above, towards a new fabrication scheme for all dielectric GaN microcavities.

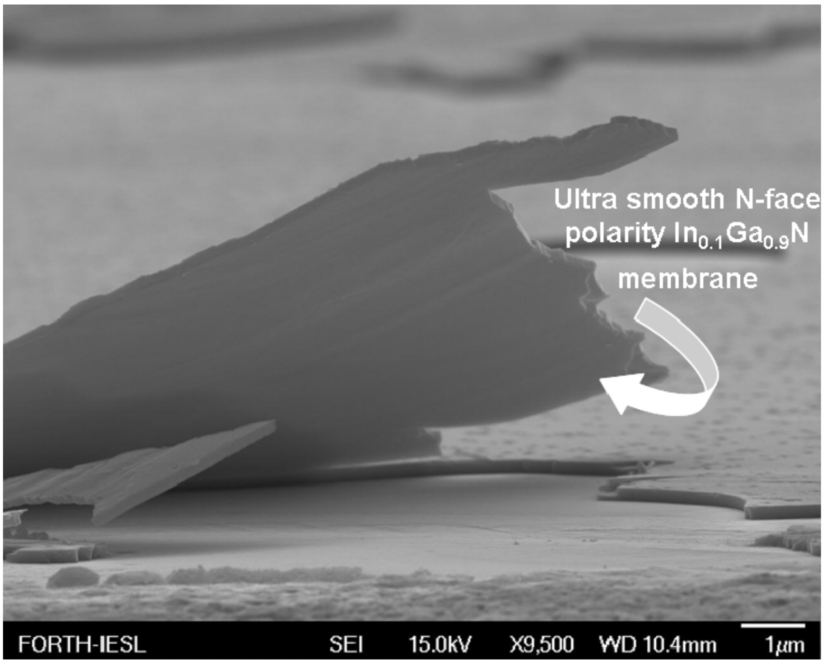

FIG.5.19. SEM image of an upward bending free standing 50nm $In_{0.1}Ga_{0.9}N$ membrane. This bending reveals the smoothness of the N-face polarity of the membrane, acquired bia biasing both the semiconductor and its Ti mask.

5.10 Conclusions

In conclusion, we show that by careful optimization of the photoelectrochemical etching conditions it is possible to induce high selectivity lateral etching of buried InGaN layers in a GaN matrix. Using this bandgap selective lateral etching technique, ultrathin freestanding GaN membranes can be fabricated, having an etched surface of optical quality and showing no degradation of their optical properties. The quality of the etched surface is found to improve at low electrolyte concentrations and high excitation power densities, suggesting high etching rates for the removal of etch byproducts. Convenient manipulation and transfer of the membranes open new opportunities for further processing of such membranes in optoelectronic devices, and in particular for the fabrication of all-dielectric strongly coupled GaN microcavities.

References

[1] E. Trichas, M. Kayambaki, E. Iliopoulos, N. T. Pelekanos, and P. G. Savvidis, “Resonantly enhanced selective photochemical etching of GaN,” *Applied Physics Letters*, vol. 94, no. 17, p. 173505, 2009.

[2] E. Trichas et al., “Selective photochemical etching of GaN films and laser lift-off for microcavity fabrication,” *physica status solidi (a)*, vol. 205, no. 11, pp. 2509-2512, 2008.

[3] E. D. Haberer et al., “Free-standing, optically pumped, GaN/InGaN microdisk lasers fabricated by photoelectrochemical etching,” *Applied Physics Letters*, vol. 85, no. 22, p. 5179, 2004.

[4] C. Meier et al., “Visible resonant modes in GaN-based photonic crystal membrane cavities,” *Applied Physics Letters*, vol. 88, no. 3, p. 031111, 2006.

[5] R. P. Strittmatter, R. A. Beach, and T. C. McGill, “Fabrication of GaN suspended microstructures,” *Applied Physics Letters*, vol. 78, no. 21, p. 3226, 2001.

[6] J. Kim, D. Kim, J. Lee, H. Jeon, Y. Park, and Y. Choi, “AlGaN membrane grating reflector,” *Applied Physics Letters*, vol. 95, no. 2, p. 021102, 2009.

[7] Y. Gao, I. Ben-Yaacov, U. K. Mishra, and E. L. Hu, “Optimization of AlGaN/GaN current aperture vertical electron transistor (CAVET) fabricated by photoelectrochemical wet etching,” *Journal of Applied Physics*, vol. 96, no. 11, p. 6925, 2004.

[8] A. R. Stonas et al., “Backside-illuminated photoelectrochemical etching for the fabrication of deeply undercut GaN structures,” *Applied Physics Letters*, vol. 77, no. 16, p. 2610, 2000.

[9] A. R. Stonas, T. Margalith, S. P. DenBaars, L. A. Coldren, and E. L. Hu, “Development of selective lateral photoelectrochemical etching of InGaN/GaN for lift-off applications,” *Applied Physics Letters*, vol. 78, no. 13, p. 1945, 2001.

[10] C. Youtsey, G. Bulman, and I. Adesida, “Dopant-selective photoenhanced wet etching of GaN,” *Journal of Electronic Materials*, vol. 27, no. 4, pp. 282-287, 1998.

[11] R. Sharma, E. D. Haberer, C. Meier, E. L. Hu, and S. Nakamura, “Vertically oriented GaN-based air-gap distributed Bragg reflector structure fabricated using band-gap-selective photoelectrochemical etching,” *Applied Physics Letters*, vol. 87, no. 5, p. 051107, 2005.

[12] D. Gogova et al., “Characterization of High-Quality Free-Standing GaN Grown by HVPE,” *Physica Scripta*, vol. 114, pp. 18-21, 2004.

[13] K. Kornitzer et al., “Photoluminescence and reflectance spectroscopy of excitonic transitions in high-quality homoepitaxial GaN films,” *Physical Review B*, vol. 60, no. 3, p. 1471, Jul. 1999.

[14] Y. Gao, M. D. Craven, J. S. Speck, S. P. Den Baars, and E. L. Hu, “Dislocation- and crystallographic-dependent photoelectrochemical wet etching of gallium nitride,” *Applied Physics Letters*, vol. 84, no. 17, p. 3322, 2004.

[15] H. M. Ng, W. Parz, N. G. Weimann, and A. Chowdhury, “Patterning GaN Microstructures by Polarity-Selective Chemical Etching,” *Japanese Journal of Applied Physics*, vol. 42, no. 2, pp. L1405-L1407, 2003.

[16] S. C. Jain, M. Willander, J. Narayan, and R. V. Overstraeten, “III–nitrides: Growth, characterization, and properties,” *Journal of Applied Physics*, vol. 87, no. 3, p. 965, 2000.

Chapter 6: Fabrication of All dielectric GaN Microcavities

6.1 Proposed Schemes for All-Dielectric GaN Microcavity Fabrication

After the optimization of the etching method, able to yield GaN membranes of ultra-smooth N-face polarity surface roughness, we have made resonantly enhanced lateral PEC etching an important and effective tool of the proposed fabrication process, presented in Chapter 3. It solves a fundamental problem of the processing, which is the isolation of free-standing GaN membranes, which can easily be incorporated in an all dielectric optical cavity. Figure 6.1 shows two different variations of the initially proposed fabrication scheme of Chapter 3. They both incorporate a sample growth similar to that shown in Figure 5.2(a) of the previous Chapter.

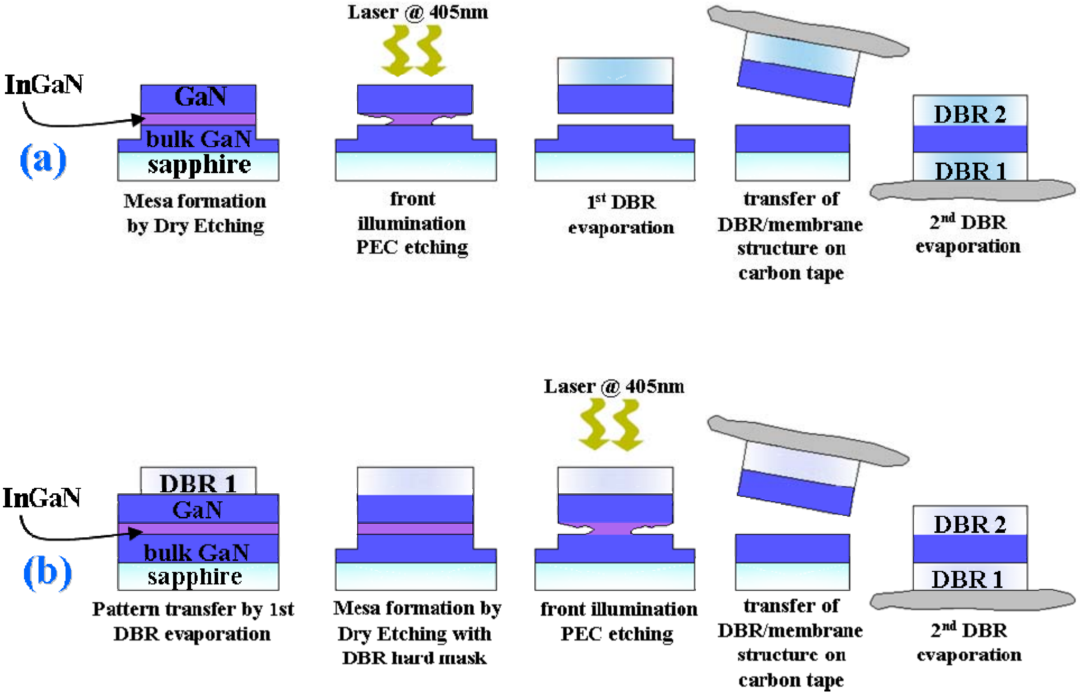

FIG. 6.1. a) Schematic of the process flow, towards the all dielectric GaN microcavity structure and b) its variation using the first DBR as a hard mask for mesa formation.

Scheme (a) begins with the fabrication of mesas using a lithographic method for pattern transfer and a following reactive ion dry etching step. This mesa formation exposes the facets of the $In_{0.1}Ga_{0.9}N$ sacrificial layer, which after that step is ready to be laterally etched.

By exciting the $In_{0.1}Ga_{0.9}N$ layer with a light from a laser source at 405nm (above its bandgap) we fully laterally etch it untill a free standing 200nm GaN membrane is created. After this particular step of the process flow, a large number of free standing membranes across the sample surface is fabricated. Before we lift them off with a common scanning electron microscope (SEM) carbon tape, we evaporate on the sample the first dielectric mirror of the microcavtiy. A key element of this scheme is the height of the mesa after the dry etching. It must be higher than the whole stack of the dielectric layers which form the DBR, so the resulting pairs DBR/GaN membrane can be easily detached from the sample.

The second scheme starts with a lithographic step and a following evaporation of the first dielctric DBR. Lift-ff process creates a pattern of dielectric squares on the as grown MBE sample. This DBR is used as a hard mask for reactive ion etching (RIE) to fabricate the desired mesas. This way, the Ga-face surface of the upper GaN layer remains protected and clean as possible by any residuals of the PEC etching. Additionally, the hard dielectric DBR protects the membranes from their exciton degradation after the dry etching [1]. This is an advantage of the second process scheme over the first one. After the lateral PEC etching of the sacrificial layer the pair of the first DBR/GaN membrane is lifted off with an SEM carbon tape. This new carbon tape is turned up side down, ready for the second DBR evaporation, completing the all dielectric microcavity structure.

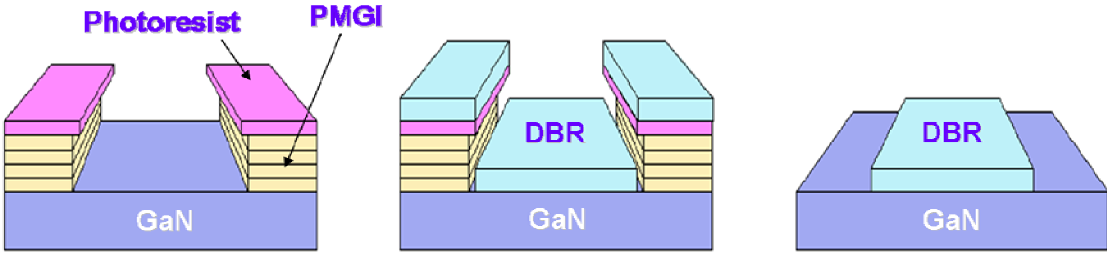

FIG. 6.2. Processing scheme, designed for easy DBR lift-off, using the PMGI undercut technique.

This process scheme faces a technical difficulty which had to be solved. The difficulty is associated with the lift-off of the first DBR after the lithographic step. Thus, we have developed a technique for the creation of an enhanced undercut of the photoresist pattern, to establish a wide path for the acetone and manage lift off of the dielectrics on top of the photoresist resin.

This technique is based on the technology of the polydimethylglutarimide (PMGI) photoresists and is combined with a common AZ5214 photoresist resin for a pattern transfer process. Four layers of this PMGI resin are spin coated on the sample and soft baked at 160ºC (see Fig. 6.2). On top of that stack of coating polymer layers, a film of AZ5214 photoresist is also spinned. Then, using a standard lithographic procedure we imprinted a pattern of the photoresist, which then was transferred to the stack of the four PMGI layers with a slight increase of the pattern dimensions, resulting in an undercut formation below the photoresist.

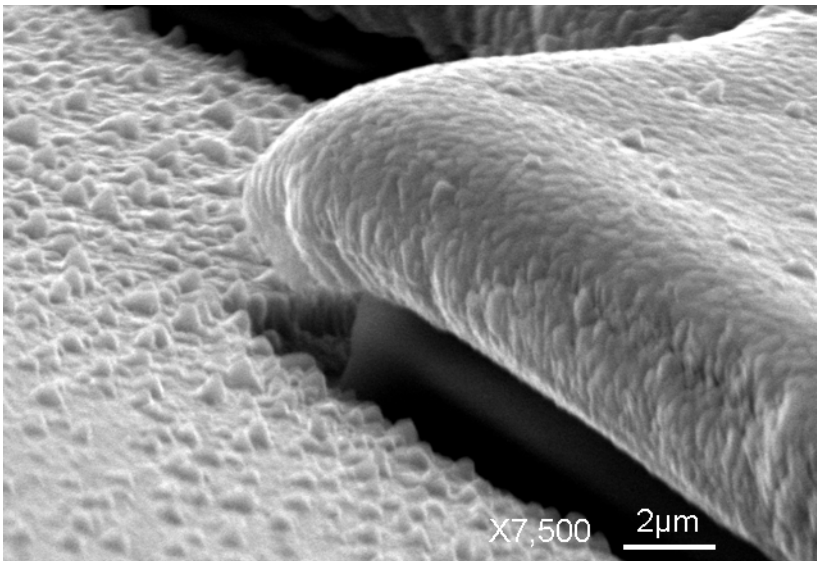

FIG. 6.3. SEM image of the undercut created with the PMGI technique, on test samples evaporated with Ti.

Another critical element of this process we had to take care of, was the fact that the dielectric evaporation process requires a continuous heat of the sample at 100ºC. This annealing introduces a possible resist reflow, which can deform the lithographic pattern and thus, create a continuous film of dielectrics, preventing us from a successful lift off afterwards. The PMGI resin is famous for its robustness to annealings up to 250ºC, but since this technology has not been previously tested in our laboratory we performed some tests to simulate the dielectrics evaporation process. We spin coated all the required layers of PMGI and AZ5214 photoresist on a sapphire substrate to simulate also the heat dissipation during the annealing. The sample is set into an e-beam evaporator chamber, annealed up to the temperature of 120ºC for three hours. During the annealing, we evaporate Ti metal, which compared to the dielectrics would have a less viscous behaviour at this temperature. The result is shown in Figure 6.3, where one can clearly see the undercut formed below the reflowed photoresist-Ti mixture.

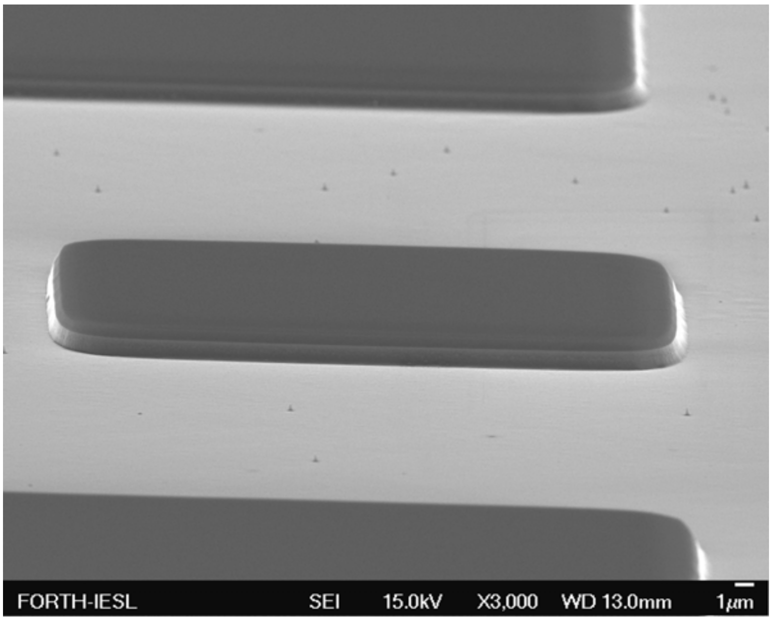

FIG. 6.4. SEM image of the formed mesas after reactive ion etching with the first DBR as a hard mask.

6.2 Fabrication of All-Dielectric GaN Microcavities

After this testing step, we are sure that the dielectrics lift-off process will be successful and as expected, we manage to create a nice pattern of a 10-pair sputtered SiO_2/Ta_2O_5 DBR, which after reactive ion etching yields mesas of 1μm high, as depicted in Figure 6.4. In the following SEM image (see Fig. 6.5), one can also see well defined dielectric layers stack together, forming the first DBR of our all dielectric microcavities.

The top surface of the dielectric mirror appears to be reasonably clean to allow the excitation light pass through, without any scattering and begin the etching of the sacrificial $In_{0.1}Ga_{0.9}N$ layer. At this point we must stress the fact that the first DBR is designed in such a way of providing the maximum possible transmission for the excitation wavelength of 405nm. In case the edge of the DBR stopband is slightly shifted into lower transmission, due to fabrication mistakes, we can shift its stopband edge by simply setting an angle of incidence for the excitation beam of 405nm, as illustrated in Figure 6.5.

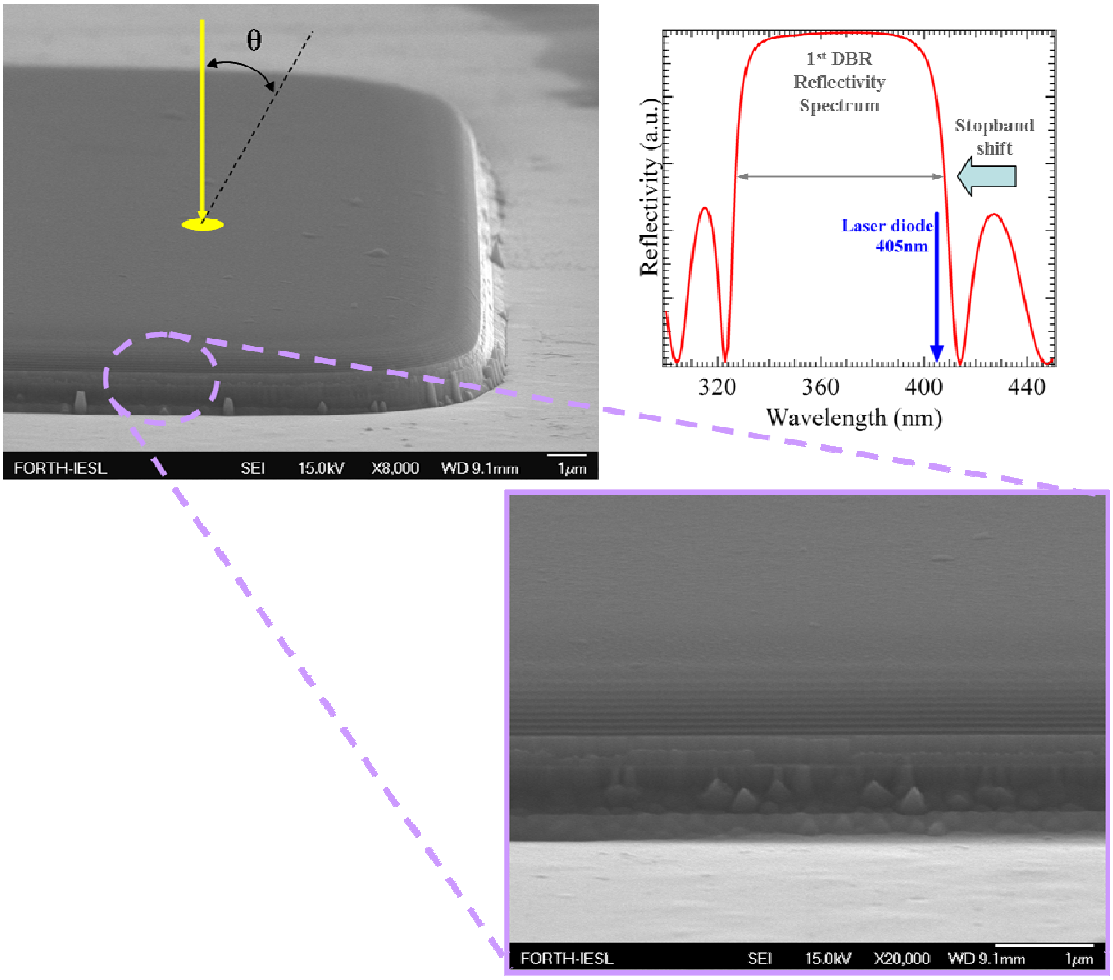

FIG. 6.5. SEM images, side views of the mesas yielded after the dry etching method with the DBR on top and schematic of the DBR stopband shift, to achieve maximum transmission for the 405nm laser excitation souece.

The next step of the lateral photoeletcrochemical etching experiments of the $In_{0.1}Ga_{0.9}N$ layer are not done all under the same conditions. Each experiment is slightly different, by changing mostly the KOH concentration and keeping constant high the excitation power density at ~$1.78 W/cm^2$ and a homogeneously illuminated area of 1mm diameter. This is done in order to investigate strong coupling dependence on the N-face polarity yielded surface roughness.

The resulting free standing pairs of the first DBR and 200nm GaN membrane are depicted in Figure 6.6. What is interesting is the upward bending of the pairs which is due to the DBR compressive stress applied to the membrane below. This bending, even though there is not any chemical bonding between the nitride and the amorphous dielectrics, may possibly induce strain, resulting in membrane PL energy shift. In Figure 6(b) one can also see the good adhesion between the two materials and the quality of the DBR individual layers.

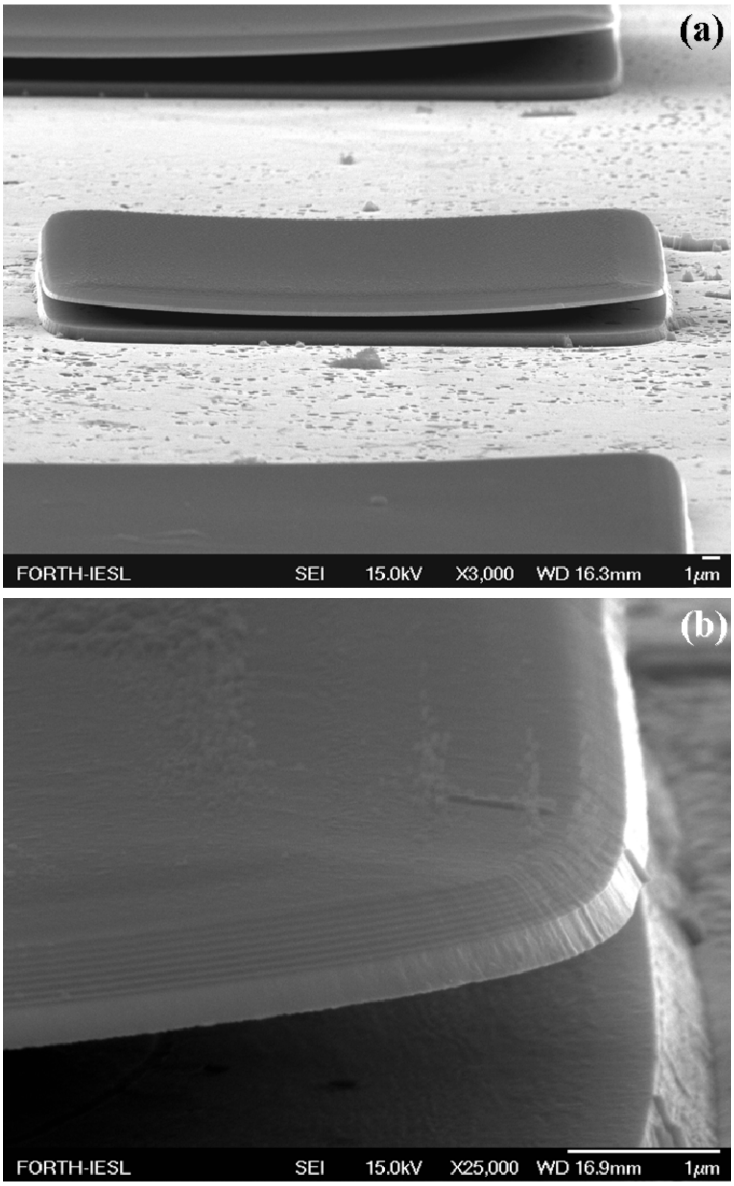

FIG. 6.6. SEM images a) of the free standing GaN membrane/DBR pairs, b) of the edge of such a pair, acquired after lateral PEC etching in a 0.01M KOH solution.

The initial lithographic step was not successful in all parts of the sample we processed, thus we have observed the following two interesting features, depicted in Figure 6.7.

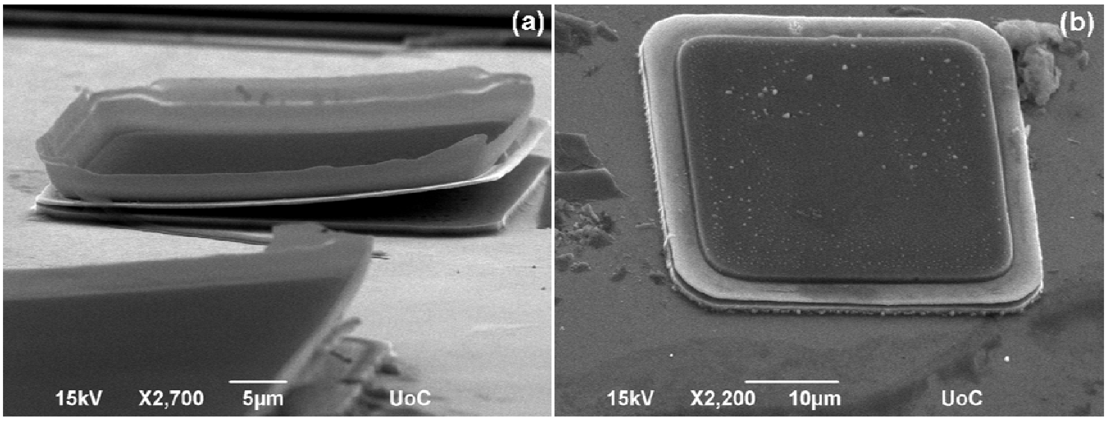

FIG. 6.7. a) SEM images fully under etched GaN membrane/DBR pairs with upward bended DBR residuals after the photoresist/PMGI lift-off. b) These DBR “wings” are broken during PEC etching, resulting into an uncovered of DBR GaN stripe, corresponding to the achieved undercut using the PMGI technique.

They both can be attributed to the reflow of the AZ5214 photoresist, covering the PMGI undercut and creating a cavity among them. Fortunately, the acetone solution managed to fill this cavity and dissolved the PMGI resin, allowing DBR lift-off. As a consequence, part of the reflowed DBR which had covered the sidewalls of the resist/PMGI patterns, became part of the continuous DBR film on top of the semiconductor. Figure 6.7(a) shows free-standing DBR film around the perimeter of each mesa. Some of these free standing films managed to remain attached to main part of the film on top of the mesas after the lateral PEC etching, but some others broke, resulting in an uncovered offset between the GaN membrane and the edge of the DBR on top of it, of about 3μm wide (see Figure 6.7(b)). This unintentionally formed offset was used as a way to clearly distinguish the membrane from the DBR, when side view SEM images of the undercut are taken. In this way, we manage to evaluate the quality of etching and the quality of both membrane and DBR facets after the etching.

After completing this part of the process scheme, we used a common carbon tape to lift-off the DBRs and GaN membrane. We turned these new substrates up-side down and observed, with an SEM the N-polar GaN surfaces, that came up after the lateral PEC etching, to check their quality.

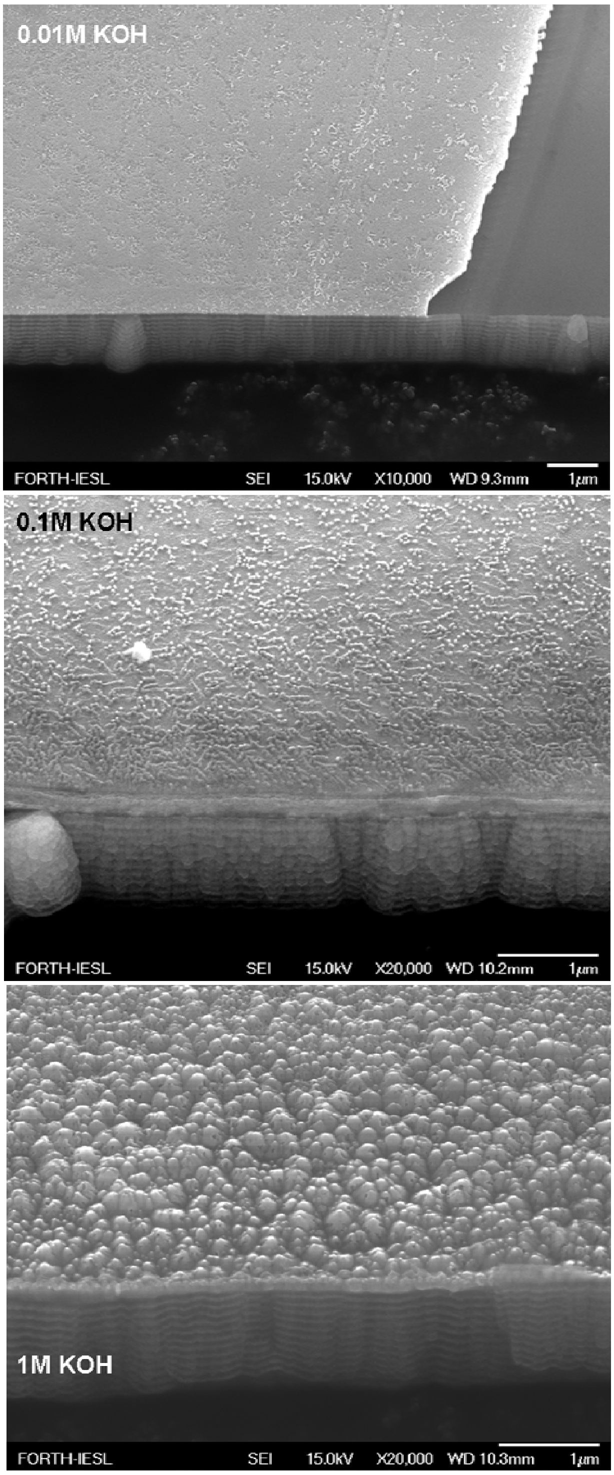

FIG. 6.8. SEM images of the N-face polarity of the GaN membranes after lateral PEC etching in electrolytes of: a) 0.01M, b) 0.1M and c) 1M KOH respectively. Lower roughness was shown for 0.01M KOH.

We observe excellent agreement with our previous results on concentration dependent lateral etching (see Fig. 5.8), as depicted in Figure 6.8. We observe low surface roughness when reduced concentration of 0.01M KOH is used, keeping high excitation intensity. When we use thick KOH electrolyte solutions, we get rougher surfaces, which in the case of 1M KOH concentration, is quit considerable as seen in Figure 6.8(b) and (c), thus it cannot be used for all-dielectric GaN microcavities fabrication.

The final step for both process schemes is the evaporation of the second DBR, to complete the "all dielectric" microcavity structure. SEM images (see Fig. 6.9) are taken after cracking few microcavities with a tweezer, to observe the sample cross-section, since all microcavities had their edges buried under the "blanket" of the second DBR.

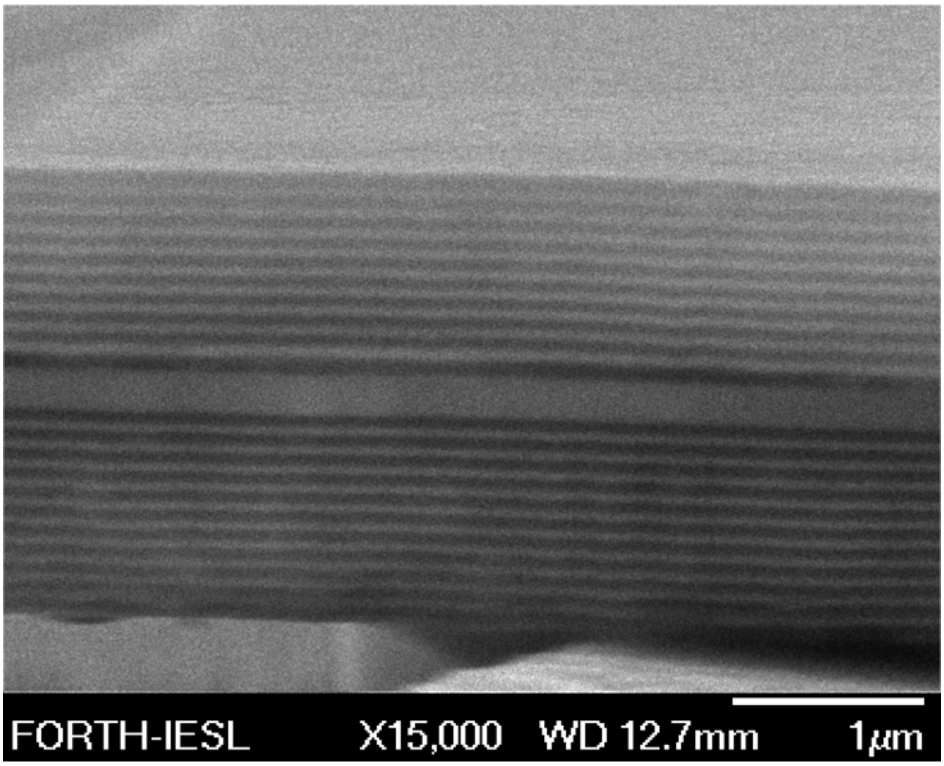

FIG. 6.9.SEM images of cross sections of the all dielectric GaN microcavities fabricated by the resonantly enhanced lateral photoelectrochemical (PEC) etching method.

At this point, we must stress that we have fabricated excellent quality all-dielectric GaN microcavitiess, as depicted in Figure 8.9, which are the "state of the art" of modern nitride-based microcavity technology.

6.3 Optical Characterization

The optical characterization of these novel all dielectric GaN microcavities will verify their high optical quality by showing exciton and photon strong coupling. However, it is important to characterize first the reflectivity of both top and bottom dielectric mirrors, in order to interpret the results of the optical characterization of our microcavities.

We setup an angle resolved white light reflectivity experiment, based on a goniometer, we have designed, in the standard Bragg-Brentano (θ-2θ) geometry, with an extra rotational stage for the sample rotation (angle θ), depicted in Figure 8.10. The second rotational stage, co-centric with the first one, is used for the mounting of the reflectivity collection optics, which couple collected photons, via a 400nm diameter UV-graded optical fiber, to an Ocean Optics spectrometer.

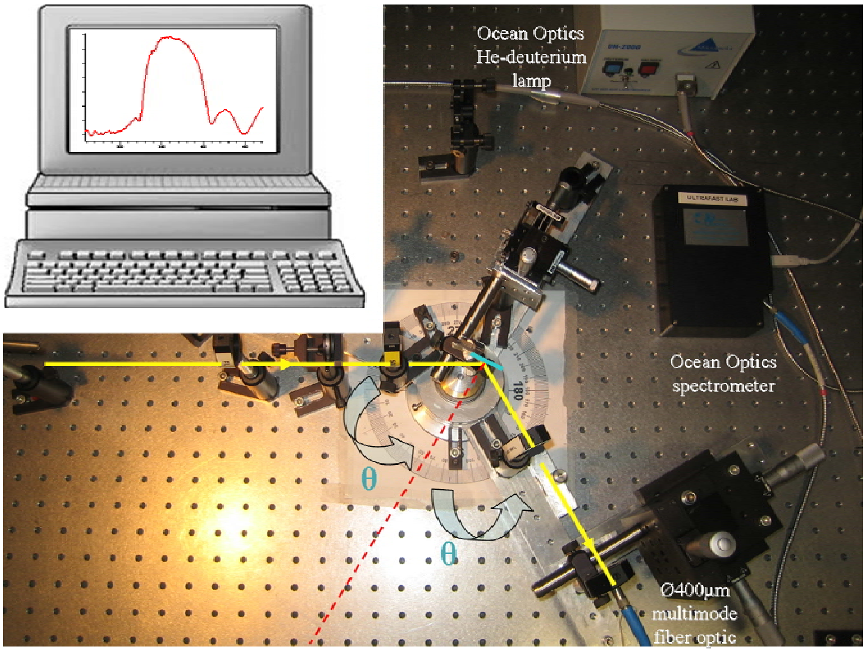

FIG. 6.10. Setup of the angle resolved white light reflectivity of used for the DBRs.

A critical element in this study is the fact that the reflectivity spectra of the two DBRs show a relative difference of ~10nm between their stopbands at normal incidence, as depicted in Figure 6.11, which will be also observed in angle resolved PL spectra.

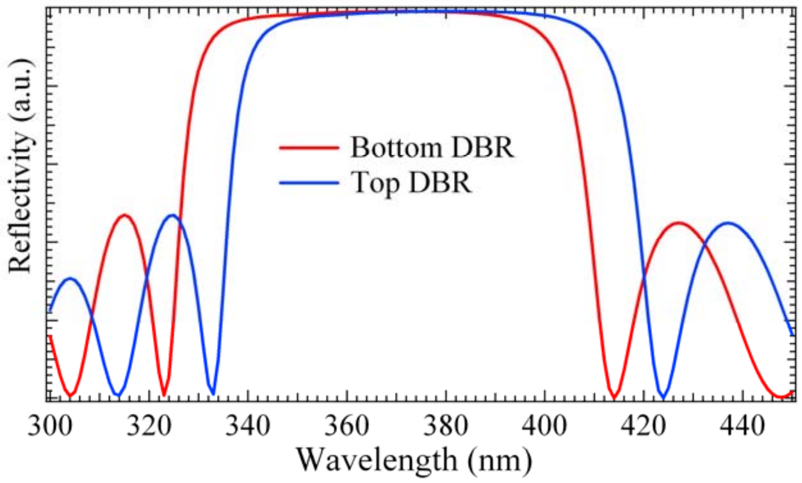

FIG. 6.11. Reflectivity spectra of the top and bottom DBR of the all dielectric GaN microcavities.

Both DBRs show also, as expected from the theory [2], a splitting between the s-wave (TE) and the p-wave (TM). In the case of s-wave the electric field vector **E** is transverse to the plane of incidence and in the case of p-wave the magnetic field vector **H** is perpendicular to the plane of incidence (see Fig. A.1 of Annex). Figure 6.12 shows angle dependence of reflectivity spectra simulations of a 10-pair SiO_2/Ta_2O_5 DBR for s and p polarizations. We observe a sharper TM-Bragg mode compared to the TE-Bragg mode.

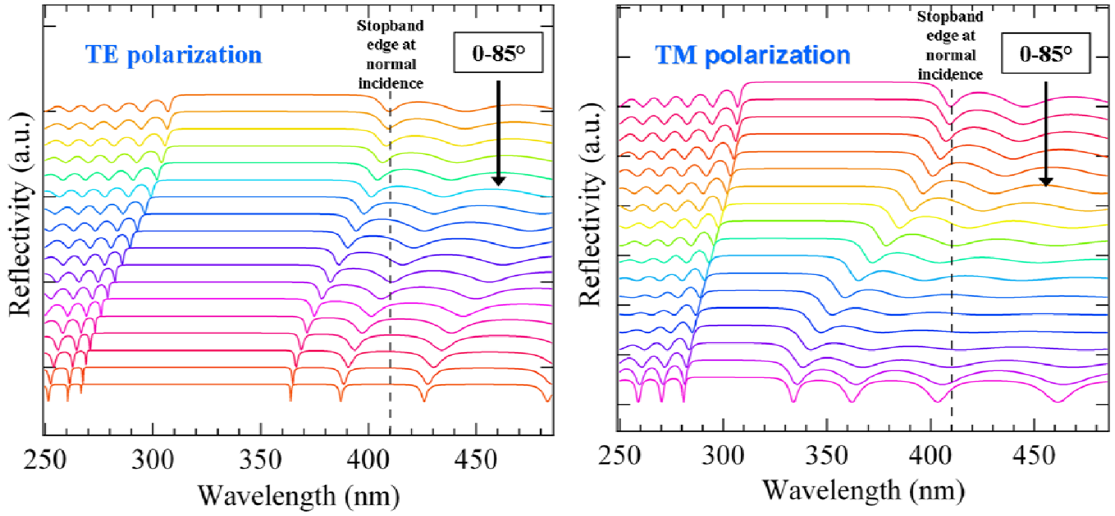

FIG. 6.12. Reflectivity spectra simulation of a 10-pair SiO_2/Ta_2O_5 DBR for TM and TE polarizations.

These two modes are mixed for unpolarized light in reflectivity spectra of a real DBR structure, as seen in Figure 6.13. This figure presents angle resolved white light reflectivity spectra, acquired (see setup of Fig. 6.10) from the second 10-pair DBR of SiO_2/Ta_2O_5, which has a shifted stopband, with its first Bragg mode at 422nm. In this, clearly one can see the splitting between the TM and TE Bragg modes of the mirror. The relative sharpness of the TM mode compared to the TE one, is verified also in Figure 6.13. An equivalent splitting between TM and TE Bragg modes is also observed in the case of the bottom DBR of our microcavites, but slightly blue shifted compared to those of Figure 6.13. Thus, we expect to identify both top and bottom DBR splitting in similar spectra of our real microcavities for the study of their linear properties and dispersion relations.

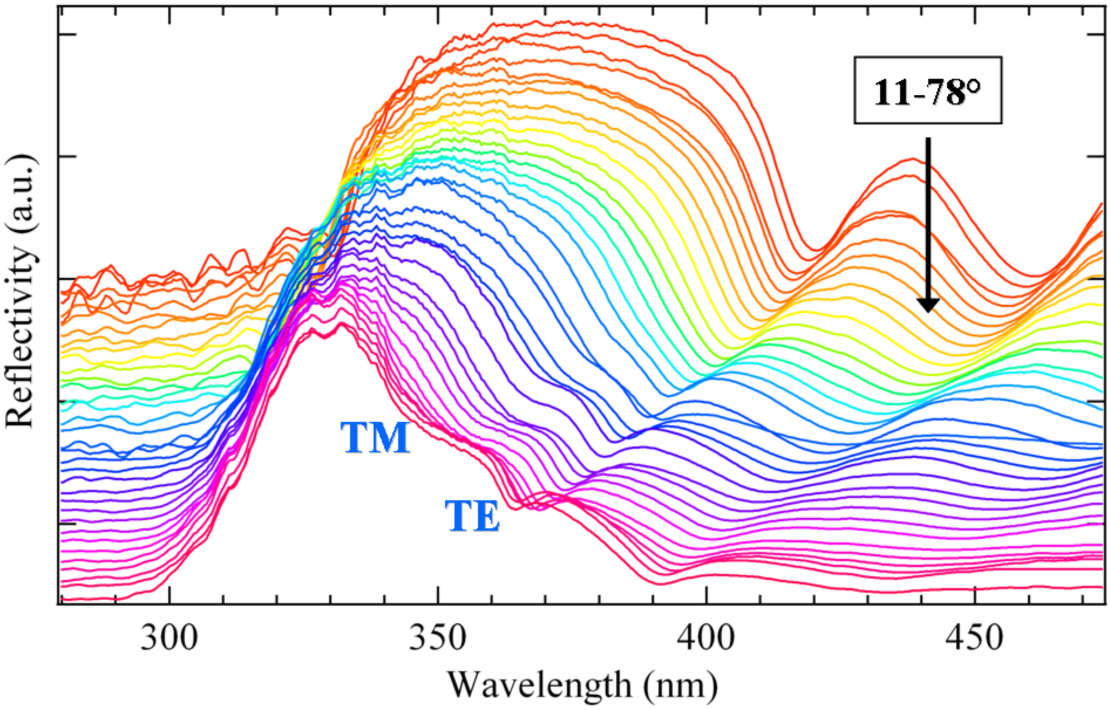

FIG. 6.13. Intentionally spaced, acquired at different angles, reflectivity spectra of the top (second) DBR, used in our all-dielctric microcavities. The s (TE) and p (TM) waves are clearly identified.

Linear properties of the fabricated microcavity structures are studied by collecting photoluminescence spectra with optical fiber at different angles under nonresonant CW excitation of 3μm spot at 325nm, at room temperature, as depicted in Figure 6.14. The laser is focused on a few micrometers spot size on the microcavities, using a very sharp lens of 12mm focal length and 0.54 numerical aperture. The achievement of this micro size spot is crucial in this study, as it will be shown in the following paragraphs, since the smaller fabricated microcavities are 40x40μm^2 squares in size. If we had used a bigger spot size, we would have acquired an averaged response for the whole microcavity surface, neglecting that way: i) small tunings of the cavity mode, due to thickness variations of the GaN active layer across the surface and additionally ii) surface roughness variations of the N-face polarity of the GaN mambranes. Thus, exciting a small smooth surface area, able to show strong coupling is more possible.

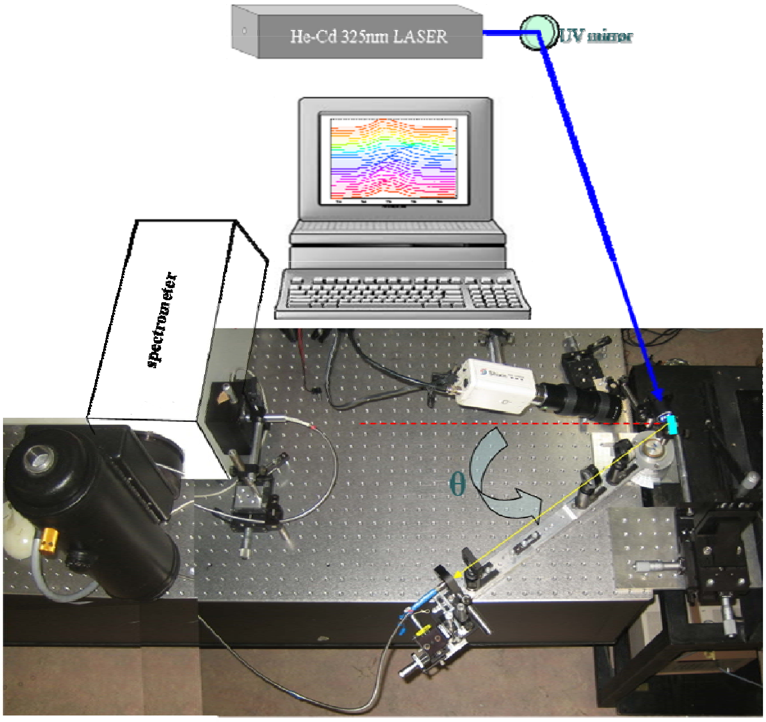

In the

FIG. 6.14. Setup of the angle resolved PL experiment. The angle range used for the spectra acquisition was from 0º-73º degrees

The setup consists of a goniometer, which is specially designed for mounting the photoluminescence collection optical components for spectral acquisition within the anglular range of 0º-73º degrees, as illustrated in Figure 6.14. A 400nm UV graded optical fiber is also used to couple the PL into a nitrogen cooled CCD spectrometer.

In Figure 6.15 one can see spectra acquired within this range of angle of PL emission. There are several modes propagating with the angle, indicating dispersive features. However, it is difficult to identify the cavity mode, the Bragg modes, the exciton, and which modes interact with each other, showing strong coupling and the equivalent Rabi splitting.

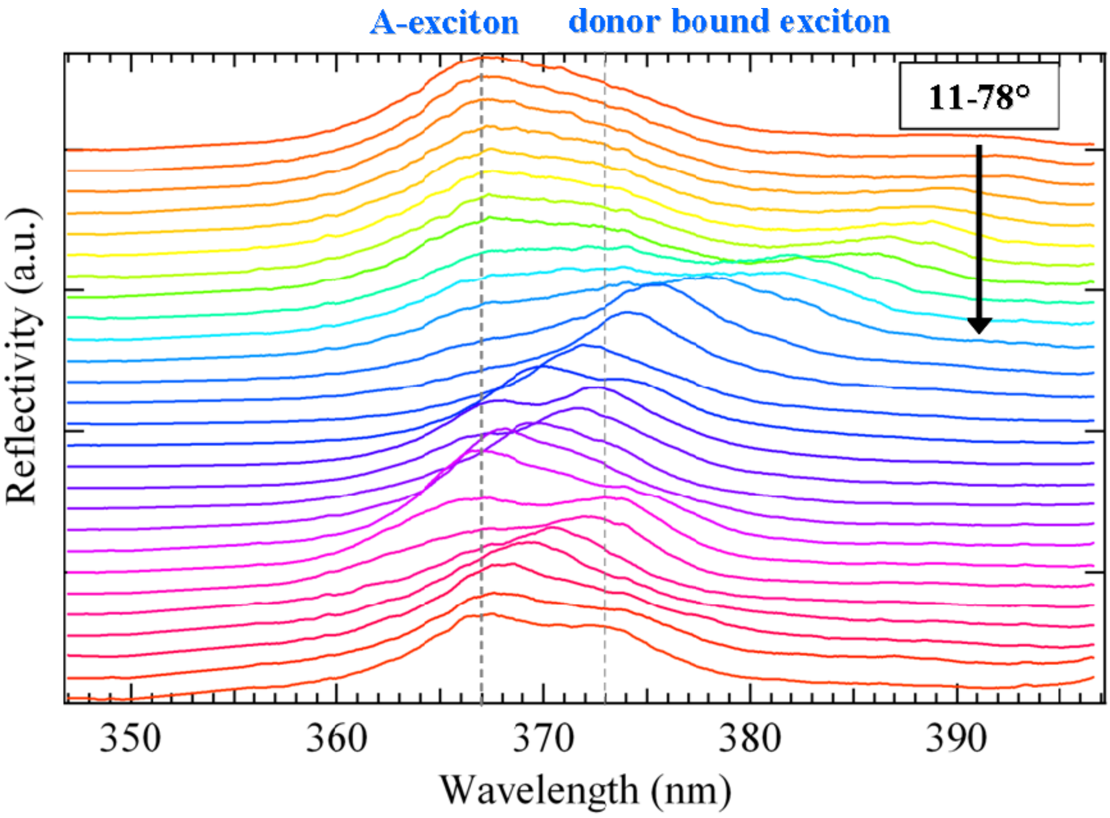

FIG. 6.15. Intentionally spaced angle resolved photoluminescence spectra of all-dielectric GaN microcavities, acquired at room temperature.

It is hard to distinguish the figure above what the different modes are. That's why we created the following contour plot out of these reflectivity spectra. In Figure 6.16 an image plot of the normalized photoluminescence intensity is presented. At small angles clear excitonic emission coinciding with PL emission from a bare GaN membrane (solid black line) is observed. For larger angles, enhanced PL emission arises from filtering of excitonic PL through photonic Bragg modes on the low energy side of the mirror stopband. Notably, the low energy Bragg modes extracted from reflectivity measurements on reference samples, for both top and bottom DBR mirror, split into distinct TE, TM modes above 15° as shown in Figure 5 (dashed line). Good agreement between PL emission and extracted Bragg mode dispersions up to 60° is also observed.

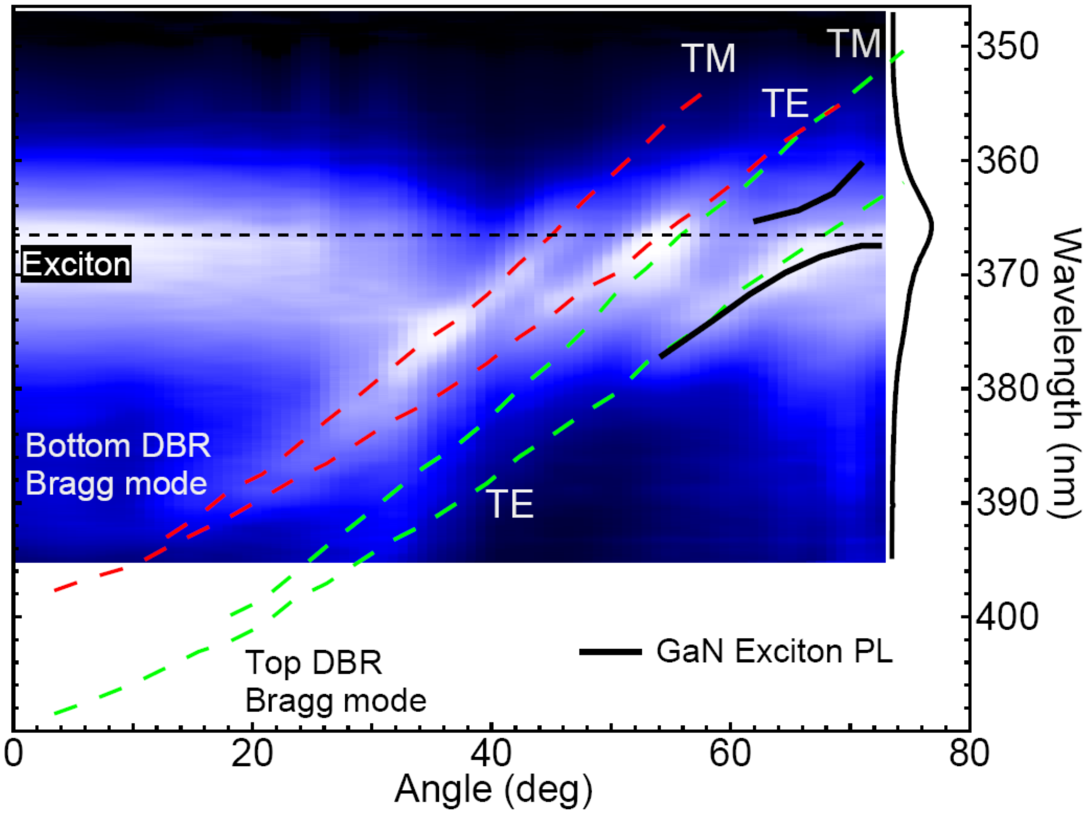

FIG. 6.16. Plot of intensity normalized photoluminescence from GaN microcavity sample. Dashed lines are TM, TE Bragg modes extracted from reference mirror samples for the top and bottom DBRs respectively. Strong exciton-Bragg mode coupling and anticrossing behaviour are observed around 68°. Solid lines are just guides for the eye.

We observe clear signature of the strong coupling regime near 68°, where anticrossing behavior between top DBR TE Bragg mode and excitonic resonance (solid line) gives rise to new eigenstates of the system called Bragg polaritons [3]. Such exciton-Bragg mode strong coupling regime has been for the first time observed in CdTe microcavities [4] owing to large oscillator strength of this material. Until now, unavailability of high quality GaN microcavities with wide mirror stopbands has prevented such observation in GaN microcavities. Remarkably the anticrossing behavior is observed only for the TE Bragg mode of the top DBR, since it has the highest cavity finesse values at such large angles, while remaining in the vicinity of the excitonic resonance. We also note that this sample does not exhibit the conventional exciton-cavity mode strong coupling regime since for the chosen thickness of our membrane the sample is positively detuned at normal incidence. For the observation of cavity mode-exciton strong coupling a thicker GaN membrane has to be incorporated in the microcavity.

6.4 Conclusions

We show that by careful optimization of the photo-electrochemical etching conditions it is possible to induce high selectivity lateral etching of buried InGaN layers in a GaN matrix. Using this bandgap selective lateral etching technique, ultrathin optical quality freestanding GaN membranes are fabricated and sandwiched between dielectric mirrors to form microcavity. In these high quality microcavites strong exciton-Bragg mode coupling is observed opening new opportunities for observation of polariton nonlinearities such as lasing, parametric amplification and oscillation at room temperature.

References

[1] H. S. Yang, S. Y. Han, K. H. Baik, S. J. Pearton, and F. Ren, “Effect of inductively coupled plasma damage on performance of GaN–InGaN multiquantum-well light-emitting diodes,” *Applied Physics Letters*, vol. 86, no. 10, p. 102104, 2005.

[2] P. Yeh, *Optical Waves in Layered Media*, 2nd ed. Wiley-Interscience, 2005.

[3] A. Askitopoulos, L. Mouchliadis, I. Iorsh, M. A. Kaliteevski, Z. Hatzopoulos, and P. G. Savvidis, “Strong Exciton-Bragg Photon Coupling in an Unfolded Microcavity: Bragg Polaritons,” *1010.4114*, Oct. 2010.

[4] M. Richard, R. Romestain, R. André, and L. S. Dang, “Consequences of strong coupling between excitons and microcavity leaky modes,” *Applied Physics Letters*, vol. 86, no. 7, p. 071916, 2005.

Chapter 7: Strong Coupling in Organic Microcavities

7.1 Advantages of Organic Microcavities

Strongly coupled organic microcavities can readily be made to span the entire visible spectrum at room temperature due to the high binding energy (~1 eV) of Frenkel excitons [1]. The strong coupling regime in an organic-based microcavity was demonstrated in 1998 by David Lidzey and co-workers [2] using a porphyrin molecule (4TBPPZn) blended in a polystyrene film as an optically resonant material at room temperature. Following this pioneering work, a variety of organic materials were used to realize strongly coupled microcavities. Because such organic systems are so different from their inorganic counterparts, so are organic cavity polaritons different from inorganic cavity polaritons [3].

Organic semiconductors, like j-aggregates, have inhomogeneous linewidths between 50 and 90 meV. These relatively broad inhomogeneous linewidths, compared to inorganic semiconductor materials, have not, however, prevented organic semiconductors from reaching the strong-coupling regime. This is because the Rabi-splitting energy is proportional to the square root of the exciton oscillator strength. As the oscillator strength of organic thin films can be at least two orders of magnitude greater than that of a single III-V QW, large Rabi splittings of up to 160 meV may be achieved [2], [4].

In this Chapter we present our work on strongly coupled j-aggregates-based microcavities. Very little work has been done already in investigating non-linear properties of such structures. Thus, our goal is to fabricate j-aggregate based microcavities in order to study their exciton-polariton dynamics and show stimulated scattering, as in inorganic semiconducting system. We fabricate microcavities with metallic mirrors and we show strong coupling of about 56meV. These metallic microcavities are our primary material for the study of the non-linear properties, using pump-probe techniques.

7.2 J-aggregates

J-aggregates of cyanine dyes are organic polar molecules of the π-conjugated family, discovered in the mid-1930s by Jelley [5]. They have attracted the interest of researchers due to their outstanding optical properties, which used them as spectral sensitizers for silver halides in conventional photography [6]. They constitute of close packing of polar monomer cyanine dye molecules coupled by Wan der Waals forces between the monomers which facilitate aggregation. This aggregation is responsible for the formation of an electronic structure similar to that meet in inorganic semiconductors, showing exctonic states.

Their large Frenkel exciton binding energy (see also Fig. 1.4) and oscillator strength [7] are the characteristic features of these materials [8-11] which give very strong exciton-photon coupling and high polariton stability at room temperature, as such as small polariton density of states and high phonon scattering rates relative to inorganics.

7.3 Band structure of π-conjugated polymers

Electronic conduction in big organic molecules takes place by the facile migration of electrons through the molecular and solid structure. This process occurs because large molecules that have delocalized, unsaturated electronic structure (many double or triple bonds in communication with each other) generate properties that are not found in simple molecules.

To understand band structure of an aggregate one has to consider a simple diatomic molecule derived from two identical atoms that have only one electron available for bonding [12]. The energy level of these two electrons involves the generation of two new energy levels-the bonding level, occupied by the two electrons, and an unoccupied antibonding level. This higher level can be populated temporarily if bonding level electrons acquire sufficient energy from heat or light to make the transition.

Bond formation in more complex molecules follows the same principle. As each bond is formed an additional bonding and antibonding level is added to the overall electronic structure. Thus, the larger the number of atoms that are linked together in a molecule or ultrastructure, the greater will be the number of bonding and antibonding orbitals. In a high carbon atom number molecule as in aggregated systems or solid state systems, hundreds, thousands or millions of atoms may be involved and the number of molecular orbitals becomes correspondingly large.

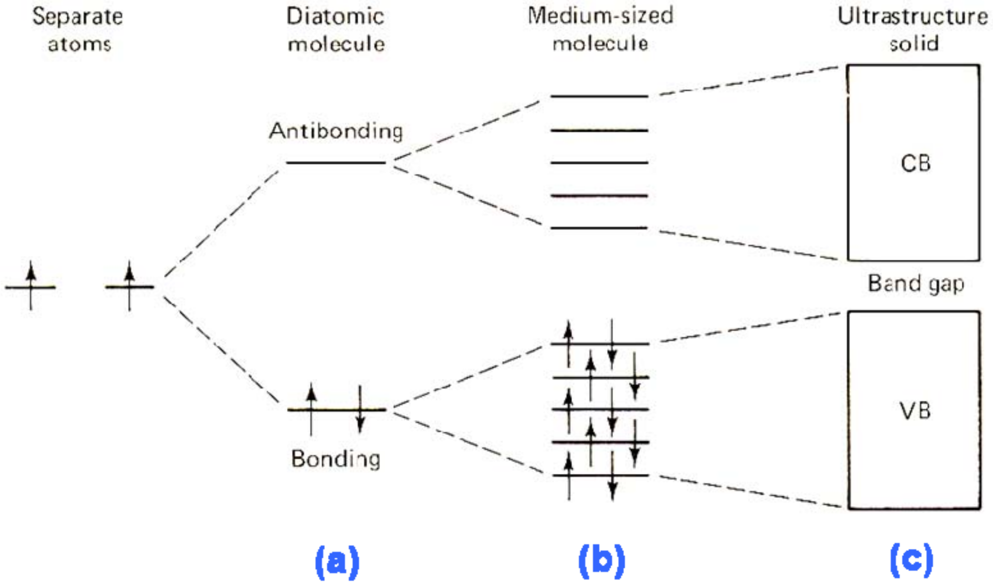

FIG. 7.1 Progression from atomic orbitals in two isolated atoms, through the formation of a bonding orbital in a simple diatomic molecule, and the generation of several bonding orbitals in a medium sized molecule, to the coalescence of orbital energy levels into bands. This last situation occurs when thousands or millions of atoms are connected to each other by a three-dimensional network of bonds. As in the case of small molecules, the energy levels are separated into a bonding set (valence band) and an antibonding set (conduction band) [12].

Beyond a certain size of “molecule” the bonding orbitals become crowded together on the energy scale to form a set of closely spaced energy levels. This set is known as a bonding *band* or, in physics or solid state terminology, as the *valence band*. The term “band” is used because the energy levels are so closely spaced that for all practical purposes they form an energy continuum within which electrons can exchange places and are free to wander throughout the material. A similar crowding and band formation occurs with the antibonding orbitals, which are described as the *conduction* *band*. The two bands are usually separated by an energy gap and the degree to which the valence band is filled with electrons determine if the material is an insulator, a semiconductor, or a “semimetal”. These possibilities are shown schematically in figure 1.

7.4 Excitonic Transitions in J-aggregates

Aggregates exhibit two characteristic sharp absorption peaks, the so-called J- and H-bands. The J-band absorption is red shifted and the H-band is blue shifted in respect to monomers absorption. These bands are attributed to the relative position (parallel or lined-up) between monomers.

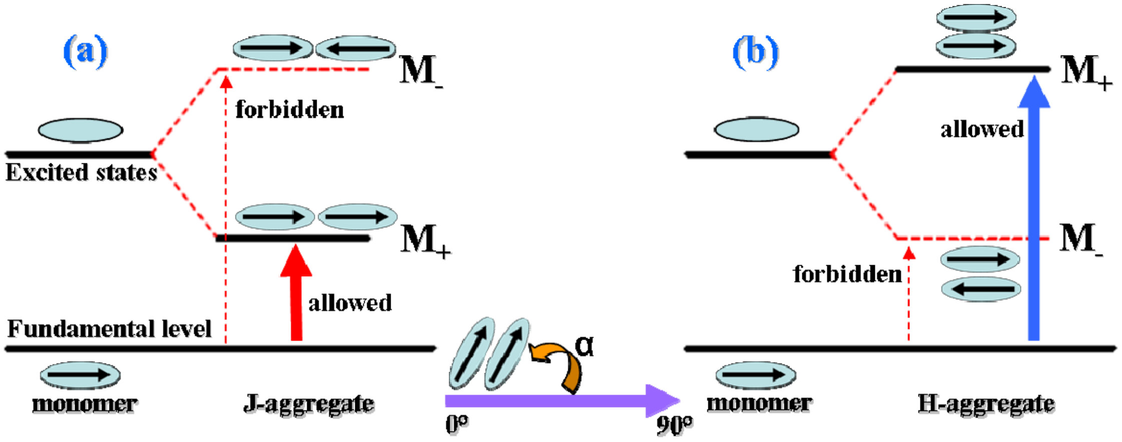

FIG. 7.2. Schematic representation of the electronic transitions in a monomer, H aggregate, and J-aggregate on the basis of the interaction between molecular excitons in aggregates, where *a* is the slip angle between molecules in an aggregate, and E_{TR}(M), E_{TR}(H), and E_{TR}(J) are the transition energies of a monomer, H-aggregate, and J-aggregate, respectively [13].

The angle between the long axis of a dye molecule and that of an aggregate *(a)* is most important, and that J-aggregates have a small *a,* while H-aggregates have a large *a.* On the basis of the molecular exciton theory [14], a description is given of the transition energy of an aggregate composed of monomer molecules 1 and 2 (E_{TR}^{A}) with respect to that of a monomer (E_{TR}^{M}) [15-17]. According to this, the transition probability of the aggregate is determined by the transition moment ($M_{\pm}$). Figure 7.2 illustrates these electronic transitions of a monomer and an aggregate as a function of *a*.

The transitions to the excited states of aggregates with transition dipoles in parallel and opposite directions give M and 0 as M_{+} and M_{-} respectively, and are therefore allowed and forbidden, respectively. For the aggregate with large *a* (i.e., H-aggregate) the energy of the allowed transition is larger (blue shift) than the energy of the monomer in the excited state, and smaller (red shift) than the energy of the monomer in the ground state for the aggregate with small *a* (i.e., J-aggregate).

Thus, electronic coupling between the transition moments of the cyanine dye causes splitting of the excited state into an exciton band. This explains an optical transition which is red shifted in relation to the monomer's spectrum [13].

7.5 Material Selection and Microcavity Fabrication Process

The monomer of cyanine dye we have chosen to fabricate our microcavities has the structure depicted in Figure 7.3a and its molecular weight is $M_w = 573.61$. The electric dipole depicted in this figure is the reason of the aggregation among the monomers. The reason we selected this particular cyanine dye is its sharp emission and absorption peaks of ~52meV. This specific cyanine dye has a monomer absorbing at 578nm with a linewidth of 0.254eV and the j-aggregate red shifts the peak absorption at 654nm with a linewidth of 0.0613eV as shown in Figure 7.3b.

We used this particular cyanine dye for the fabrication of organic microcavities. Fused silica glass was used as non-absorbing in the UV range substrate. The first mirror of the cavity consisted of a 350nm Aluminum thin film, fabricated using e-beam evaporation. A reflectivity spectrum of such a mirror is shown in Figure 7.4. The organic j-aggregate layer is spin coated above the metallic mirror and the cavity is completed by a second evaporation of 350nm of Aluminum. The j-aggregate is formed during the spin coating process.

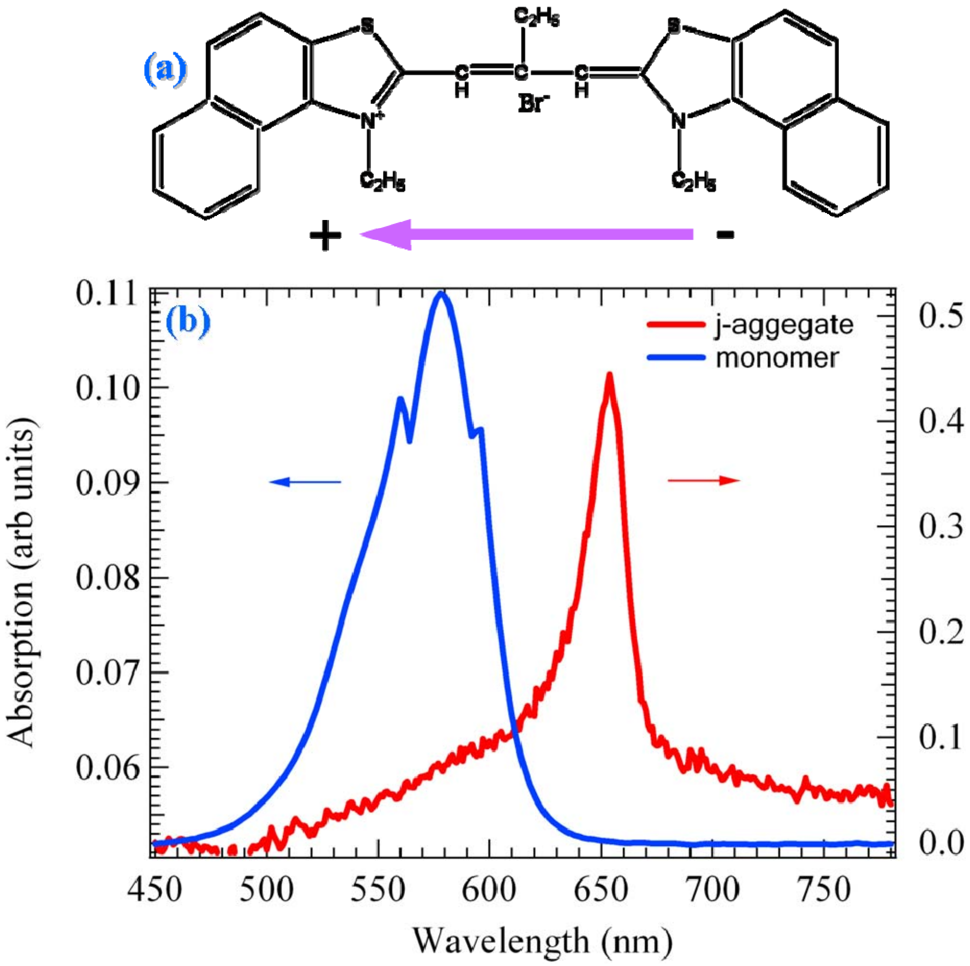

FIG. 7.3. a) Schematic representation of monomer's structure and its polarization direction, b) Peak absorption of our cyanine dye monomer molecule and its corresponding j-aggregate.

Aluminum mirrors are not as reflective as dielectric mirrors. They have lower, compared to the DBR, reflectivity of 0.9, in the desired range of the wavelengths of the j-aggregate emission However, they are quiet sufficient for showing strong coupling when combined with the large binding energy and oscillator strength of Frenkel exciton of j-aggregates. Thus, Aluminum evaporation is a cheap and easy process for j-aggregate microcavity mirror fabrication.

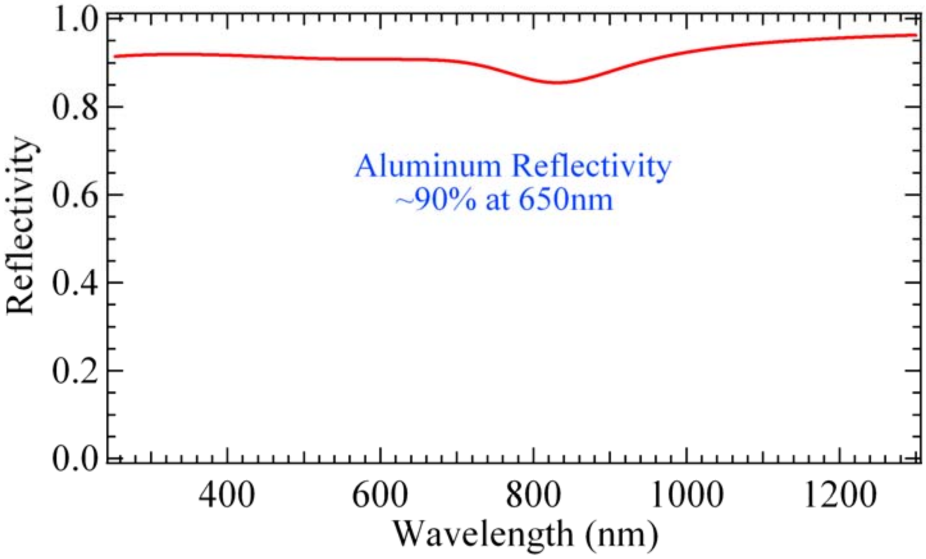

FIG. 7.4. Simulation of aluminum reflectivity spectra with a thickness of 350nm. There is a deep at 832nm, close to the region of interest for the strong coupling between the cavity mode made of aluminum mirrors and the j-aggregate exciton absorption around 655nm.

In order to acquire the desired optical thickness of the j-aggregate, we prepare a series of samples with different spin coating conditions.

ACTIVE MATERIAL	**CONCENTRATION OF ACTIVE MATERIAL**	**SOLVENT**	**RPM**	**SEC**	**RPM/SEC**	**Annealing (T, t)**	**SUBSTRATE**
Cyanine dye NK-716/gelatin	3	H_2O	3000	60	3000	Overnight	Quartz Al 350 Å

TABLE 7.1. List of optimized conditions for the fabrication of a strongly coupled j-aggregate microcavity.

Angular velocity, acceleration and spinning time at several concentrations of aggregates help as to optimize the film's surface roughness, its thickness and reduce the big fluctuations of the thickness across the substrate's surface. The following table below shows the conditions of the optimized cyanine dye microcavity.

7.6 Optical Characterization

The white light transmission spectroscopy experiments are performed using the setup depicted in Figure 7.5. An Ocean Optics 500Watt Xe-Ar compact lamp is used as a white light source. A beam is focused on a ~80μm spot size, on the microcavity.

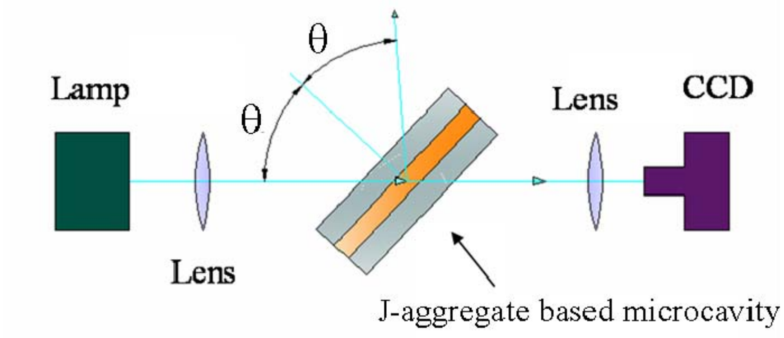

FIG. 7.5. Experimental setup of white light transmittance.

Just behind the sample, a lens, coupled to a multimode 400nm thick quartz optical fiber, was collecting the transmitted beam, leading it on an Ocean Optics computer controlled compact spectrometer. The sample was mounted on a rotational stage, thus, it allowing easy transmission spectra acquisition at several angles of incidence. These spectra are shown in Figure 7.6a. The peak position at every angle of incidence shows also strong coupling in the dispersion curve of the polaritons (figure 6b). A 56meV Rabi splitting was measured at 30°.

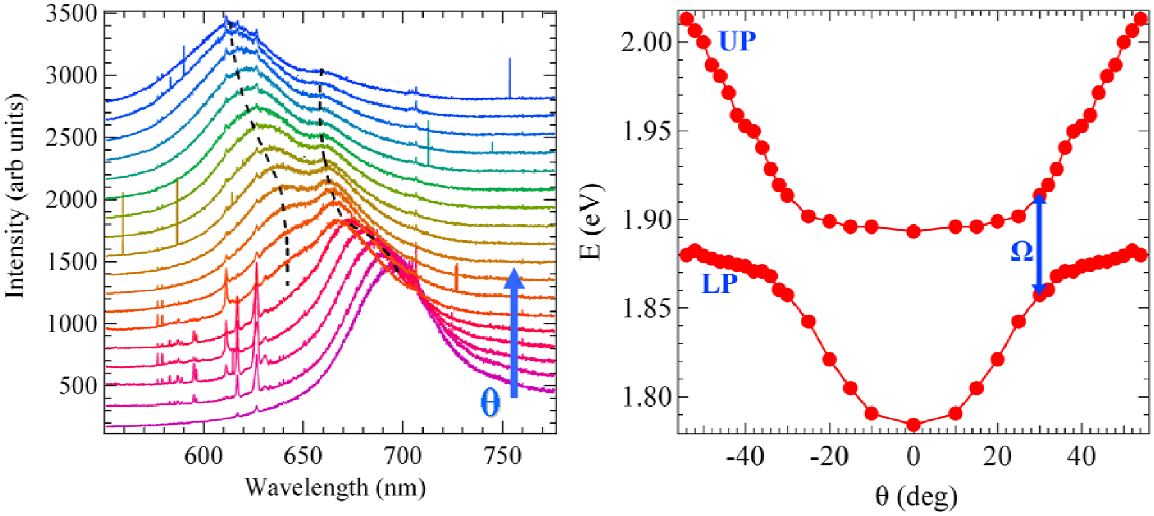

FIG. 7.6. a) Transmittance spectra from j-aggregate microcavity. They are intentionally spaced in order to show the anticrossing of lower and upper polariton branch, b) polariton dispersion curve versus the angle of incidence.

Despite the small reflectivity of the aluminium mirrors the Frenkel exciton of this particular j-aggregate is strongly coupled with the cavity mode.

7.7 Future Work-Perspectives

In conclusion, we have fabricated j-aggregate based organic microcavities, which show strong coupling with a Rabi splitting of 56meV. This is achieved with use of metallic mirrors. Future work must be done with stronger photon confinement by using dielectric mirrors. Our perspectives are the study of non-linear properties of organic based high-Q microcavities such as the polariton amplification and stimulating scattering and the investigation of possibility showing electrically pumped polariton lasing at room temperature. J-aggregates are very promising materials for such applications due to the their large variety and plethora of emission photon energies. This advantage will lead to tunable polariton emitters of the future.

References

[1] Kena-CohenS. and ForrestS. R., “Room-temperature polariton lasing in an organic single-crystal microcavity,” *Nat Photon*, vol. 4, no. 6, pp. 371-375, Jun. 2010.

[2] D. G. Lidzey, D. D. C. Bradley, M. S. Skolnick, T. Virgili, S. Walker, and D. M. Whittaker, “Strong exciton-photon coupling in an organic semiconductor microcavity,” *Nature*, vol. 395, no. 6697, pp. 53-55, 1998.

[3] G. C. La Rocca, “Organic photonics: Polariton lasing,” *Nat Photon*, vol. 4, no. 6, pp. 343-345, Jun. 2010.

[4] D. G. Lidzey, A. M. Fox, M. D. Rahn, M. S. Skolnick, V. M. Agranovich, and S. Walker, “Experimental study of light emission from strongly coupled organic semiconductor microcavities following nonresonant laser excitation,” *Physical Review B*, vol. 65, no. 19, p. 195312, May. 2002.

[5] E. E. Jelley, “Spectral Absorption and Fluorescence of Dyes in the Molecular State,” *Nature*, vol. 138, no. 3502, pp. 1009-1010, 1936.

[6] W. L. Jolly, “Photographic Sensitivity: Theory and Mechanisms By Tadaaki Tani (Fuji Photo Film Co.). Oxford University Press: New York and Oxford. 1995. viii + 254 pp. $75.00. ISBN 0-19-507240-5.,” *Journal of the American Chemical Society*, vol. 118, no. 39, p. 9460, Jan. 1996.

[7] “New optical properties by extraordinary high oscillator strength in ordered dye films.” [Online]. Available: http://cat.inist.fr/?aModele=afficheN&cpsidt=14129056. [Accessed: 29-Oct-2010].

[8] R. H. Friend et al., “Electroluminescence in conjugated polymers,” *Nature*, vol. 397, no. 6715, pp. 121-128, Jan. 1999.

[9] D. G. Lidzey, D. D. C. Bradley, T. Virgili, A. Armitage, M. S. Skolnick, and S. Walker, “Room Temperature Polariton Emission from Strongly Coupled Organic Semiconductor Microcavities,” *Physical Review Letters*, vol. 82, no. 16, p. 3316, Apr. 1999.

[10] A. I. Tartakovskii et al., “Raman scattering in strongly coupled organic semiconductor microcavities,” *Physical Review B*, vol. 63, no. 12, p. 121302, Mar. 2001.

[11] D. G. Lidzey, D. D. C. Bradley, A. Armitage, S. Walker, and M. S. Skolnick, “Photon-Mediated Hybridization of Frenkel Excitons in Organic Semiconductor Microcavities,” *Science*, vol. 288, no. 5471, pp. 1620-1623, Jun. 2000.

[12] H. Allcock, F. Lampe, and J. Mark, *Contemporary Polymer Chemistry*, 3rd ed. Prentice Hall, 2003.

[13] A. Moliton and R. C. Hiorns, “Review of electronic and optical properties of semiconductingπ-conjugated polymers: applications in optoelectronics,” *Polymer International*, vol. 53, no. 10, pp. 1397-1412, 2004.

[14] A. S. Davydov, “THE THEORY OF MOLECULAR EXCITONS,” *Soviet Physics Uspekhi*, vol. 7, no. 2, pp. 145-178, 1964.

[15] T. Kobayashi, *J-aggregates*. World Scientific, 1996.

[16] N. Kato et al., “Determination of a Merocyanine J-Aggregate Structure and the Significant Contribution of the Electric Dipole Interaction to the Exciton Band Wavelength,” *Physical Review Letters*, vol. 94, no. 13, p. 136404, Apr. 2005.

[17] A. Datta and S. K. Pati, “Dipole orientation effects on nonlinear optical properties

of organic molecular aggregates," *The Journal of Chemical Physics*, vol. 118, no. 18, p. 8420, 2003.

Annex Transfer Matrix Formulation for Isotropic Layered Media

AX.1 Reflection and Transmission of s Waves (TE Wave)

The s wave also known as TE wave because the electric field vector **E** is transverse to the plane of incidence. Referring to figure B, we consider the reflection and transmission of the s wave. All dielectric field vectors are perpendicular to the plane of incidence , and the magnetic field vectors are chosen to give a positive energy flow in the direction of wave vectors.

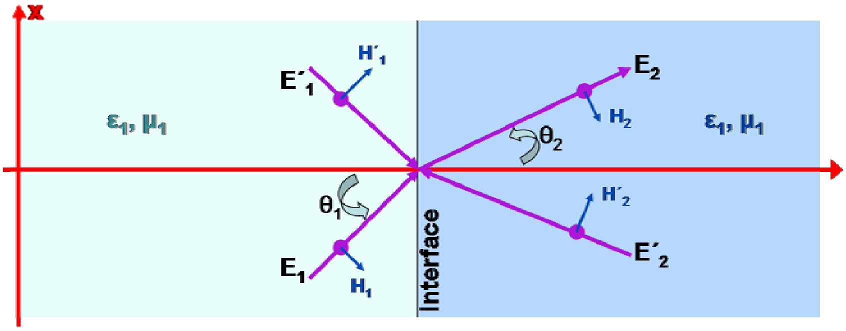

FIG. A.1. Schematic drawing of the standing-wave patterns in a $\lambda/2$ cavity

Imposing the continuity of E_y and H_z at the interface x=0 leads to

$$E_{1S}+E'_{1S}=E_{2S}+E'_{2S}$$
$$\sqrt{\frac{\varepsilon_1}{\mu_1}}(\mathrm{E}_{1s}-E'_{1s})\cos\theta_1=\sqrt{\frac{\varepsilon_2}{\mu_2}}(\mathrm{E}_{21s}-E'_{2s})\cos\theta_2, \qquad \text{(A.1 \& A.2)}$$

where θ_1 and θ_2 are the angles of the wave vectors $\mathbf{k}_1$ and $\mathbf{k}_2$, respectively, with respect to the normal to the interface. These two equations can be rewritten as a matrix equation:

$$D_s(1)\begin{pmatrix}E_{1s}\\E'_{1s}\end{pmatrix}=D_s(2)\begin{pmatrix}E_{2s}\\E'_{2s}\end{pmatrix} \qquad \text{(A.3)}$$

where

$$D_s(i) = \begin{pmatrix} 1 & 1 \\ \sqrt{\frac{\varepsilon_i}{\mu_i}}\cos\theta_i & -\sqrt{\frac{\varepsilon_i}{\mu_i}}\cos\theta_i \end{pmatrix}, \quad \text{i=1, 2} \qquad \text{(A.4)}$$

The $D_s(i)$ is called the *dynamical matrix* of the s wave for the medium i (i=1, 2). If the light is incident from medium 1, the reflection and transmission coefficients are given for a single interface as

$$r_s = \left(\frac{E'_{1s}}{E_{1s}}\right)_{E'_{2s}=0}, \qquad t_s = \left(\frac{E_{2s}}{E_{1s}}\right)_{E'_{2s}=0} \qquad \text{(A.5)}$$

The subscript $E'_{2s} = 0$ indicates that only the transmitted wave E_{2s} exists in the medium 2 because the incident wave is launched from medium 1.

AX.2 2x2 Matrix Formulation for a Thin Film

The problem of the reflection and transmission of electromagnetic radiation through a film can be solved by using the 2x2 matrix method. The dielectric structure is described by the following equation

$$n(x) = \begin{cases} n_1, & x < 0, \\ n_{2,} & 0 < x < d, \\ n_3, & d < x, \end{cases} \qquad \text{(A.6)}$$

where n_1, n_2, n_3 are the refractive indices and d the thickness of the film. Since the whole medium is homogeneous in the z direction (i.e., $\partial n / \partial z = 0$), the electric field that satisfies the Maxwell's equations has the form

$$E = E(x)e^{i(\omega t - \beta z)}, \qquad \text{(A.7)}$$

where β is the z component of the wave vector and ω is the angular frequency. In equation (44), we assume that the electromagnetic wave is propagating in the xz plane, and we further assume that the electric field is either an s wave (with **E**||**y**).

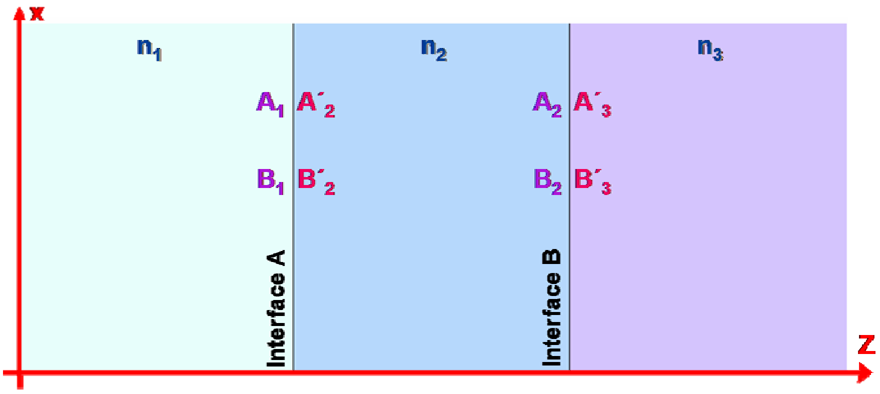

FIG. A.2. Schematic drawing of the standing-wave patterns in a $\lambda/2$ cavity

The electric field E(x) consists of a right-traveling wave and a left-traveling wave and can be written as

$$E(x) = \mathrm{R}e^{-ik_x x} + Le^{ik_x x} = A(x) + B(x)\,, \qquad \text{(A.8)}$$

where $\pm k_x$ are the x components of the wave vector and R and L are the constants in each homogeneous layer. Let A(x) represent the amplitude of the right-traveling wave and B(x) be that of the left-traveling wave one. To illustrate the matrix method, we define

$$\begin{aligned} A_1 &= A(0^-),\ B_1 = B(0^-), \\ A_2' &= A(0^+),\ B_2' = B(0^+), \\ A_2 &= A(d^-),\ B_2 = B(d^-), \\ A_3' &= A(d^+),\ B_3' = B(d^+) \end{aligned} \qquad \text{(A.9)}$$

where 0^- represents the left side of the interface, x=0, and 0^+ represents the right side of the interface. Similarly, d^- and d^+ are defined for the interface at x=d. Note that E(x) for the s wave is a continuous function of x. however as a result of the decomposition of the equation (45), A(x) and B(x) are no longer continuous at the interfaces. If we present the two amplitudes of E(x) as column vectors, the column vectors shown I figure D are related by

$$\begin{pmatrix} A_1 \\ B_1 \end{pmatrix} = D_1^{-1} D_2 \begin{pmatrix} A_2' \\ B_2' \end{pmatrix} = D_{12} \begin{pmatrix} A_2' \\ B_2' \end{pmatrix}$$

$$\begin{pmatrix} A_2' \\ B_2' \end{pmatrix} = P_2 \begin{pmatrix} A_2 \\ B_2 \end{pmatrix} = \begin{pmatrix} e^{i\phi_2} & 0 \\ 0 & e^{-i\phi_2} \end{pmatrix} , \qquad \text{(A.10)}$$

$$\begin{pmatrix} A_2 \\ B_2 \end{pmatrix} = D_2^{-1} D_3 \begin{pmatrix} A_3' \\ B_3' \end{pmatrix} = D_{23} \begin{pmatrix} A_3' \\ B_3' \end{pmatrix}$$

where D_1, D_2 and D_3 are the dynamical matrices of the waves in the mediums 1, 2, and 3 respectively and given by

$$D_a = \begin{pmatrix} 1 & 1 \\ n_a \cos\theta_\alpha & -n_a \cos\theta_\alpha \end{pmatrix} , \qquad \text{(A.11)}$$

where α=1,2,3 and θ_α is the ray angle in each layer and is related to β and $k_{\alpha x}$ by

$$\beta = n_a \frac{\omega}{c} \sin\theta_\alpha , \qquad k_{ax} = n_a \frac{\omega}{c} \cos\theta_\alpha , \qquad \text{(A.12)}$$

P_2 is the co-called propagation matrix, which accounts for propagation through the bulk of the layer, and the φ_2 is given by $\phi_2 = k_{2x} d$, (50)

From the equations (47), the amplitudes A_1, B_1 and A_3', B_3' are related by

$$\begin{pmatrix} A_1 \\ B_1 \end{pmatrix} = D_1^{-1} D_2 P_2 D_2^{-1} D_3 \begin{pmatrix} A_3' \\ B_3' \end{pmatrix}, \qquad \text{(A.13)}$$

Note that the column vectors representing the plane-wave amplitudes in each layer are related by a product of 2x2 matrices in sequence. Each side of an interface is represented by a dynamical matrix, and the bulk of each layer is represented by a propagation matrix. Such a recipe can be extended to the case of multilayer structures like the DBRs.

AX.3 2x2 Matrix Formulation for a Multilayer System

Referring to figure E, we consider the case of multilayer structures. The dielectric structure is described by

$$n(x) = \begin{cases} n_0 & x < x_0 \\ n_1 & x_0 < x < x_1 \\ n_2 & x_1 < x < x_2 \\ \cdots & \cdots \\ n_N & x_{N-1} < x < x_N \\ n_s & x_N < x \end{cases}, \qquad (A.15)$$

where n_i is the refractive index of the l^{th} layer, x_1 is the position of the interface between the l^{th} layer and the $(l+1)^{th}$ layer, n_s is the substrate index of refraction, and n_0 is that of the incident medium.

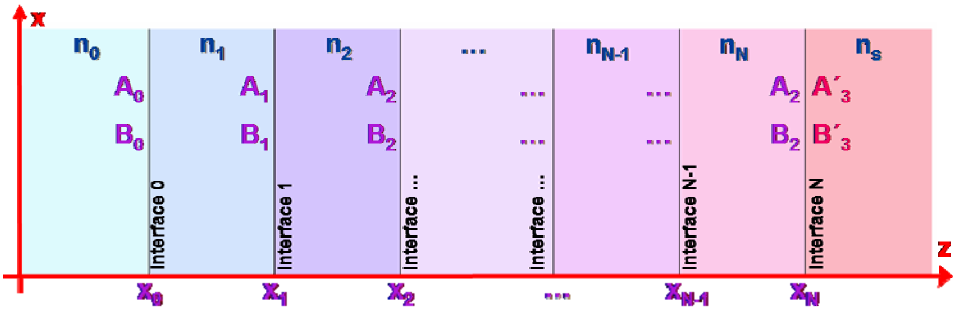

FIG. A.3. Schematic drawing of the standing-wave patterns in a $\lambda/2$ cavity

The layer thickness d_1 are related to the x_1's by

$$\begin{aligned} d_1 &= x_1 - x_0 \\ d_2 &= x_2 - x_1 \\ \ldots.. &= \ldots - \ldots. \\ d_N &= x_N - x_{N-1} \end{aligned}, \qquad (A.16)$$

The electric field of a general plane-wave solution of the wave equation can still be written as $E = E(x)e^{i(\omega t - \beta z)}$, (57) where the electric field distribution $E(x)$ can be written as

$$E(x) = \begin{cases} A_0 e^{-ik_{0x}(x-x_0)} + B_0 e^{ik_{0x}(x-x_0)} & x < x_0 \\ A_1 e^{-ik_{1x}(x-x_1)} + B1 e^{ik_{10x}(x-x_1)}, & x_{l-1} < x < x_l, \\ A_s^{'} e^{-ik_{sx}(x-x_N)} + B_s^{'} e^{ik_{sx}(x-x_N)} & x_N < x \end{cases} \qquad (A.17)$$

where k_{lx} is the x component of the wave vectors

$$k_{lx} = \left[\left(n_1 \frac{\omega}{c}\right)^2 - \beta^2\right]^{1/2}, \quad l = \text{o, 1, 2, …., N, s}, \qquad (A.18)$$

and is related to the ray angle θ_i by $k_{lx} = n_1 \dfrac{\omega}{c}\cos\theta_1$, (A.19)

According to equations (58) and (59), A_l and B_l represent the amplitude of plane waves at interface $x = x_l$. Thus, using the dynamical matrices we can write:

$$\begin{pmatrix} A_0 \\ B_0 \end{pmatrix} = D_0^{-1} D_1 \begin{pmatrix} A_1 \\ B_1 \end{pmatrix}, \quad \text{(A.20)}$$

$$\begin{pmatrix} A_l \\ B_l \end{pmatrix} = P_1 D_1^{-1} D_{l+1} \begin{pmatrix} A_{l+1} \\ B_{l+1} \end{pmatrix}, \quad l = 1, 2, \ldots, \mathrm{N}, \quad \text{(A.21)}$$

where $N+1$ represents s, $A_{N+1} = A_s^{'}$, $B_{N+1} = B_s^{'}$ and the matrices can be written as

$$D_l = \begin{pmatrix} 1 & 1 \\ n_1 \cos\theta_l & -n_1 \cos\theta_l \end{pmatrix}, \quad \text{(A.22)}$$

and $$P_1 = \begin{pmatrix} e^{i\phi_l} & 0 \\ 0 & e^{-i\phi_l} \end{pmatrix} \quad \text{with} \quad \phi_l = k_{lx} d_1, \quad \text{(A.23)}$$

The relation between A_0, B_0 and $A_s^{'}$, $B_s^{'}$ can thus be written as

$$\begin{pmatrix} A_0 \\ B_0 \end{pmatrix} = \begin{pmatrix} M_{11} & M_{12} \\ M_{21} & M_{22} \end{pmatrix} \cdot \begin{pmatrix} A_s^{'} \\ B_s^{'} \end{pmatrix}, \quad \text{(A.24)}$$

with the matrix given by

$$\begin{pmatrix} M_{11} & M_{12} \\ M_{21} & M_{22} \end{pmatrix} = D_0^{-1} \left[\prod_{l=1}^{N} D_1 P_1 D_1^{-1} \right] \cdot D_s, \quad \text{(A.25)}$$

Here, we recall that N is the number of layers, A_0 and B_0 are the amplitudes of the planes in medium 0 at $x = x_0$, and $A_s^{'}$, $B_s^{'}$ are the amplitudes of the plane waves in medium s at $x = x_N$. For multilayer structures, the expressions for M_{ij} become complicated and are best handled by a computer program.

AX.4 Transmittance and Reflectance

Using the 2x2 matrix method, we now discuss the reflectance and transmittance of monochromatic plane waves through a multilayer dielectric structure. If the light is incident from medium 0, the reflection and transmission coefficients are defined as

$$r = \left(\frac{B_0}{A_0} \right)_{B_s=0} \quad \text{and} \quad t = \left(\frac{A_s}{A_0} \right)_{B_s=0} , \quad \text{(A.26)}$$

respectively. Here we drop the $(')$ prime and define $A_s = A_s^{'}$, $B_s = B_s^{'}$.

Using the matrix equation (66) and following definitions (68) and (69), we obtain

$$r = \frac{M_{12}}{M_{11}} \quad \text{and} \quad t = \frac{1}{M_{11}} , \quad \text{(A.27)}$$

Reflectance is given by

$$R = |r|^2 = \left| \frac{M_{21}}{M_{11}} \right|^2 , \quad \text{(A.28)}$$

provided medium 0 is lossless.

If the bounding media (0,s) era both pure dielectric with real n_s and n_0 , transmittance T is given by

$$T = \frac{n_s \cos\theta_s}{n_0 \cos\theta_0} |t|^2 = \frac{n_s \cos\theta_s}{n_0 \cos\theta_0} \left| \frac{1}{M_{11}} \right|^2 , \quad \text{(A.29)}$$

provided both the incident wave and the transmitted wave have real propagation vectors.

AX.5 Quarter-Wave Stack

To illustrate the use of the matrix method in the calculation of the reflection and transmission of a multilayer structure, we consider a layered medium consisting of N pairs of alternating quarter waves ($n_1 d_1 = n_2 d_2 = \lambda / 4$) with refractive indices n_1 and n_2, respectively. Let n_0 by the index of refraction of the incident medium and n_s be the index of refraction of the substrate. The reflectance R at normal incidence can be obtained as follows: According to equation (67), the matrix is given by

$$\begin{pmatrix} M_{11} & M_{12} \\ M_{21} & M_{22} \end{pmatrix} = D_0^{-1}\left[D_1 P_1 D_1^{-1} D_2 P_2 D_2^{-1}\right]^N D_s , \qquad (A.30)$$

The propagation matrix for quarter-wave layers (with $\phi_l = \frac{1}{2}\pi$) is given by

$$P_{12} = \begin{pmatrix} i & 0 \\ 0 & -i \end{pmatrix}, \qquad (A.31)$$

By using the equation (63) for the dynamical matrices and assuming normal incidence, we obtain, after some matrix manipulation,

$$D_1 P_1 D_1^{-1} D_2 P_2 D_2^{-1} = \begin{pmatrix} \frac{-n_1}{n_2} & 0 \\ 0 & \frac{-n_1}{n_2} \end{pmatrix}, \qquad (A.32)$$

Carrying out the matrix multiplication in equation (73) and using the equation (71) the reflectance is

$$R = \left(\frac{1-(n_s/n_0)(n_1/n_2)^{2N}}{1+(n_s/n_0)(n_1/n_2)^{2N}} \right)^2 , \qquad (A.33)$$

The equation can be written as

$$R = \tanh^2 Nx \qquad \text{with} \qquad x = \ln\frac{n_1}{n_2} + \frac{1}{2N}\ln\frac{n_s}{n_0} , \qquad (A.34)$$

for large N, the reflectance R approaches unity exponentially as a function of N.

The dielectric layered structure that consists of alternating quarter-wave layers of two different materials is the simplest way of achieving high reflectance. This is the so-called Bragg reflector and is a special type of periodic layered media. The reflection coefficient of such a reflector is given by Eq. (?), assuming that the substrate is the same material as one of the layers. The peak reflectance of such a structure corresponds to the wavelength when all the layers are quarter-wave in thickness. Let d_1, d_2 and n_1, n_2 be the thickness and indices of refraction of the layers respectively. Then this wavelength corresponds to

$$n_1 d_1 = \frac{1}{4}\lambda, \qquad n_2 d_2 = \frac{1}{4}\lambda \quad \text{(A.35)}$$

the peak reflectance is given by

$$R = \left(\frac{1 - \left(\frac{n_s}{n_a}\right)\left(\frac{n_2}{n_1}\right)^{2N}}{1 + \left(\frac{n_s}{n_a}\right)\left(\frac{n_2}{n_1}\right)^{2N}} \right)^2, \quad \text{(A.36)}$$

where n_s represents the index of refraction of the substrate, n_a is that of the air, and N is the number of periods. For large N, this equation can be written as

$$R = \tanh^2 (N \ln \frac{n_2}{n_1} + \frac{1}{2} \ln \frac{n_s}{n_a}), \quad \text{(A.37)}$$

Note that peak reflectance approaches unity as N increases. The bandwidth of the Bragg reflectors is determined by the forbidden band of the periodic layered structure and is given by

$$\frac{\delta\lambda}{\lambda} = \frac{4}{\pi} \sin^{-1} \frac{|n_2 - n_1|}{n_2 + n_1}, \quad \text{(A.38)}$$

This width is reduced by a factor of $(2p+1)$ if the layer thicknesses are $n_1 d_1 = (2p+1)\lambda / 4$. The equation above can be written approximately as

$$\frac{\delta\lambda}{\lambda} \approx \frac{2}{\pi} \frac{\Delta n}{n}, \quad \text{(A.39)}$$

provided that $n_1 \approx n_2$. Here $\Delta n = |n_1 - n_2|$. Note that the bandwidth of the Bragg reflector is determined by the fractional difference of the index of refraction of the neighboring layers or, equivalently, the fractional index modulation $\Delta n / n$ of the periodic layered medium [1].

References

[1] P. Yeh, *Optical Waves in Layered Media*, 2nd ed. Wiley-Interscience, 2005.